AN ELECTRON BEAM SUSTAINED EXCIMER LASER

by

Martin Casey

A thesis submitted in partial fulfilment of the requirements for the degree of Doctor of Philosophy of the University of London, and for the Diploma of Membership of the Imperial College of Science and Technology.

Blackett Laboratory
Imperial College
London
England

October 1982

Abstract

An electron beam sustained discharge excimer laser has been developed. This work describes the construction and detailed characterisation of the system, and the studies which were undertaken with it.

The electron beam generator comprised a 200 kV pulse transformer driven power supply and an electrostatically focussed electron beam diode. It is shown how the careful design and optimisation of this generator allowed very reliable, reproducible operation of the complete laser. When a discharge circuit was incorporated, and the whole system used to pump the XeCl excimer laser, average output power densities of 0.63 MW cm^{-2} were obtained at 308 nm - comparable to the highest so far reported. Results of efficiency, gain and beam quality measurements are given, and KrF laser operation is considered.

Long pulse length, high power density beams are required for a number of experiments with rare gas halide excimers. Notable among these is the generation of short pulses by mode-locking.

The illumination of a semi-insulating GaAs switch with pulses of light from a passively mode-locked dye laser can lead to the generation of very short, high voltage pulses. The use of these pulses to drive optical modulators is considered. A study of commercially available Pockels cells has led to the construction of an extremely simple optical modulator. When incorporated into an optical shutter, pulse lengths of 300 ps have been switched out at a repetition rate of >0.1 GHz. Active mode-locking results are given for both the commercial Pockels cell and the redesigned modulator. The limitations of this technique are discussed, and unsuccessful experiments to passively mode-lock the laser are described.

ACKNOWLEDGEMENTS

It is my great pleasure to be able to thank Dr. M.H.R. Hutchinson, my supervisor, and Dr. P.W. Smith for their contributions to the work reported in this thesis. Both have been a valuable source of advice and inspiration throughout the course of this project. I would especially like to thank Paul Smith, without whose original design work the laser could not have been built, nor could many of the other experiments have been completed without his continued aid.

Many other people within the Laser Group at Imperial College have also given me considerable assistance. I would specifically like to mention Dr. J.R. Taylor, for battling with the streak camera, and Roy Morrison and John Bean in the Optics Workshop for their technical support.

Dr. P.W. Smith and Dr. W. Margulis must also be thanked for their constructive criticism of the early versions of the thesis, as must Deanne Eastwood for typing it accurately.

Financial support from the Science and Engineering Research Council and Hartley Measurements Ltd., in the form of an S.E.R.C. C.A.S.E. studentship, is gratefully acknowledged.

I have spent three stimulating and enjoyable years as a postgraduate student. I would like to dedicate this thesis to those people, both inside and outside College and in my family, whose encouragement and friendship made this possible.

CONTENTS

		Page
ABSTRACT		2
ACKNOWLEDGEMENTS		3
CHAPTER 1	INTRODUCTION	12
	1.1 Introduction to excimer lasers	12
	1.2 Rare gas halide excimers	13
	1.2.1 Spectroscopy	13
	1.2.2 Kinetics	17
	1.3 Pumping of excimer lasers	22
	1.3.1 Direct e-beam pumping	22
	1.3.2 E-beam sustained discharge pumping	27
	1.3.3 Avalanche discharge pumping	29
	1.3.4 X-ray preionized discharge pumping	30
	1.3.5 Microwave pumping	31
	1.4 Objectives of this work	32
	1.4.1 Laser development	32
	1.4.2 Short pulse generation	34
CHAPTER 2	AN ELECTRON BEAM GENERATOR	36
	2.1 Introduction	36
	2.2 Description of the pulsed power supply	38
	2.2.1 The pulse transformer	38
	2.2.2 The primary circuit	42
	2.2.3 The secondary circuit	44
	2.3 Performance of the pulsed power supply	46
	2.4 The electron beam diode	50
	2.4.1 Output bushing design	50
	2.4.2 Theory of electron beam diodes	52
	2.4.3 Diode construction	54
	2.5 Diode performance	55
	2.5.1 Techniques of measurement	55
	2.5.2 Optimisation of the electron beam	57

Page

2.5.3 Experimental problems 68

2.6 Standard operating characteristics 68

CHAPTER 3 THE ELECTRON BEAM SUSTAINED DISCHARGE LASER 71

3.1 Introduction 71

3.2 The laser cavity 71

3.2.1 Design and optics 71

3.2.2 Gas handling 74

3.3 Discharge design and operation 74

3.4 Performance of the XeCl laser 79

3.4.1 Electron beam pumping 81

3.4.2 Electron beam sustained pumping 81

3.5 Laser efficiency 83

3.5.1 Electron beam energy deposition 83

3.5.2 Discharge energy deposition 86

3.5.3 Efficiency calculations 86

3.6 Measurement of the laser gain 89

3.7 Discussion of results 92

3.7.1 Optimised operation 92

3.7.2 Standard operation 93

3.8 An unstable resonator 96

3.9 An electron beam sustained KrF laser 100

3.9.1 Performance results 100

3.9.2 Explanation of the instability 103

CHAPTER 4 A FAST, HIGH REPETITION RATE OPTICAL SHUTTER 105

4.1 Introduction 105

4.2 Optical pulse generation by electrooptic phase modulation 106

4.3 The repetitive generation of short duration, high voltage electrical pulses 110

Page

4.3.1 Auston switch technology 111

4.3.2 The mode-locked dye laser 113

4.3.3 Pulse generation 117

4.4 A Pockels cell as an optical shutter 119

4.4.1 The Pockels cell 119

4.4.2 Triggering and synchronisation 121

4.4.3 The Pockels cell driving circuit 123

4.4.4 Modulation results 125

4.4.5 Circuit analysis 126

4.5 Conclusions 127

CHAPTER 5 REDESIGNING THE ELECTROOPTIC PHASE MODULATOR 129

5.1 Introduction 129

5.2 Design criteria 129

5.3 Low inductance driving of a KDP electro-optic crystal 131

5.3.1 The crystal as a section of a 50Ω transmission line 132

5.3.2 The crystal as the load of a Blumlein pulse forming line 135

5.4 Construction of an improved electro-optic modulator 140

5.4.1 The crystal and electrodes 140

5.4.2 The driving circuit 143

5.5 Performance of the modulator 143

5.5.1 Experimental results 143

5.5.2 Analysis of results 149

5.5.3 Summary and improvements 152

CHAPTER 6 MODE-LOCKING OF EXCIMER LASERS 154

6.1 Introduction 154

6.2 Active mode-locking 156

Page

6.2.1 Introduction 156
6.2.2 Active mode-locking with a commercial Pockels cell 157
6.2.3 Active mode-locking with the redesigned modulator 162
6.2.4 Discussion 167
6.3 Passive mode-locking 169
6.3.1 Introduction 169
6.3.2 Passive mode-locking of excimer lasers 170
6.3.3 Discussion 175
6.4 Conclusions 177
CHAPTER 7 CONCLUSIONS 178
7.1 Introduction 178
7.2 Review 178
7.2.1 The laser system 178
7.2.2 Pulse generation 179
7.3 Further work 179
7.3.1 The laser system 179
7.3.2 Mode-locking 181
7.3.3 Other experiments 181
REFERENCES 184
APPENDIX : PUBLICATIONS 192

LIST OF FIGURES

No.		Page
1.	General potential energy diagram for the rare gas halides	14
2.	Main kinetic routes for the formation of KrF*	18
3.	Electron beam pumping geometries	23
4.	Electrical schematic of a 5-stage Marx generator	25
5.	Simplified e-beam sustained discharge pumping geometry	28
6.	Pulsed power supply layout	37
7.	Circuit diagram of the complete system	39
8.	Simplified transformer construction diagrams	41
9.	Power supply trigger circuit diagram	43
10.	Equivalent circuit of the pulsed power supply	47
11.	Calculated and observed transformer performance	49
12.	E-beam sustained discharge head	51
13.	Synchronised electrical characteristics of the electron beam	58
14.	Transverse e-beam current density profiles	59
15.	The focussing electrodes (plate)	60
16.	Variable dimensions of the capacitive focussing system	62
17.	A prefoil (plate)	65
18.	The discharge cavity (plate)	67
19..	Diode and discharge chambers (plate)	72
20.	Laser cavity and discharge circuit	75
21.	Simplified discharge circuit diagram	77
22.	The complete laser system (plate)	78
23.	Synchronised electrical characteristics of the discharge and the laser output power	80
24.	Optmised laser output profiles	82
25.	Discharge energy deposition profiles	87

No.		Page
26.	Discharge impedance profiles	88
27.	The experimental arrangement to measure the laser gain	90
28.	Experimental set-up of the XeCl unstable resonator	97
29.	The near field spatial beam profile at L_2	98
30.	The laser output from the unstable resonator compared to the e-beam pumping pulse	99
31.	Characteristics of the KrF laser	102
32.	Symmetry axes of $\bar{4}2m$ crystals	107
33.	Simplified diagram of an electrooptic amplitude modulator	109
34.	Current delivered to a 50Ω load from a GaAs switch	112
35.	Schematic diagram of the dye laser	114
36.	Dye laser output and the resultant voltage pulse train generated from a GaAs switch	116
37.	The GaAs switch in a 50Ω line	118
38.	The Pockels cell crystal and electrodes	120
39.	The Pockels cell driving circuit	122
40.	Pockels cell driving voltage and response	124
41.	Circuit to model the performance of the Pockels cell	126
42.	Low inductance driving of KDP	133
43.	A Blumlein pulse forming line	136
44.	A KDP crystal as the load of a Blumlein line	138
45.	Voltage appearing across the load of the Blumlein line	138
46.	The redesigned crystal and electrodes	141
47.	Schematic diagram of the crystal and charging circuit	142
48.	The redesigned modulator (plate)	144

No.		Page
49.	Modulated output of the XeCl laser	146
50.	Schematic streak camera arrangement	147
51.	Circuit to model the electrical behaviour of the modulator	151
52.	Active mode-locking with a commercial Pockels cell	158
53.	Output of the actively mode-locked XeCl laser (Pockels cell)	160
54.	Mode locking with the redesigned modulator	163
55.	Output of the actively mode-locked XeCl laser (redesigned modulator)	164
56.	Passive mode-locking schemes	172

LIST OF TABLES

No.		Page
1.	Emission wavelengths and lifetimes of the B-X and C-A transitions of the rare gas halide excimers	16
2.	Dominant KrF* quenching and photoabsorption processes	21
3.	Diode optimisation results	63
4.	Pulsed power supply and diode performance summary	69
5.	Laser performance summary	95
6.	Summary of active mode-locking results	166
7.	Saturable absorbers for passive mode-locking	174

CHAPTER 1

INTRODUCTION

1.1 Introduction to excimer lasers

The term "excimer" is now used to describe both homopolar and heteropolar molecules which have bound electronic excited states and dissociative ground states. The discovery of rare gas halide excimers has led to the development of a new breed of efficient, high power, pulsed lasers operating in the ultraviolet. This work will describe the development of such a laser and the studies which were carried out with it.

There are a number of basic requirements for the efficient operation of a laser. The upper laser level must be formed efficiently and not be rapidly quenched, while the lower level population must be rapidly removed. Also, the active medium must have only a small absorption at the laser wavelength. The first parts of this chapter will show how these conditions are met by the rare gas halide excimers.

The threshold inversion density required for gain at a particular wavelength may be approximated by

$$\Delta N = \frac{\tau_r \Delta\lambda}{\tau_c \lambda^4} \qquad (1.1)$$

where λ is the transition wavelength, τ_r is the radiative lifetime and $\Delta\lambda$ the bandwidth of the transition. τ_c is the cavity damping constant[1]. Thus, ultraviolet rare gas halide lasers require much higher levels of pumping than the previously existing, longer wavelength, gas lasers and the techniques developed to achieve this will be outlined in section 1.3.

Section 1.4 will go on to introduce the electron beam sustained discharge excimer laser, whose development and operational characteristics will be discussed in Chapters 2 and 3. The second half of this thesis will then be outlined, concerning a study of the repetitive generation of short pulses of light by fast optical modulators and the use of these modulators, and other techniques, in experiments to mode-lock the excimer laser.

1.2 Rare gas halide excimers

1.2.1 Spectroscopy

A schematic potential energy diagram illustrating the electronic structure of a typical rare gas halide molecule is given in figure 1. The lowest energy curves are essentially repulsive, arising from the collision of a ground state rare gas atom R ('S) with a halide atom H ($^2P_{3/2,\ 1/2}$). The molecular states which then arise are the $X^2\Sigma$ ($\Omega = \frac{1}{2}$) and the strongly repulsive and, for most purposes, degenerate, $A^2\Pi$ (Ω = 3/2, 1/2) states[2],[3]. Usually the X, or lowest energy, state is, at most, weakly attractive and thermally unstable.

The excited states of the rare gas halides are ion pairs R^+H^- which are strongly bound relative to the lowest atomic excited states. These binding energies can be predicted to within a few per cent by noting the similarities between the excited state of a rare gas halide ion pair and the ground state ion pairs of the corresponding alkali halide molecule[4]. For example, KrF* has a very similar binding energy and formation kinetics to the RbF molecule. The H^- ion is a spherically symmetric 'S state while the R^+ ion has $^2P_{3/2,1/2}$ angular momentum. Hence, three low lying ionic excited states

General potential energy diagram
for the rare gas halides

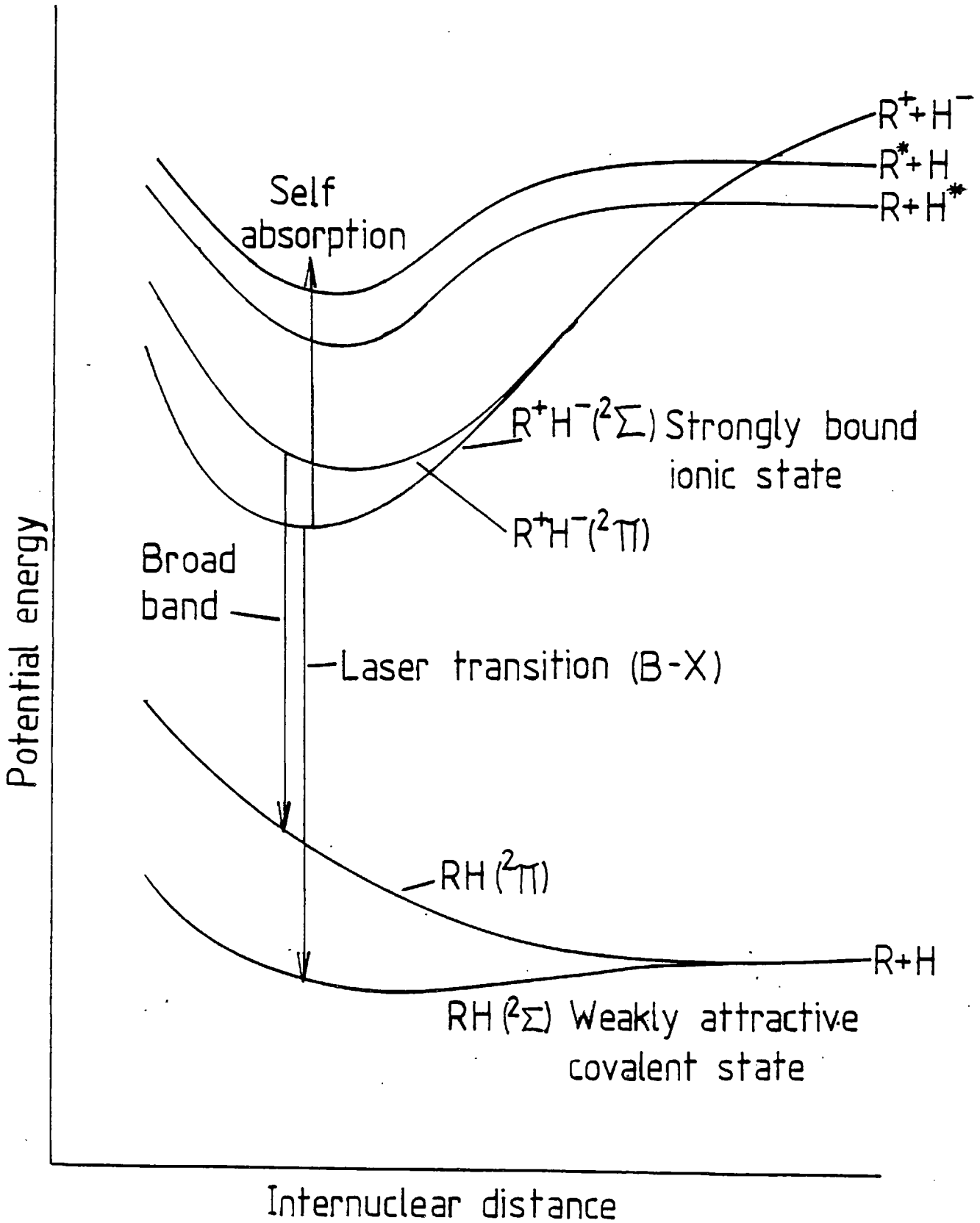


Figure 1

are found : $B^2\Sigma$ ($\Omega = \frac{1}{2}$), $C^2\Pi(3/2)$ and $D^2\Pi(\frac{1}{2})$. Ω is the sum of electronic orbital and spin angular momentum along the molecular axis.

$D(\frac{1}{2}) \rightarrow X(\frac{1}{2})$, $B(\frac{1}{2}) \rightarrow X(\frac{1}{2})$ and $C(3/2) \rightarrow A(3/2)$ radiative transitions may all occur. Generally the $B \rightarrow X$ bands show a pronounced structure due to emission from the higher vibrational states of the upper level to the fairly flat potential of the lower. However, for the $X(\frac{1}{2})$ states of XeF and XeCl bound by 1065 cm^{-1} [5] and 255 cm^{-1} [6] respectively, the primary emission band is a bound-bound transition and has resolvable vibrational and rotational structure. $C \rightarrow A$ emission has been observed in each molecule, although more weakly and at a longer wavelength[7],[8]. Since the A state is purely repulsive the transitions have a much greater bandwidth ($\simeq$ 70 nm for Xe F) than the $B \rightarrow X$ emissions (typically 2 nm at high pressure). Very weak $D \rightarrow X$ emission has also been observed, the weakness possibly being due to strong quenching of the D state[8].

Table 1 summarises the important lifetimes of the $B \rightarrow X$ and $C \rightarrow A$ transitions of the rare gas halides, either measured or calculated[11].

In addition to rare gas halide, RH, emission, further broad band emission is observable at longer wavelengths from R_2H excimers and also mixed rare gas dimers (e.g. Ar_2F or ArXeF*[9]).

Stimulated emission cross sections, depending on the emission wavelength, bandwidth and radiative decay time, have been calculated. For $B \rightarrow X$ transitions they are typically $2\text{-}5.10^{-16} cm^2$ [8], while for the longer lifetime and broader bandwidth $C \rightarrow A$ transitions a typical value is

		F		C1		Br		I	
		λ(nm)	τ(ns)	λ(nm)	τ(ns)	λ(nm)	τ(ns)	λ(nm)	τ(ns)
Xe	B-X	351	(12-19)	308	(11)	282	(12)	253	(12)
	C-A	450	(93,113)	350	(120)	302	(120)	263	(110)
Kr	B-X	249	(6.5-9)	222		206			
	C-A	275	(63)						
Ar	B-X	193	(4.2)	175					
	C-A	203	(48)	199					
Ne	B-X	108	(2.6)						
	C-A	117	(38)						

Table 1[11]

Emission wavelengths (nm) and lifetimes (ns) of the B-X and C-A transitions of the rare gas halides. Laser action has been observed on those transitions whose wavelengths are underlined.

$5.10^{-18}cm^2$ (for XeF [10]).

Laser action has been observed on many rare gas halide transitions (table 1). The formation kinetics for the upper laser level and the various pumping schemes employed to populate it will now be reviewed. Further details on these subjects, including rare gas halide spectroscopy, and a much more complete list of references, may be found in one of the many excellent review papers on rare gas halide lasers[11],[12],[13],[14].

1.2.2 Kinetics

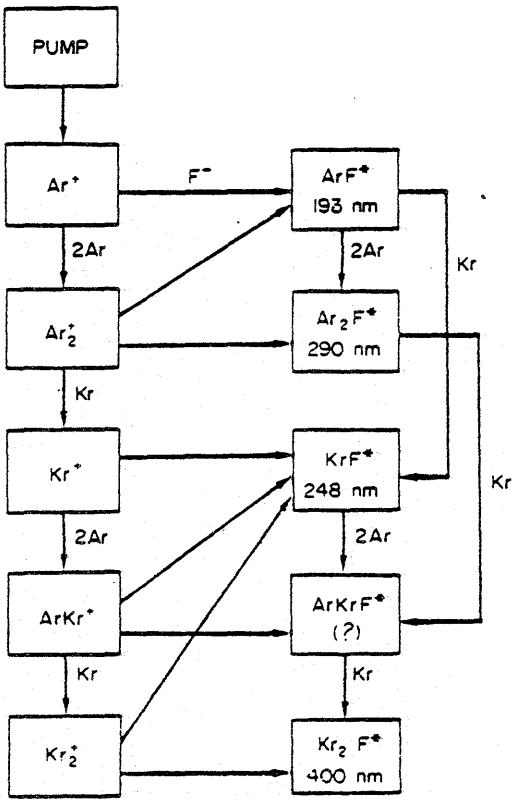
A typical rare gas halide laser contains a mixture of at least three gases. Two of these, at low number densities, provide the rare gas and halogen ions which will form the required upper laser level while the third, another rare gas at a relatively high pressure, acts as a buffer gas.

The reaction kinetics of the rare gas halide excimers are complicated and involve several ground state atomic and molecular species, several ionic species, and a large number of excited atomic and molecular species. The detailed kinetic rate to (usually) the B state of an excimer depends on the particular excimer, the halogen donor molecule, the excitation conditions, and the partial pressures of the constituent gases. Rokni et al[13] have considered in detail the formation kinetics and loss processes in electron beam and discharge pumped KrF and XeF lasers, and to give an idea of the processes involved and their complexity, their deductions for KrF will now be outlined.

First, consider the electron beam pumping (1.3.1) of a typical gas mixture Ar : Kr : F_2 in the ratio 180:20:1 at a total pressure of 1-3 Bar. Figure 2(a) illustrates the

Main kinetic routes for the formation of KrF^* (12)

(a) via ionic reaction intermediates



(b) via neutral reaction intermediates

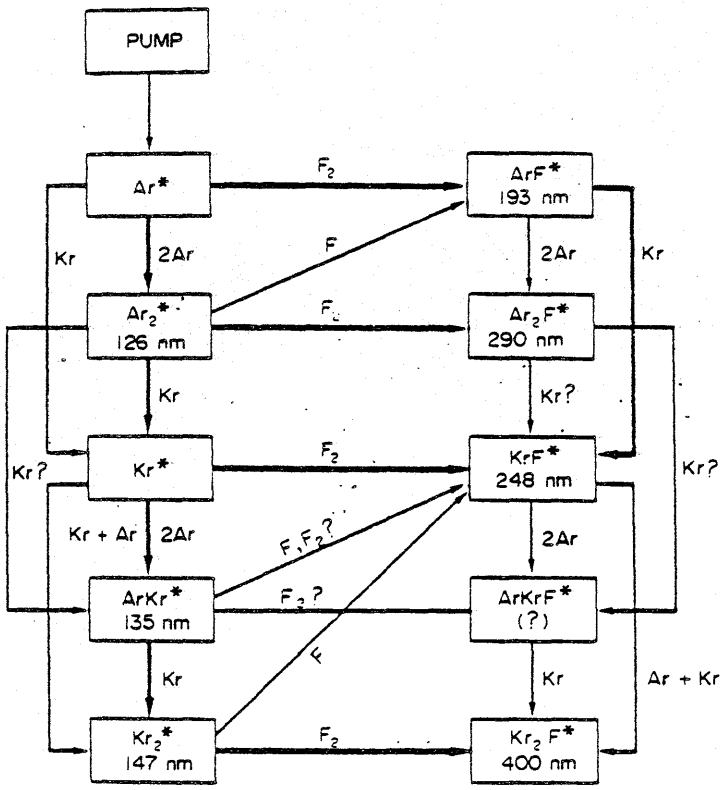


Figure 2

dominant kinetics.

Of the power deposited in the gas approximately 55% results in $Ar^+ - e^-$ pairs, and 10% in Ar* metastable states. At a typical current density of 10 A cm^{-2}, secondary electrons predominantly dissociatively attach themselves to F_2, producing F^- ions which, at pressures lower than 1 Bar, recombine with Ar^+ ions to form ArF*. However, for higher pressures and with Kr representing greater than 5% of the total, Kr efficiently exchanges with Ar in ArF* before it decays, producing KrF* in the required upper laser level.

At pressures greater than 1 Bar, 2 Ar and Ar^+ predominantly recombine in Ar_2^+ which charge transfers with Kr producing Kr^+ ions. These then combine with F^- yielding KrF* for lean Kr mixtures, but for higher concentrations Kr_2^+ preferentially forms, which then recombines with F^- to give KrF*. KrF* then either decays radiatively or is collisionally quenched.

In the case of the discharge pumping (1.3.3) of a similar gas mixture, for efficient operation the laser level is formed via the metastable channel. Secondary electrons, formed by the multiplication of primary electrons produced by UV preionization, acquire enough energy in the discharge field to excite rare gas metastables. Ar* metastables produce ArF* with a branching ratio of 0.6 via the "harpoon" reaction $Ar^* + F_2 \rightarrow ArF^* + F$. ArF* then either radiates or Kr replaces Ar as before to give KrF* The Kr* metastables, with a branching ratio of 1, produce KrF* in another harpooning reaction with F_2. Since Kr* is lower in energy than Ar*, and because of the higher branching ratio, it is preferable that more of the available energy should go into the Kr* levels. This is controlled by the Kr density and the applied field,

although increasing the Kr concentration increases its quenching of KrF* and a balance must therefore be found. For a 10% rich Kr mixture the formation efficiency of KrF* may be 35%.

In both electron beam and discharge pumping the upper laser level produced can, as an alternative to emitting laser radiation, be quenched by two or three body collisions whose rates must be low for efficient laser operation. Quenching rates for the KrF* level have been obtained by observing the B-X radiation as a function of partial pressures (table 2). The reactions which form Kr_2F^* proceed more efficiently at higher pressures, and Kr_2F^* emission is indeed observed to increase with pressure.

Further reductions in excimer laser efficiencies may be caused by photoabsorption (see table 2 for KrF). Firstly, there is photodissociation of the halogen carrier. This is important for F_2 in XeF and can be avoided, at the expense of more unfavourable kinetics, by changing the halogen donor. The second process is photodetachment by negative ions, F^-. Third is the photoionization of excited rare gas atoms and molecules and finally there is the photodissociation of rare gas dimer ions, and trimer absorption.

Analysis of the XeCl laser, which is more appropriate to the bulk of this thesis, has not so far reached the completeness of that for KrF. Levin et al[15] have, however, developed a model for the kinetics of the long pulse pumping by an electron beam of a XeCl laser, with HCl as the chlorine donor and Ne as the major diluent. Modest electron beam pump power densities of 100 kW cm^{-3} and long pulse lengths of 1 μs were considered. The B state of XeCl was formed efficiently by the ion-ion recombination of Xe^+ and Cl^-. Xe^+ was produced by a rapid three-

Table 2[13]

(a) quenching

Reaction	Rate constant
$KrF^* + F_2 \longrightarrow$ products	$7.8 \times 10^{-10} cm^3 s^{-1}$
$KrF^* + 2Kr \longrightarrow Kr_2F^* + Kr$	$6.7 \times 10^{-31} cm^6 s^{-1}$
$KrF^* + Kr \longrightarrow$ products	$\leqslant 1.7 \times 10^{-12} cm^3 s^{-1}$
$KrF^* + Kr + Ar \longrightarrow Kr_2F^* + Ar$	$6.5 \times 10^{-31} cm^6 s^{-1}$
$KrF^* + 2Ar \longrightarrow$ products	$7 \times 10^{-32} cm^6 s^{-1}$

(b) photoabsorption

Species	Cross section/cm^2
F^-	5.6×10^{-18}
Kr_2^+	1.6×10^{-18}
Kr_2F^*	1.6×10^{-18}
Ar_2^+	1.3×10^{-17}
Ar**,Kr**	6×10^{-18}

Dominant KrF* quenching and photoabsorption processes

body charge exchange process between Ne_2^+ and Xe, while the Cl^- was the result of rapid electron attachment to vibrationally excited HCl. This vibrationally excited HCl (v = 1), produced by secondary electron interaction with ground state HCl, has a 40 times greater dissociative attachment rate constant than the v = 0 level. For the conditions considered Cl^- was identified as the major absorber of the XeCl* emission.

In the electron-beam sustained discharge pumping of both XeCl and KrF, which is to be described, the upper state is predominantly reached via the metastable route, but it is apparent that as the enhancement ratio (the ratio of the energy deposited in the gas from the discharge to that from the electron beam) of the system is reduced, the contribution from the ionic route will increase.

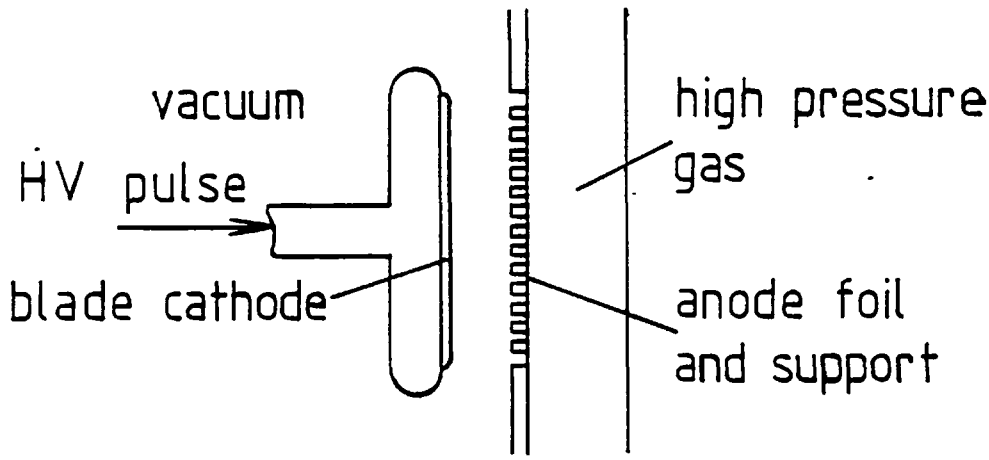
1.3 Pumping of excimer lasers

Four main techniques have been employed to pump the rare gas halide excimers : direct electron beam pumping, electron beam sustained discharge pumping, UV preionized (avalanche) discharge pumping, and X-ray preionized discharge pumping. These will now be considered in turn, with a greater emphasis on the first and second, since these relate most directly to the subject of the following chapters. The novel technique of the microwave excitation of excimer lasers will also be briefly discussed.

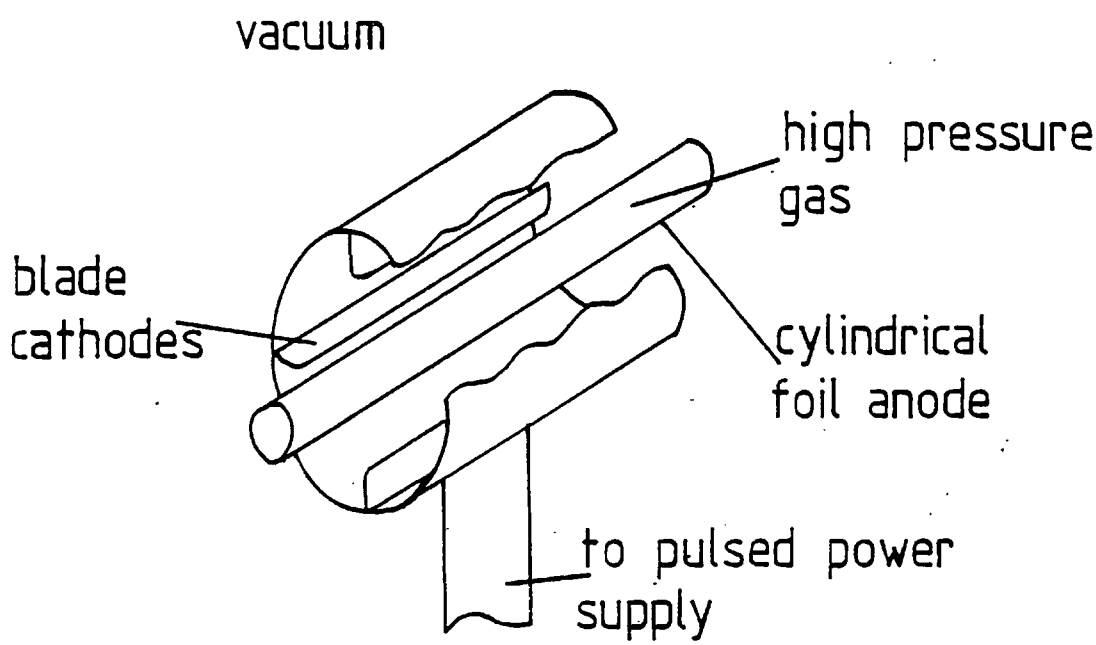
1.3.1 Direct e-beam pumping

A laser pumped by a high intensity relativistic electron beam is shown schematically in figure 3. The electron beam

Electron beam pumping geometries



(a) transverse



(b) coaxial

Figure 3

source consists of a pulsed high voltage power supply, a vacuum diode which forms the beam, and a window through which the electrons enter the gas.

This technique was originally used to pump the pure rare gas excimers with emissions in the vacuum ultraviolet. In the case of the longer wavelength, narrower bandwidth, rare gas halide excimers, the pumping powers required are much less. Also, the rare gas halides operate efficiently at much lower pressures than the pure rare gas excimers, and so a typical gas mix has a much lower stopping power for electrons. This often means that, even with a lower voltage electron beam, a proportion of the beam traverses the gas chamber completely and is lost to the cell walls.

High voltage pulsed power supplies are usually comprised of two parts, the HV generator section and the pulse compression or shaping section. High voltages are most commonly achieved with either a Marx generator or a pulse transformer, both of which provide voltage multiplication. They are energised by HV capacitors slowly charged to a voltage which is many times less than the output of the complete pulsed power supply.

In a Marx generator[16]-[19] a bank of capacitor stages is slowly charged in parallel and then rapidly discharged in series by means of spark gaps. Figure 4 shows a schematic diagram of a typical five stage Marx generator. If the charging voltage is V_{in} across N stages, then the output voltage is approximately given by $V_{out} = N\, V_{in}$.

Pulse transformers for high voltage generation are usually, but not exclusively, air cored and are often in the form of an autotransformer[20],[21]. The primary of such a transformer is energised by the discharge of a HV capacitor through a spark

Electrical schematic of a 5-stage Marx generator

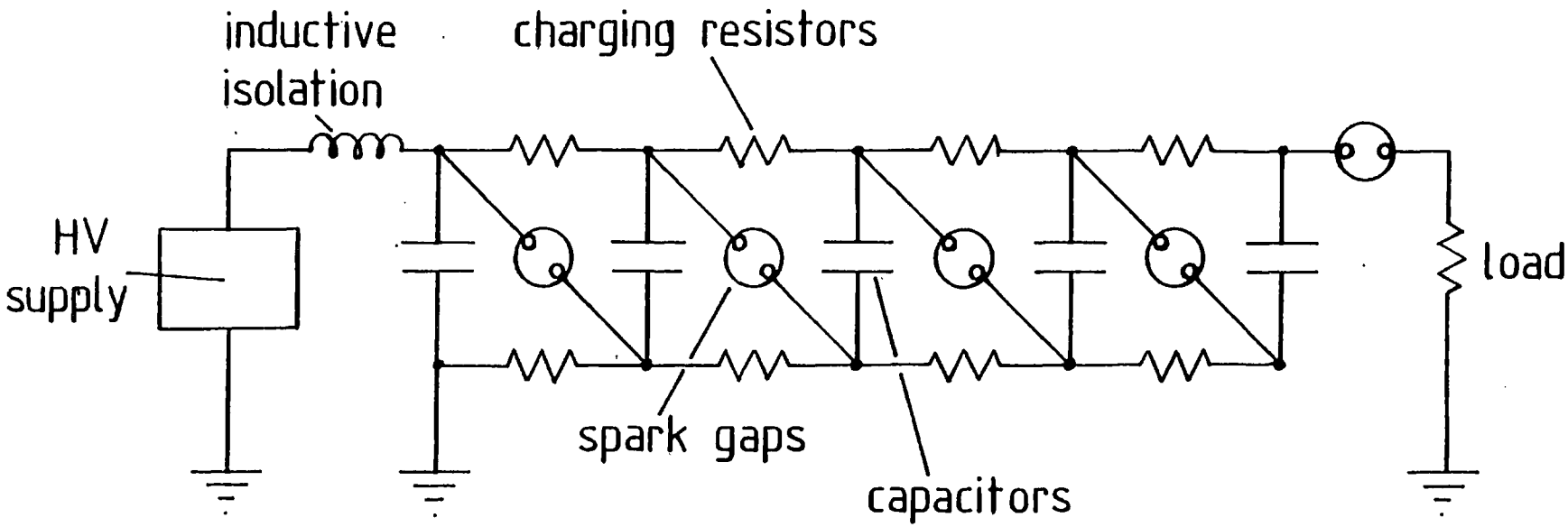


Figure 4

gap. Voltages of up to 5 MV can be generated in this way from a system which is much simpler and smaller than an equivalent voltage Marx generator. Transformer reliability has also been shown to approach that of a well-made Marx generator, if care is taken over its construction, and reasonably high repetition rates are possible[22]. The output voltage pulse from such a transformer has an approximately $(1 - \cos\omega t)$ form with possibly a several hundred nanosecond risetime and some pulse forming or compression is usually necessary.

This pulse shaping is achieved, for either the transformer or the Marx generator, with a pulse forming network, such as a simple water- or oil-dielectric transmission line, or a Blumlein pulse forming line[23]. A Blumlein pulse forming line supplies an output voltage into a matched load which is almost equal to its charging voltage, whereas the single pulse forming line, although simpler in construction, supplies only one half of this. These techniques allow the tailoring of fast rising and falling voltage pulses with durations governed only by the geometries of the lines.

The output voltage pulse is fed to the cathode of a vacuum diode. A spark gap may be inserted between the power supply and the diode to prevent voltage reaching the load before charging of the pulse forming line is complete - the phenomenon of prepulse. In the vacuum diode the electron beam current density is typically 5-500 A cm^{-2} over the area of the cathode, with total currents of 5-50 kA in pulses of 50 ns - 1 μs. Cold cathodes rather than thermionic emitters are necessary for such high current densities over large areas. The electrons are emitted by a zero work function plasma which forms over the surface of the cathode when a high voltage gradient is applied[24]. The current density is then space-charge limited

by Child's Law[25] and the electrons enter the laser cavity through a thin, 25-50 μm, foil with hopefully small loss of energy. The transverse geometry of figure 3 is most common, but axial geometries (in which the electron beam is injected near one end of the laser and guided along the axis by a magnetic field) and coaxial geometries have also been used. In the latter (figure 3), more uniform energy deposition is obtained by containing the gas in a thin-walled tube which is concentric with a cylindrical cathode.

Ionization of the diluent gas is the main form of excitation by the electron beam. If an amount of energy W is required to form an ion-electron pair, and if ν is the laser photon frequency, then $h\nu/W$ defines the quantum efficiency. For example, in KrF with an Ar diluent this is 25%. Other losses significantly reduce this figure, but a 15% intrinsic efficiency has been reported in a 150 ns coaxial KrF laser[26].

1.3.2 E-beam sustained discharge pumping

In an electrical discharge, a field E is applied to a gas of number density N. For rare gas halide excimers the levels of E/N required for efficient excitation of the rare gas metastable levels are also sufficient to produce rapid ionization from these excited states by $R^* + e^- \rightarrow R^+ + 2e^-$. This means that high pressure discharges are inherently unstable. However, this problem can be circumvented with the electron beam ionized, attachment stabilised, discharge technique in which the rapid attachment rate of electrons to the laser medium to be excited is kept above the rate of regenerative ionization of the discharge. Electrons are lost mainly by attachment to the halogen atoms/molecules present in the laser medium, and it has been shown[27] that if this attachment rate is greater than twice the rate of ionization by the two step process

Simplified e-beam sustained discharge pumping geometry

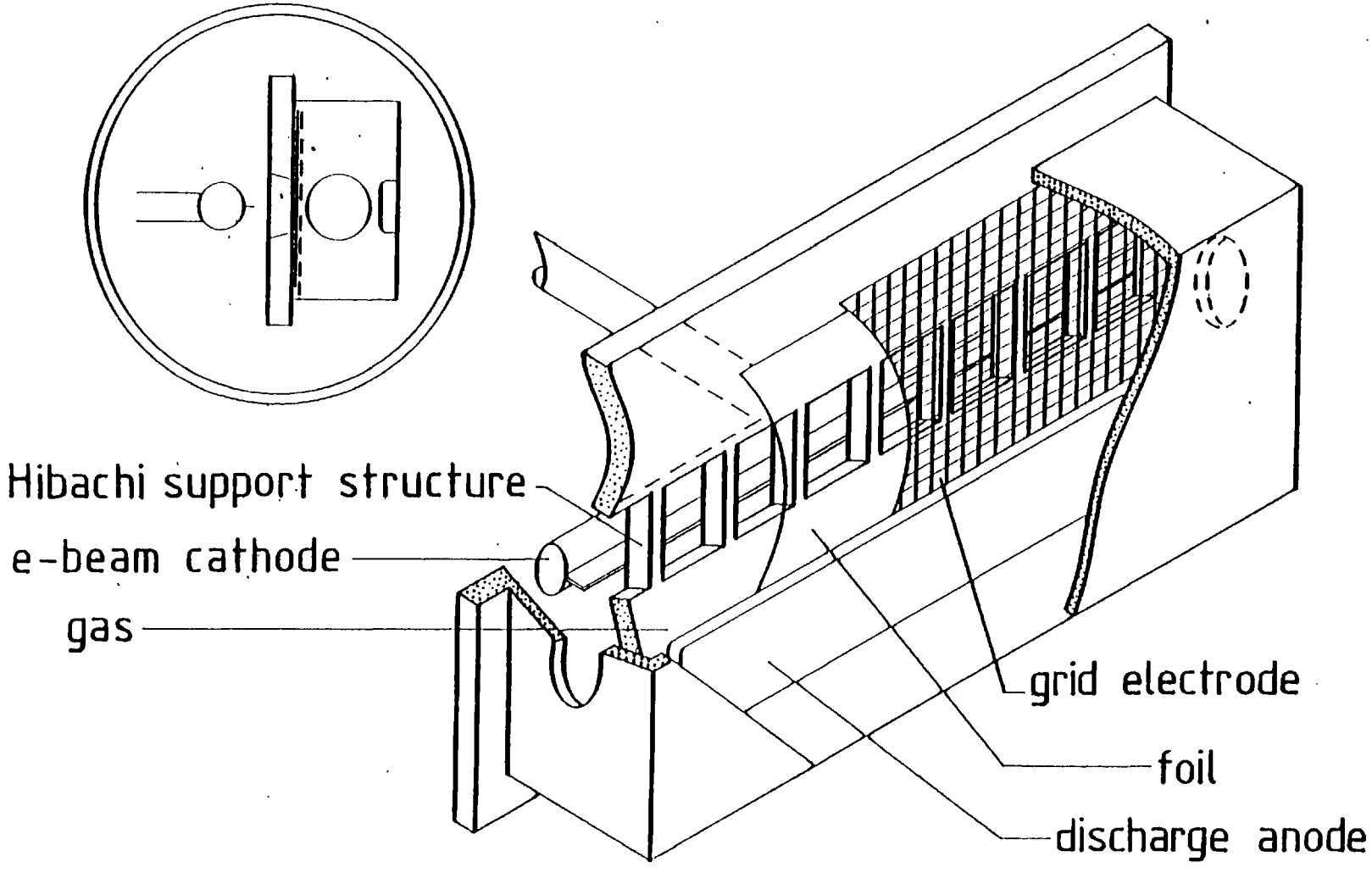


Figure 5

indicated, the discharge will be volumetrically stable. For a steady state, the difference of the two rates must be made up from an external ionization source, viz. an electron beam, a typical arrangement for which is given in figure 5.

An enhancement ratio is a measure of the success of e-beam sustained discharge lasers. It is defined either as the ratio of the electrical input power to the laser medium from the discharge to that from the electron beam or as the ratio of the respective laser output powers obtained. Within discharge stability limitations this first ratio can be in the range 5-10 [27].

This pumping scheme has several advantages over pure electron beam pumping. The quantum efficiency is, in this case, the ratio of the photon energy to the atomic excitation energy, since metastable atoms are the main precursor. For KrF this is $\simeq 0.5$, or twice the value for the electron beam alone. Also, because the discharge plasma has a well defined, if low ($< 1\Omega$), impedance, relatively efficient electrical coupling from the discharge circuit to the plasma should be possible. Hence, because most of the pump energy is supplied by the discharge, these systems should ultimately have higher efficiencies than electron beam pumped lasers. Further, the technical problems of building and running a smaller electron beam generator plus discharge are also much less than those of a high voltage, high current density electron beam generator alone.

1.3.3 Avalanche discharge pumping

Although unsustained discharges are inherently unstable, there is a short period of time (a few tens of nanoseconds at several atmospheres) when the plasma impedance is relatively high and the discharge uniform before the rapid multiplication

of electrons in the high electric fields leads to the growth of arcs from spatial non-uniformities and impedance collapse. Fast, transverse discharges have been used very successfully to pump lasers over this limited period and have produced energies of Joules in pulses of 10-40 ns[28]. The techniques of low inductance capacitor dumping[29]-[31] and, less often, LC inversion networks[32],[33] have been most commonly used for pumping. Preionization of the gas with UV radiation has also been frequently used to suppress the growth of non-uniformities[32]. The spark gaps producing the preionization are either mounted along the side of the discharge channel, although this may result in some non-uniformity of preionization and discharge constriction, or behind a screen forming one of the main discharge electrodes[31].

These lasers have been rapidly developed as relatively cheap, very reliable commercial sources of high power UV laser light. They have become especially important for the pumping of dye lasers[34]. A typical commercial system[35] operating on KrF supplies pulses of up to 1J at a maximum power of 20W and an efficiency of less than 2%. The maximum repetition rate is 25Hz, the beam divergence 2x4 mrad and the gas fill lifetime greater than 10^6 shots.

1.3.4 X-ray preionized discharge pumping

This relatively recent[36] alternative to ultraviolet preionization has the advantage of scalability in high pressure lasers. Due to the very small collision cross section of X-rays, ionization of large volumes is possible. The spatial homogeneity of the X-ray induced preionization has allowed avalanche discharges to be run for up to 200ns[37],[38],[39] before instability sets in.

In general, the X-rays are generated by an electron beam striking a target made of material with a high atomic number. A specifically low voltage, low energy X-ray source has also been developed for preionization studies[40] and can operate at up to 35Hz. Similar high pressure, high repetition rate work with e-beam or e-beam sustained discharge pumping is limited by the mechanical strength and heat transfer properties of the foil. With the new technique, large volume kHz operation may be possible[40].

1.3.5 Microwave pumping

Successful microwave pumping of excimer lasers has been reported[41]. $\simeq$2 μs long, 9.375 GHz microwave pulses have produced $\simeq$500ns of spontaneous emission and 100ns laser pulses from the XeCl excimer. More recent work by the same group has increased the laser pulse length to 200ns[42]. In both cases the efficiency was an order of magnitude lower than that of a typical avalanche discharge system.

Microwave excitation of high pressure gases has several important advantages over avalanche discharge pumping : the power deposition is nominally independent of gas composition, uniform preionization is not critical, and even a breakdown or arc does not prevent effective excitation in other regions of the plasma. Further, such a device is easily constructed with high-vacuum, halogen-compatible materials and does not have electrode sputtering problems.

Until efficiencies are improved, such a long pulse laser may be most useful for the generation of well controlled (spatial/temporal/spectral) pulses for injecting into a high power amplifier chain.

1.4 Objectives of this work

It has been shown that for high output energy laser operation in a long pulse the electron beam sustained method of pumping the rare gas halides has some definite advantages over pure electron beam pumping. An electron beam sustained discharge laser system was therefore developed both to study further the limitations of this pumping technique and to be used in a number of other experiments, especially concerning short light pulse generation in the UV.

1.4.1 Laser development

The laser was designed after a study of the published literature concerning the e-beam and e-beam sustained pumping of the XeCl excimer (the excimer for which most sustainer information was available).

Ewing and Brau, in 1975[43], first observed lasing on the $B \rightarrow X$ transition of XeCl at 308 m. $\simeq$ 2J of purely e-beam energy was deposited in an Ar:Xe:Cl_2 mixture, but peak outputs of only 50 μJ were obtained. The output spectrum was made up of two peaks, now known to be the (0,1) and (0,2) vibrational bands of $B \rightarrow X$ at 308.0 and 308.2 nm. Cl_2 and Ar_2^+ absorptions at 308 nm were identified as major limiting factors on the system efficiency, and the donor and buffer gases were eventually replaced by HCl and Ne by Champagne[44]. This allowed a 5% extraction efficiency to be reached. Somewhat contradicting this, however, is the comprehensive study of halogen donors and diluent gases carried out by Losev et al[45] in which Ar and Ne were found equally effective.

XeCl was first pumped in an e-beam sustained system by Levatter et al[46], who reported efficiencies approaching those of KrF on the same system. Their e-beam delivered

20 kA at up to 225 kV for 0.3-3 μs through a 10 x 120 cm^2 foil window into a 6 l discharge with electrodes 5 cm apart. For an operational gas mix with an Ar diluent and 8 Acm^{-2} of electron beam entering the gas output energy densities of 0.02 Jl^{-1} and 0.5 Jl^{-1} for sustainer voltages of 0 and 30 kV respectively were found. The output increased rapidly with sustainer voltage and was limited only by the self-breakdown threshold of the cavity. An enhancement ratio of 25 was claimed as a measure of the success of the system, but this is somewhat misleading. In fact, the ratio of deposited energies was only $\simeq 2.4$, and the factor of 25 reflects more on the low electron beam efficiency. Clearly, an arbitrarily high ratio, using the output energy definiton, could be obtained by running the system such that it was below threshold for e-beam pumping alone, but above it for sustained operation.

Rothe et al[47] first investigated the use of Ne as a diluent in sustained discharges and they recorded extraction efficiencies which were almost an order of magnitude above those of Levatter et al[46]. In a Ne:Xe:HCl gas mix, 38 A cm^{-2} of 270 kV electrons produced a 0.7J pulse in 200 ns from a 100 cm^3 extraction volume (4.2% extraction efficiency). In the sustained mode with the discharge electrodes now 3 cm apart and for a 160 cm^3 extraction volume, a 1.5 J output was achieved at a 4.5% efficiency. The enhancement ratio, by either definition, was $\simeq 2$. Efficient, high output power operation in a long pulse was therefore achieved but, because of the low enhancement ratio, at the expense of needing a complicated, high current density, electron beam generator.

To summarise, XeCl has been developed to the stage where its efficiency of performance matches that of XeF or

KrF, but its kinetic and photoabsorption processes are not, as yet, well understood. Notably, the replacement of Ar by Ne as the buffer gas, which originally seemed to lead directly to order of magnitude increases in efficiency, does not now seem so clear[45]. If the results of Oomen et al[48] for the increase in laser output power in KrF, found by using a mixture of diluent gases, can be applied to other rare gas halide excimers, then this should lead to further increases in laser efficiency.

An electron beam sustained discharge laser was therefore developed from a consideration of the above and from preliminary work done on a versatile system developed for the pumping of the rare gas and rare gas halide excimers in both long and short pulse modes[49]. Chapters 2 and 3 will describe this work in some detail and show how careful design allowed an efficient, high power, reliable laser to be developed.

1.4.2 Short pulse generation

Short-duration optical pulses in the ultraviolet find potential application in the study of rapid kinetic processes, optical pumping of short-lived atomic and molecular states, and enhancement of non-linear effects such as frequency multiplication and multiphoton spectroscopy. For a number of these applications it is essential that the optical pulse exhibits high energy as well as short temporal duration. An ideal way of achieving this would be the mode-locking of an excimer laser, where the laser energy is extracted in a series of short pulses separated by the round-trip time of the cavity.

Chapters 4-6 will introduce this concept in greater detail and describe the short pulse generation experiments carried out with the long pulse e-beam sustained XeCl laser. Chapters 4

and 5 will concentrate on the techniques of fast optical shutters and especially the problems of repetitively driving them at a frequency equal to the inverse of the cavity round-trip time. Chapter 6 will then report the mode-locking results obtained with a number of shutters and the negative results obtained with saturable absorbers.

Finally, Chapter 7 will briefly summarise the important results and propose both improvements to the completed experiments and new experiments which could usefully be performed with the XeCl laser.

CHAPTER 2

AN ELECTRON BEAM GENERATOR

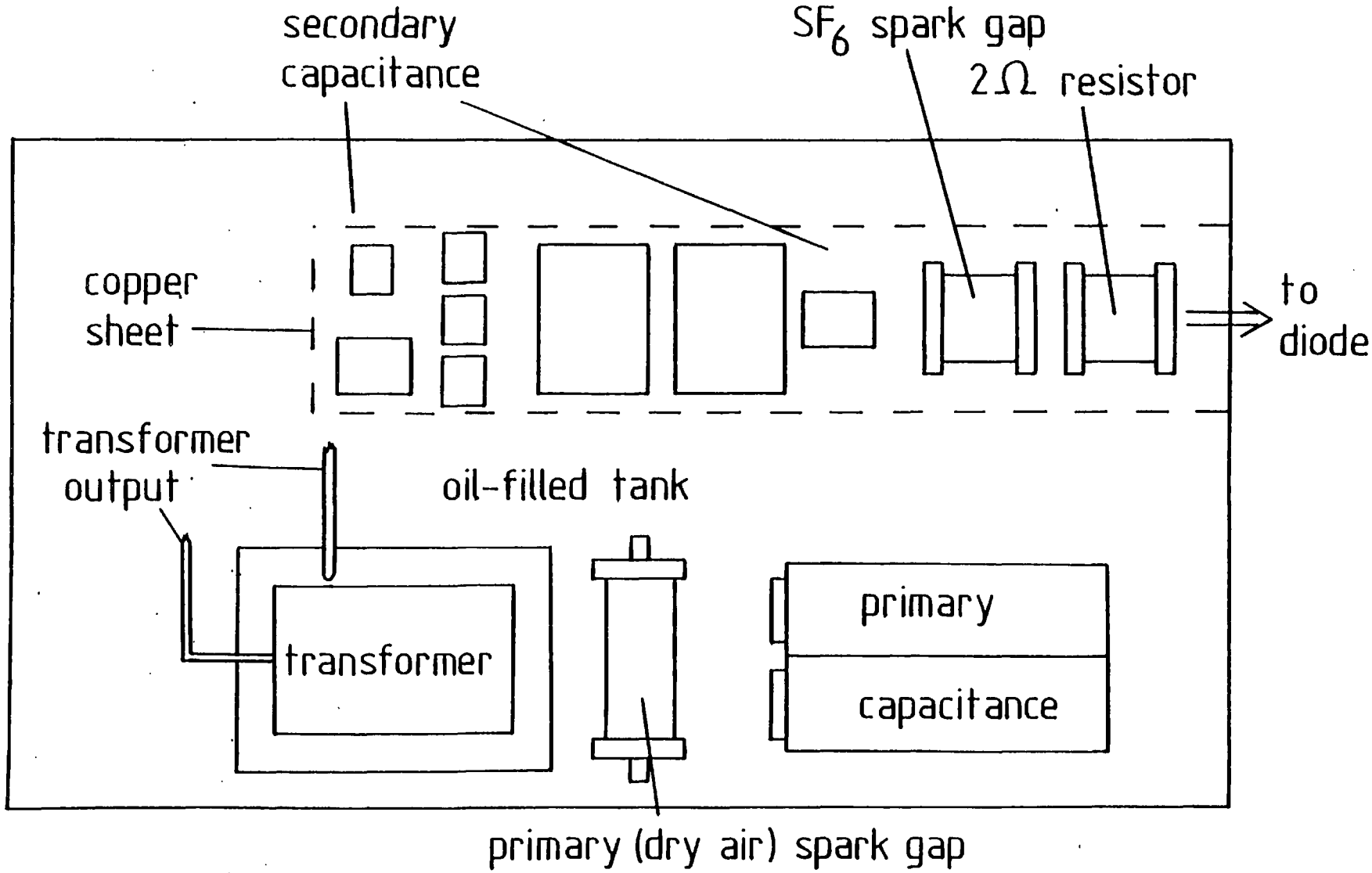
2.1 Introduction

This chapter will describe the development of an electron beam generator to be used in the e-beam sustained discharge pumping of an XeCl laser. A detailed description and performance study for the high voltage pulsed power supply will be followed by a similar consideration of the electron beam diode.

The particular design of the generator was chosen in the light of the results of the National Research and Development Corporation Programme No. 109552 entitled, "Gas Lasers for the Ultraviolet Wavelengths"[49].

In this project a single pulsed power supply was developed for use with three easily interchangeable laser heads. Two of the laser heads used coaxial electron beam diodes to pump the rare gas and rare gas halide excimers respectively, while the third allowed the long pulse pumping of the rare gas halides by the e-beam sustained discharge technique.

High voltage generation was achieved with an autotransformer. For short pulse operation this charged a Blumlein pulse forming line, while the transformer was connected directly to the output of the power supply in the long pulse case. Employing techniques similar to those which will be described later in this chapter, the long pulse output from the power supply generated a transverse electron beam which allowed the sustained discharge operation of an XeCl laser. The diode voltage reached a peak value of 300 kV in a 400 ns F.W.H.M. pulse, and 7 A cm^{-2} of electron beam current was transmitted into the laser cavity. This allowed a laser output of 300 mJ in a 110 ns pulse to be extracted during sustainer operation.



Pulsed power supply layout

Figure 6

For this system, increasing the electron beam current density entering the laser cavity was observed to steadily increase the obtainable laser output power. Similarly, the pulse length of the laser output varied with the duration of the electron beam current pulse. Since neither of these parameters could easily be increased further on the available system, it was decided to redesign the pulsed power supply. The new pulsed power supply was to be operated purely in the long pulse configuration, and the design goals of the complete generator were a much higher electron beam current density transmitted into the laser cavity in a substantially longer duration pulse.

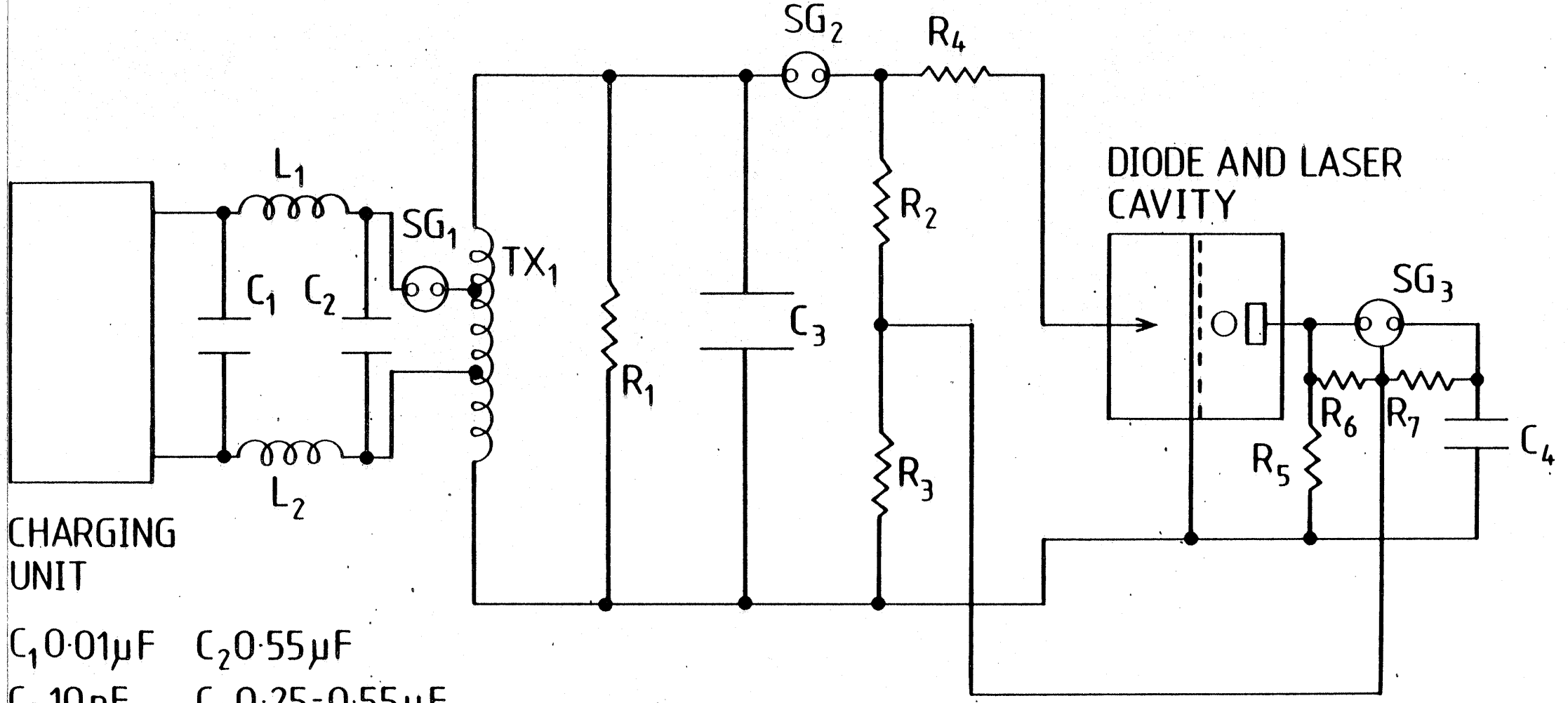
2.2 Description of the pulsed power supply

Figure 6 shows schematically the lay-out of the pulsed power supply, housed in an oil-filled tank of dimensions 0.66 x 1.22 x 1.48 m^3. In summary, a secondary capacitance was charged from a much larger primary capacitance via a transformer used to provide voltage multiplication. When the first peak of the charging curve of the secondary capacitance was reached, a switch closed and it was discharged into the load, consisting of either copper sulphate resistors or the e-beam diode.

An electrical circuit diagram for the complete system (including the discharge) is given in figure 7.

2.2.1 The pulse transformer

The basis of the power supply was a simple 8:1 turns ratio pulse transformer TX_1. This was a copper foil-wound autotransformer insulated with polyester film (0.25 mm thick "mylar") and constructed as follows. The copper foil windings



C_1 0·01μF C_2 0·55μF

C_3 10nF C_4 0·25-0·55μF

$L_{1,2}$ 1·4mH

Circuit diagram of the complete system

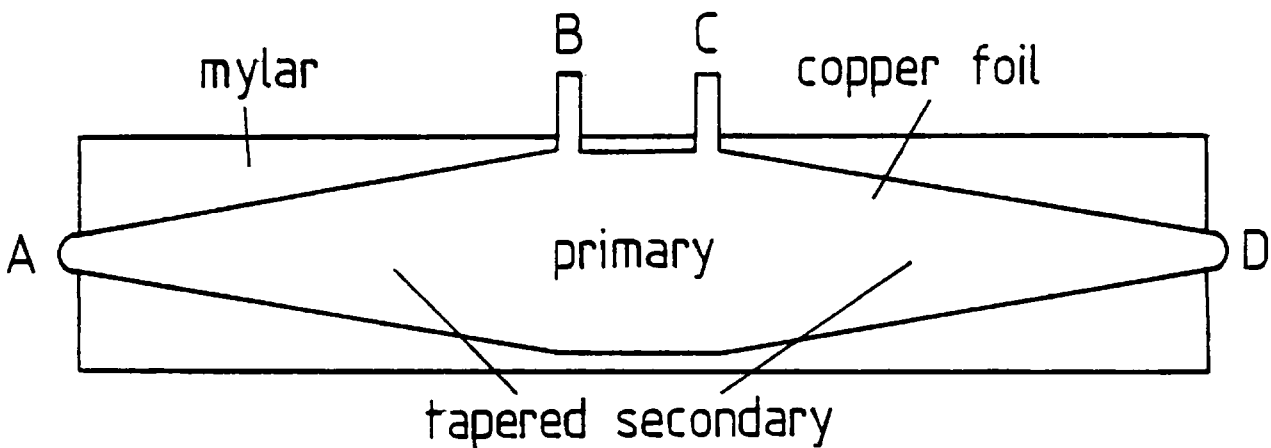
Figure 7

were tapered, as shown in figure 8(a), and wound tightly, with the insulator, on to a 25 cm long, 15 cm diameter perspex cylinder, as shown schematically in figure 8(b). 10.5 turns of 0.076 mm thick copper were first wound on to the cylinder, beginning at a width of 2.5 cm and tapering out to 15.2 cm. These comprised one half of the secondary, the inside turn of which was fed through the wall of the perspex cylinder and became the HV output. Following this was the primary, 3 turns of 0.127 mm thick copper, 15.2 cm wide and with two feeds leading to the beginning and end of the 3 turns (fig. 8(a)). The second 10.5 turns of the 0.076 mm thick secondary were finally wound, again tapering down from a width of 15.2 cm to 2.5 cm. A single 22.9 cm wide, rectangular piece of 0.25 mm thick mylar was wound between every turn for insulation. Electrical connection between the primary and secondary was simply made by folding the overlapping ends together, and care was taken that the turns did not contain any sharp projections, especially at the edges.

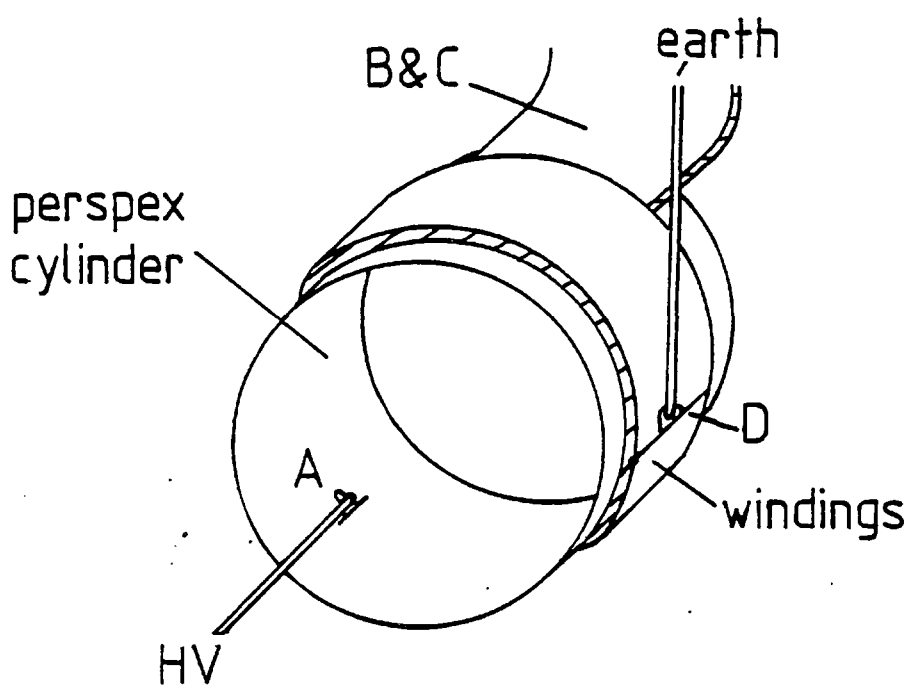
Tapering of the secondary windings caused the internal distance from primary to secondary to increase as the number of secondary turns increased, thereby improving the breakdown characteristics of the transformer. It also improved the flux linkage between the primary and secondary, minimising the leakage inductance of the transformer.

After the winding was completed, the turns being held together with strings of cable ties, the transformer was placed on two cradles in a perspex box of dimensions 34.5 x 23 x 23 cm^3 and covered in transformer oil. The whole box was then placed in a chamber and evacuated. This ensured complete extraction of air from between the transformer turns and its replacement with oil for greater dielectric strength. Copper sulphate

Simplified transformer construction diagrams



(a)



(b)

Figure 8

impregnation, which is important for high voltage transformers, proved unnecessary at the voltage levels to be used with this transformer. A fuller description of the design problems associated with the manufacture of pulse transformers has been reported by Martin et al[50].

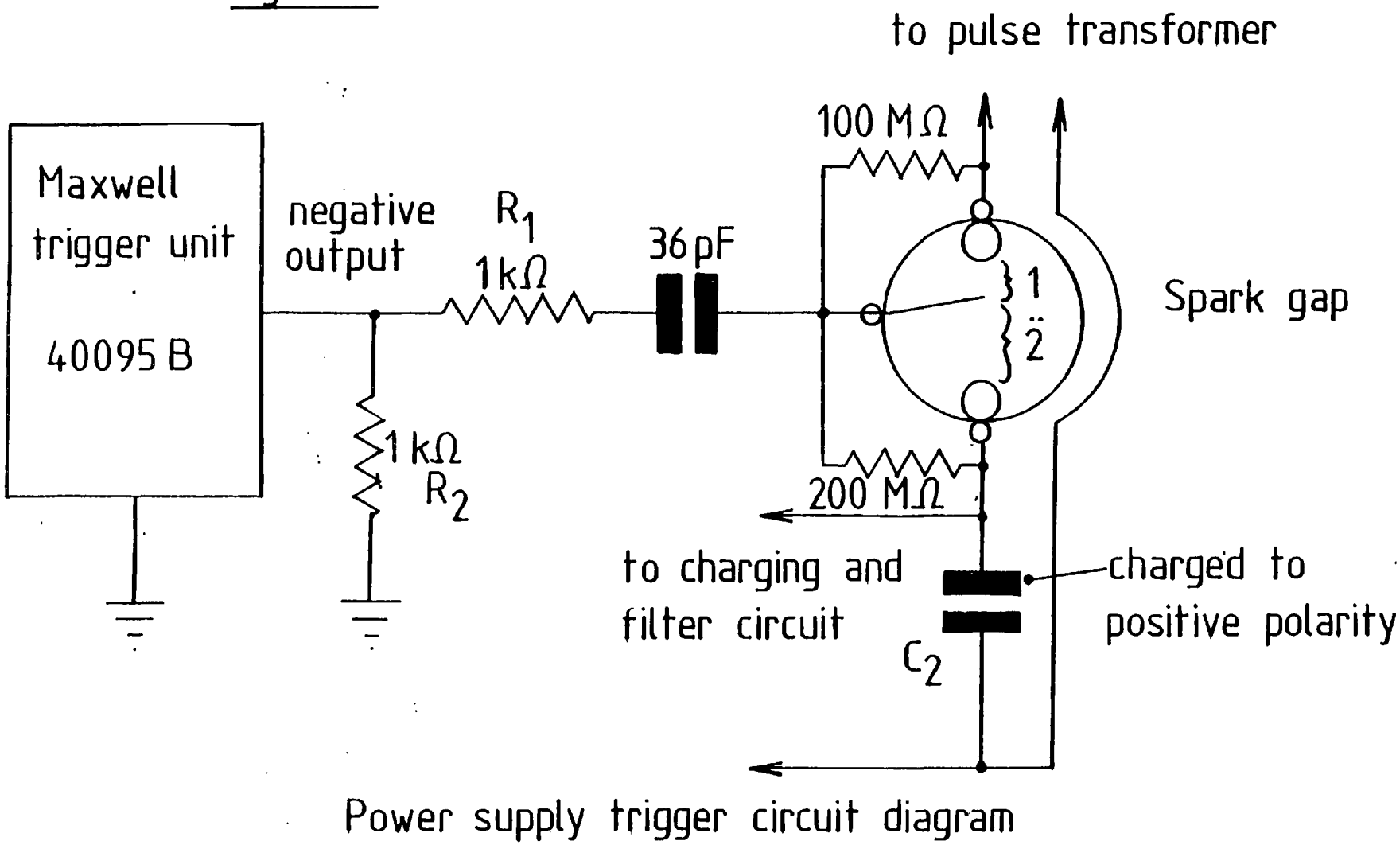
2.2.2 The primary circuit

The primary capacitor bank C_2 (see fig. 7) consisted of a 0.3 and 0.25 μF rapid discharge capacitor connected in parallel. It was charged by a Hartley Measurements Ltd., 200 Js^{-1}, 50 kV charging unit via the inductors L_1 and L_2. These inductors, together with the capacitor C_1, comprised a D.C. filter network which prevented energy from the primary of the autotransformer from feeding back to the charging unit after the primary gap had fired. This would have occurred because the potential of the transformer primary rose to one half of the total transformer voltage on firing. C_2 was connected with 15.2 cm wide copper foil to the feeds of the primary winding via the primary spark gap SG_1. The feeds were wrapped with insulating mylar, which permitted them to be sandwiched together and minimised the inductance of the primary circuit.

Primary spark gap SG_1 consisted of a 4 cm diameter cylinder of perspex in which were mounted two stainless steel rail electrodes, 8 mm apart, and a trigger blade electrode. The trigger blade was set parallel to the main cylindrical electrodes and at a spacing ratio of 2:1 between them, closer to the transformer (output) side. Gas connections at either end of the perspex cylinder allowed pressurisation with dry air. Pressure sealed studs made electrical connection between the electrodes and the external circuit.

In order to trigger the power supply, after the charging

Figure 9



Power supply trigger circuit diagram

of C_2, an isolated Maxwell trigger unit was used (Model no. 40095B). This unit delivered a pulse of up to ± 100 kV, with a throughput delay and risetime of $\simeq$100 ns. The unit itself was triggered with a 3-10V external pulse or manually by contract closure. Since the trigger electrode also rose up to one half of the transformer output voltage on firing, it was necessary to prevent energy feeding back into the trigger unit. Figure 9 shows the coupling circuit employed. Two 1 kΩ copper sulphate resistors were used to halve the size of any back transient from the spark gap to the trigger unit. The magnitude of the resistors was chosen so that the time constant produced by multiplication of the series 1 kΩ resistor and the trigger electrode capacitance, $\simeq$ 10 pF, was small compared to the risetime of the trigger pulse. An oil filled 36 pF coaxial capacitor isolated the trigger unit from the spark gap.

The trigger pulse was of negative polarity, opposite to that of the charging voltage on C_2. The potential of the blade, before firing, was automatically set to one third of the voltage on C_2 with a potential divider formed by the 200 MΩ and 100 MΩ resistors of figure 9. The complete arrangement gave the best jitter and delay to trigger performance of the overall triggering system[51].

A risetime of 100 ns was measured for the output pulse from the Maxwell unit, while the minimum time to trigger for the power supply was $\simeq$200 ns.

The spark gap pressure was set at 22 psi above atmospheric, with C_2 charged to 46 kV, to just prevent self-breakdown.

2.2.3 The secondary circuit

Secondary capacitance C_3 was charged directly from the HV output of the transformer. Spark gap SG_2 connected C_3 to the

load and was set to break down at the first peak of the output of the transformer.

C_3 consisted of eight capacitors connected in series, to give a low capacitance with a high voltage stand-off. A total measured capacitance of 9 nF was made up of 6 x 100 nF, 1 x 40 nF and 1 x 46 nF individual capacitors. R_1 was a chain of copper sulphate resistors which ensured that the output from the transformer was correctly shared between the capacitors. Resistors of 1.4 kΩ were strapped across the larger capacitors and 2.8 kΩ across the smaller, making a total R_1 of 14 kΩ. The capacitors were connected together with brass plates, and to the HV of the transformer with 0.64 cm diameter copper tubing.

SG_2 was a simple two electrode spark gap pressurised with SF_6. It had two smoothed cylindrical brass electrodes which were set with their flat faces parallel and 1 cm apart. A perspex housing with non-metallic gas connections allowed gas pressurisation and exhaust. Pressure sealed studs again permitted connections to be made to and from the spark gap, which was pressurised to typically 20 psi above atmospheric.

The output from SG_2 was taken via a brass plate feed and 2Ω copper sulphate resistor either to the electron beam diode or to a dummy load. The 2Ω resistor was a spark gap of the same design as SG_2 but filled with copper sulphate solution. It limited the amount of current which could be drawn from the power supply if a short circuit was to develop in the load (of a few tens of ohms). This was especially important when trying to limit the current which might be drawn into an instability in the electron beam diode.

Finally, the earth connection was made from C_3 to the diode with a 17.8 cm wide sheet of thick copper foil. This was run closely across the top of the capacitor bank to ensure as

low an inductance for the secondary circuit as possible.

2.3 Performance of the pulsed power supply

A theoretical and experimental study was made of the pulsed power supply performance. The theoretical results to be described are a combination of those developed for the N.R.D.C. report 109552 and provided independently by J.C. Martin[52].

The transformer and associated components can be represented by the equivalent circuit of figure 10. A Laplace transform analysis of this circuit leads to a relationship which can be used to calculate the expected transformer performance. If v(t) is the voltage on C_3 as a function of time, then it is found that, in the underdamped case :

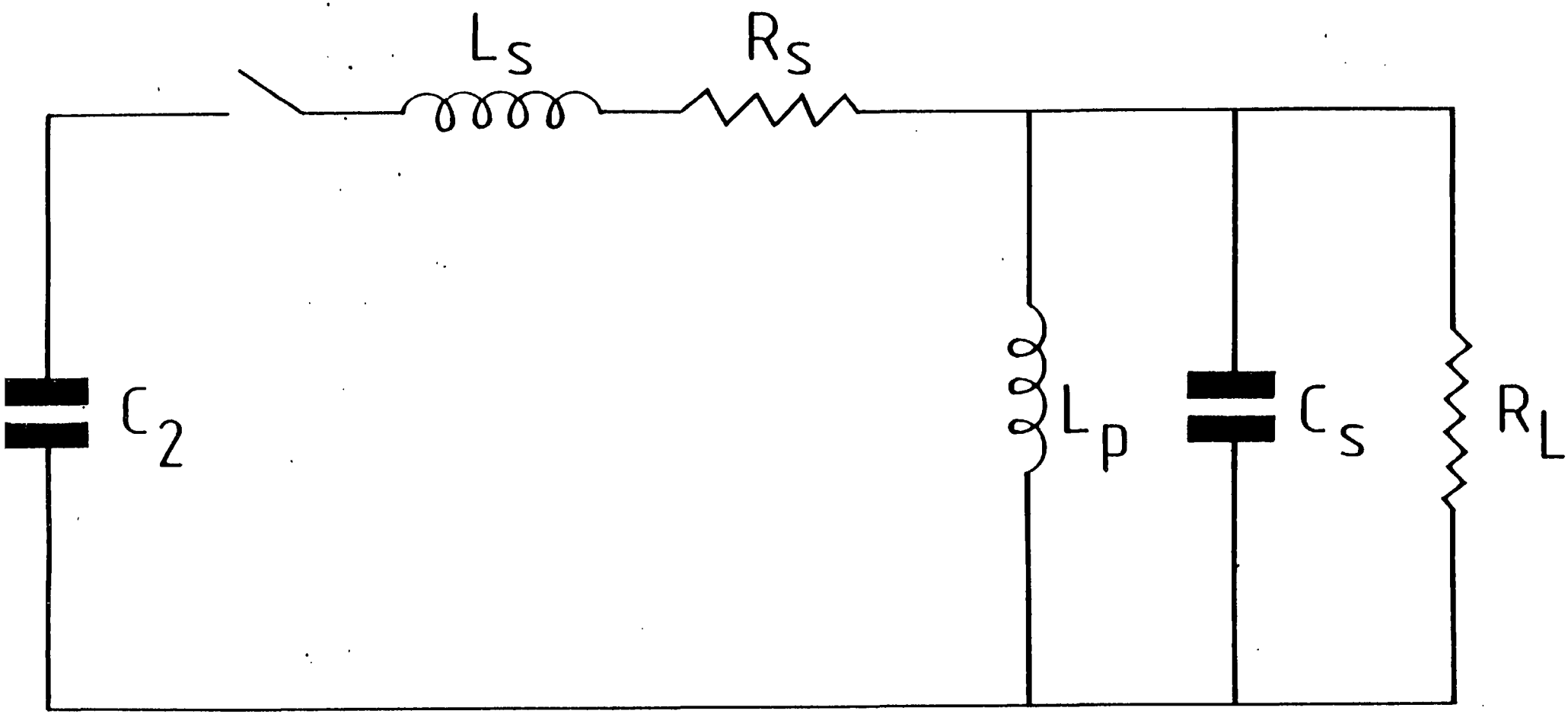
$$\frac{v(t)}{V_{C_2(0)}} = \frac{1}{L_s C_s} \cdot \frac{1}{(\omega_1^2 - \omega_2^2)} [\cos(\omega_1 t)\exp(-\alpha t) - \cos(\omega_2 t)\exp(-\beta t)] \qquad (2.1)$$

where $V_{C_2(0)}$ is the initial voltage on C_2,

$$\omega_1 = \sqrt{\frac{C_2 + C_s}{L_p C_2 C_s} - \alpha^2} \quad , \quad \omega_2 = \sqrt{\frac{1}{L_p (C_2 + C_s)} - \beta^2}$$

$$\alpha = \frac{R_s}{2 L_s} \quad \text{and} \quad \beta = \frac{1}{2 R_L C_s} .$$ C_2 is the primary capacitance, L_s is the total series inductance, R_s is the series resistance and L_p the primary inductance. C_s is the reflected secondary capacitance (= $n^2 C_3$ + stray effects in the secondary windings) and R_L the effective reflected load resistance (= load resistance/n^2 + stray effect of monitors etc). n is the transformer turns ratio.

The first peak in the output of the transformer, when SG_2



Equivalent circuit of the pulsed power supply

Figure 10

was set to break down, occurs at a time t_r given approximately by

$$t_r = \pi \sqrt{\frac{L_s C_2 C_s}{C_2 + C_s}} \qquad (2.2)$$

neglecting damping, and the peak voltage reached, V_p, is given by (defining a gain G)

$$G = \frac{V_p}{V_{C_2(0)}} = n\left[\frac{\exp(-\beta t) + \exp(-\alpha t)}{R_C + R_L + 1}\right] \qquad (2.3)$$

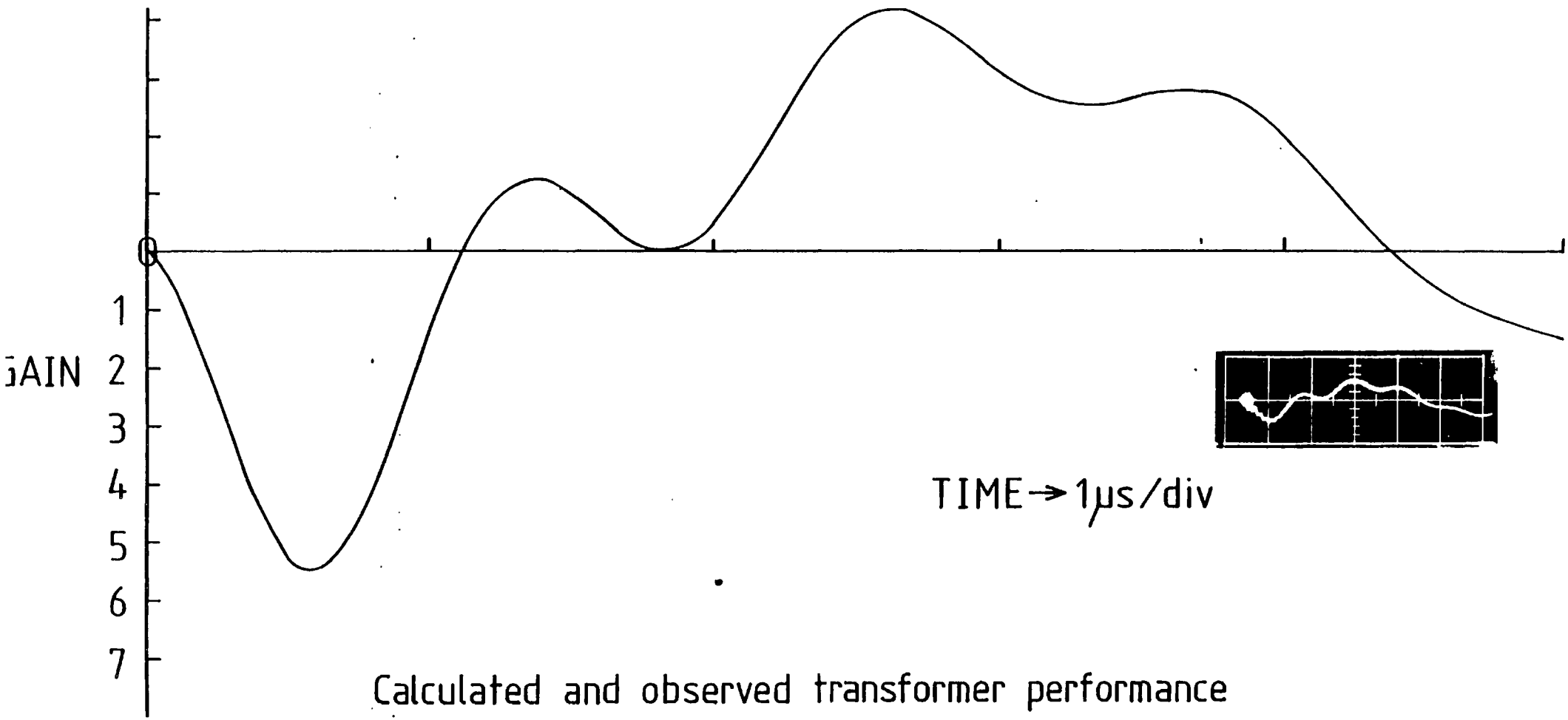
where $R_C = C_s / C_2$ and $R_L = L_s / L_p$.

The values of L_s, L_p, C_s, R_s and R_L depended both on the construction details of the transformer as well as on the external circuit to which it was connected. For example, L_s, the series inductance, was given by the sum

$$L_s = L_{cap} + L_{gap} + L_{feeds} + L_{leak} \qquad (2.4)$$

where L_{cap} was the equivalent series inductance of the capacitor, L_{gap} the inductance of the spark gap, L_{feeds} that of the connections in the primary circuit and L_{leak} the leakage inductance of the transformer. These parameters, either calculated or estimated, were substituted in equations 2.1 - 2.3 in order to model the behaviour of the transformer under certain load conditions.

First, the gain of the transformer under load was checked by observing (see 2.6.1 for monitor details) and calculating (on a small computer with a graphical print-out) the output voltage of the transformer when the power supply was loaded with a 60 Ω copper sulphate resistor. When C_2 was charged to 46 kV, V_p was measured to be 223 kV, i.e. an observed gain of



Calculated and observed transformer performance

Figure 11

4.84. The calculated gain was 4.7 and the time to the first peak was measured and calculated to be 570 ns.

As a second test, the transformer was allowed to ring into the unswitched capacitor C_3. Figure 11 shows the good agreement found between the theoretical and experimental gain measurements.

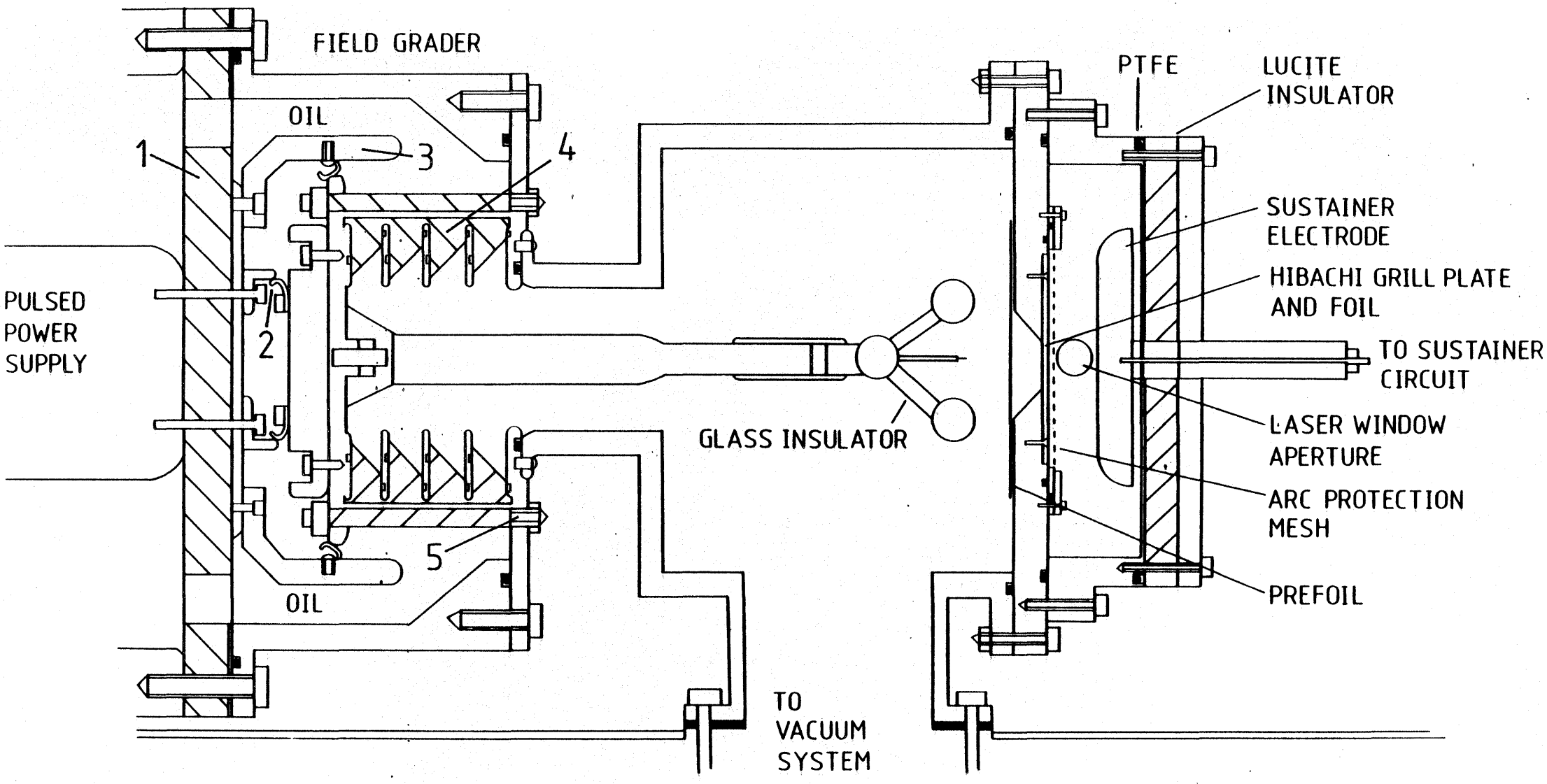
This simple method of circuit analysis, perfected with use over a number of systems, has greatly aided both their design and understanding. Similarly, it would enable the design of further pulsed power supplies to be made with a high degree of confidence.

2.4 The electron beam diode

2.4.1 Output bushing design

In general, to connect the high voltage output of an oil filled pulsed power supply to the cathode of an evacuated electron beam diode a high voltage bushing is necessary. The design of such bushings is well understood[53], and the bushing to be described was originally developed for operation at much higher voltages[49].

Figure 12 shows the cross-section of the bushing and its connection to the transverse electron beam diode. The output plate from the power supply was mounted centrally on to a thick circular perspex plate (1) which was bolted on to the front of the power supply tank. Electrical connection to the cathode stalk plate was made with a push-fit connector (2). A similar technique was used to connect the outside of the cathode stalk plate to an aluminium dish-shaped part (3) which surrounded part of the insulation section of the bushing (4). This insulation section was comprised of a series of perspex rings



E-beam sustained discharge head

Figure 12

chamfered at 45° between which were inserted aluminium rings fitted with 'O' rings. The whole structure was then clamped with six nylon tie bars (5) which compressed the 'O' rings, giving a good vacuum seal. The chamfering of the perspex rings optimised the breakdown strength of their surfaces[53] and the aluminium spacing rings ensured a uniform electric field across the sloping faces of the rings and shielded each section from the effects of its neighbour.

The completed bushing had been carefully designed for use at diode voltages approaching 1 MV and was therefore ideal for the much lower voltages (< 250 kV) of this system.

2.4.2 Theory of electron beam diodes

The purpose of an electron beam diode is to generate an electron beam and to couple that beam into the laser medium as efficiently as possible. Efficiency of generation and coupling is important in ensuring reasonable cathode emitter and anode foil lifetimes.

Figure 12 shows the pumping scheme for the laser under consideration. This was a standard edge-plane diode with an additional focussing capability. In the simplest systems the cathode consists of a long rod or cylinder into which a blade of thin foil is set (typically tantalum, titanium or stainless steel). The cathode is connected to the pulsed power supply by the cathode stalk.

When a negative high voltage pulse is applied to a cold cathode several different phases of operation of the emitter have been identified[54]. Stable field emission first occurs from microscopic whisker-like projections along the cathode due to initial field enhancement (several MV cm^{-1}). Local current densities of up to 10^9A cm^{-2} may flow from these pro-

jections which quickly heat (ohmically) and explode. The plasmas from adjacent exploding microtips begin to overlap and form a cathode sheath along the length of the blade. Space-charge-limited emission of electrons then occurs from the plasma sheath, which behaves as a surface with a zero work function. This stage is reached in a few nanoseconds and is the working regime for any emitter. The exploding plasma also moves towards the anode, at 2-3 cm μs^{-1}, and as it reaches the anode there is a transition to highly convergent electron flow, known as diode closure, as the diode impedance collapses. Self-focussing of the beam by its associated magnetic field is important at very high current densities but could be ignored for this system.

The diode impedance is time-varying and difficult to calculate accurately. Some approximate formulae have, however, been developed for the steady state conditions of space-charge-limited current flow. For example, the space-charge-limited current density for a plane-plane diode geometry is given by Langmuir and Compton[55] as

$$J = \frac{2{\cdot}33\, V^{3/2}}{s^2} \qquad (2.5)$$

where V is the voltage in MV and s the anode-cathode spacing in cm. In Forster's more relevant treatment of an edge-plane diode[56] of length l (where $l >> s$ and $s >> r$, the radius of curvature of the emitting plasma) the diode impedance is found to be

$$Z = \frac{172\, s}{l\, V^{1/2}} \qquad (2.6)$$

Only the empirical treatment of Martin[57] has attempted to include the effect of the blade support plane or cylinder on the diode impedance.

The lack of development of these studies and the complexity of the diode under consideration meant that the optimisation of the electron beam was largely empirical, although the equations above did allow first estimates of impedances to be made (for the calculations of 2.3).

2.4.3 Diode construction

A blade length of 40 cm and an electron beam window height of 2 cm were originally chosen[49] on the basis of existing reports of successfully operating e-beam sustained XeCl lasers[46], [47]. The transmitted 2 x 40 cm^2 beam was then a balance between a short (25 cm) wide beam system and a long (100 cm) narrow beam system.

Care was taken so that the separation between the cathode components and the earthed outside case of figure 12 was sufficient to prevent vacuum breakdown. Field enhancement due to sharp edges was minimised by using polished, thick, rounded cathode components. All of these dural cathode components were coated with a thin film of diffusion pump oil applied from a solution of the oil in acetone to minimise the chance of field emission occurring from them.

The generated electron beam traversed two foils and a wire mesh before entering the laser cavity. The first of these, a thin prefoil, also defined the e-beam anode plane while the second, mounted on a "Hibachi" grill structure, provided a thin but strong barrier between the high vacuum ($< 10^{-5}$ torr) of the diode and the pressurised laser chamber. Finally, the mesh acted as the discharge cathode, at earth with respect to the e-beam cathode (2.6.2 for more details).

The vacuum system was mounted underneath the welded steel table on which the power supply was positioned. Two

systems were employed, one to pump the diode chamber and one the laser cavity. Both consisted of a conventional rotary pump/diffusion pump combination with appropriate liquid nitrogen traps. Automatic electric valves allowed the convenient operation of both systems.

2.5 Diode Performance

The performance of the diode was dependent on a number of important factors: (i) the cathode material, (ii) the focussing arrangement, (iii) the anode-cathode spacing, (iv) the foils and mesh. The effects of changes in (i)-(iv) were monitored by measuring (a) the diode voltage, (b) the total emitted electron beam current, (c) the electron beam current transmitted into the laser cavity, (d) the electron beam spatial profile and (e) the reliability and reproducibility of the results.

2.5.1 Techniques of measurement

(a) the diode voltage - the voltage reaching the cathode was monitored from inside the power supply with a copper sulphate resistive divider[58]. Essentially this consisted of two copper sulphate resistors in series, with an overall resistance $\simeq 10\ k\Omega$. One resistor was in the form of a long P.V.C. tube filled with copper sulphate solution (resistance $\simeq 10\ k\Omega$) and was connected to a low resistance ($\simeq 5\Omega$) copper sulphate resistor which was formed between two circular copper plates. The voltage across this resistor was monitored via a coaxial U.H.F.-type connector. Such dividers have an excellent high frequency response and a high noise immunity.

(b) the total emitted e-beam current - this was the sum

of the current collected by the e-beam anode and that transmitted through the anode window into the laser cavity (c). The anode collected current was measured by isolating the anode plate and passing the collected current to earth through 48 x 2.2Ω non-inductive resistors, arranged around the plate at equal spacing. The potential difference then generated across the monitor was assumed proportional to the current collected.

(c) the transmitted e-beam current - the plate inside the laser cavity, which was to become the discharge anode, was originally used to collect this current. In this case the collected current was returned to earth through 24, 2.2Ω symmetrically placed non-inductive resistors. However, blue cellophane dye dosimetry measurements (d) indicated that an appreciable fraction of the electrons reaching the plate were being re-emitted as secondaries and lowering the measured current (this was a field-free region). To account for this a form of Faraday cup was built around the plate with a 40 x 0.5 cm^2 aperture lying close to the foil window. In this way a more accurate estimation of the transmitted beam current was made.

(d) the e-beam spatial profile - the spatial variation of current density, i.e. the beam uniformity and width, was found by "Avisco" blue cellophane dye dosimetry[59]. Bleaching of thin cellophane by the e-beam, which was logarithmically proportional to the number of electrons which had passed through, was scanned on a "Joyce-Loebl" recording microdensitometer to give the beam profiles. To prevent saturation of the dye, strips of aluminium foil were introduced to reduce the e-beam dose received by the cellophane to an acceptable level from a single shot.

(e) reliability and reproducibility - these factors were borne continually in mind throughout experimentation. It was very important, for the laser to be successfully used in later work, that the results of (a)-(d) could be repeated often and reliably with only a minimum of maintenance.

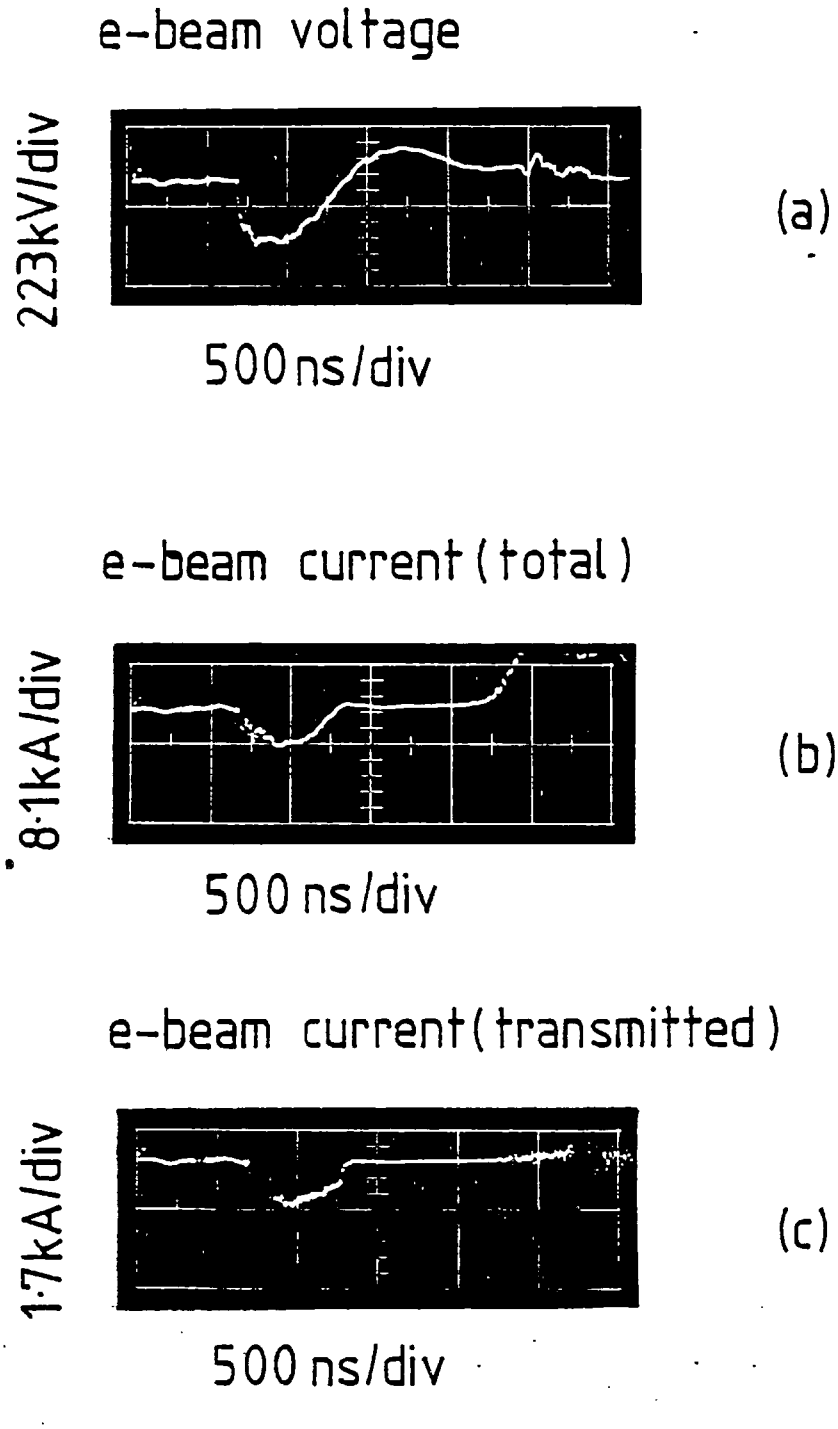
2.5.2 Optimisation of the electron beam

Figures 13 and 14 show a set of results taken for a particular diode configuration. They show the cathode voltage, total and transmitted e-beam currents, and the beam profile at the window.

Each of the parameters (i)-(v) was varied, and the results obtained can be summarised as follows :

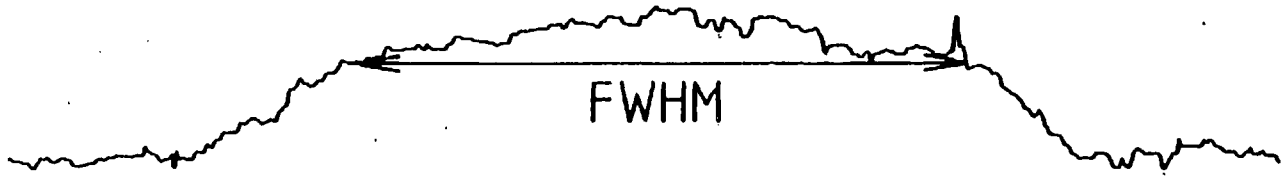
(i) the cathode material - a number of different cathode materials were studied in a particular diode arrangement to look for the best emitter. A simple, single, uncoated stainless steel blade proved the most successful. No improvement was found with titanium or tantalum foils, or multiple stainless steel arrangements. Similarly, despite some evidence to the contrary[60], a carbon cathode, in the form of graphite felt, gave no better results.

(ii) and (iii) the focussing arrangement and anode to cathode spacing - two focussing arrangements were considered. In the first, the cathode consisted of a cylindrical blade holder of 2.54 cm diameter with the blade centrally positioned, around which was mounted a "race-track" type structure. This was constructed from 2.54 cm diameter dural tube and was electrically connected to the cathode. In the second, capacitive electrostatic focussing arrangement[61], two 2.54 cm diameter focussing electrodes were mounted above and below, and parallel to, the blade holder on glass rod insulators (see

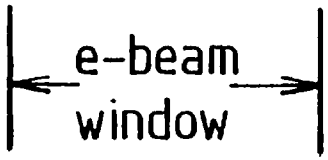


Synchronised electrical characteristics of the electron beam

Figure 13



(a) at the prefoil





(b)at the discharge

Transverse e-beam current density profiles

Figure 14

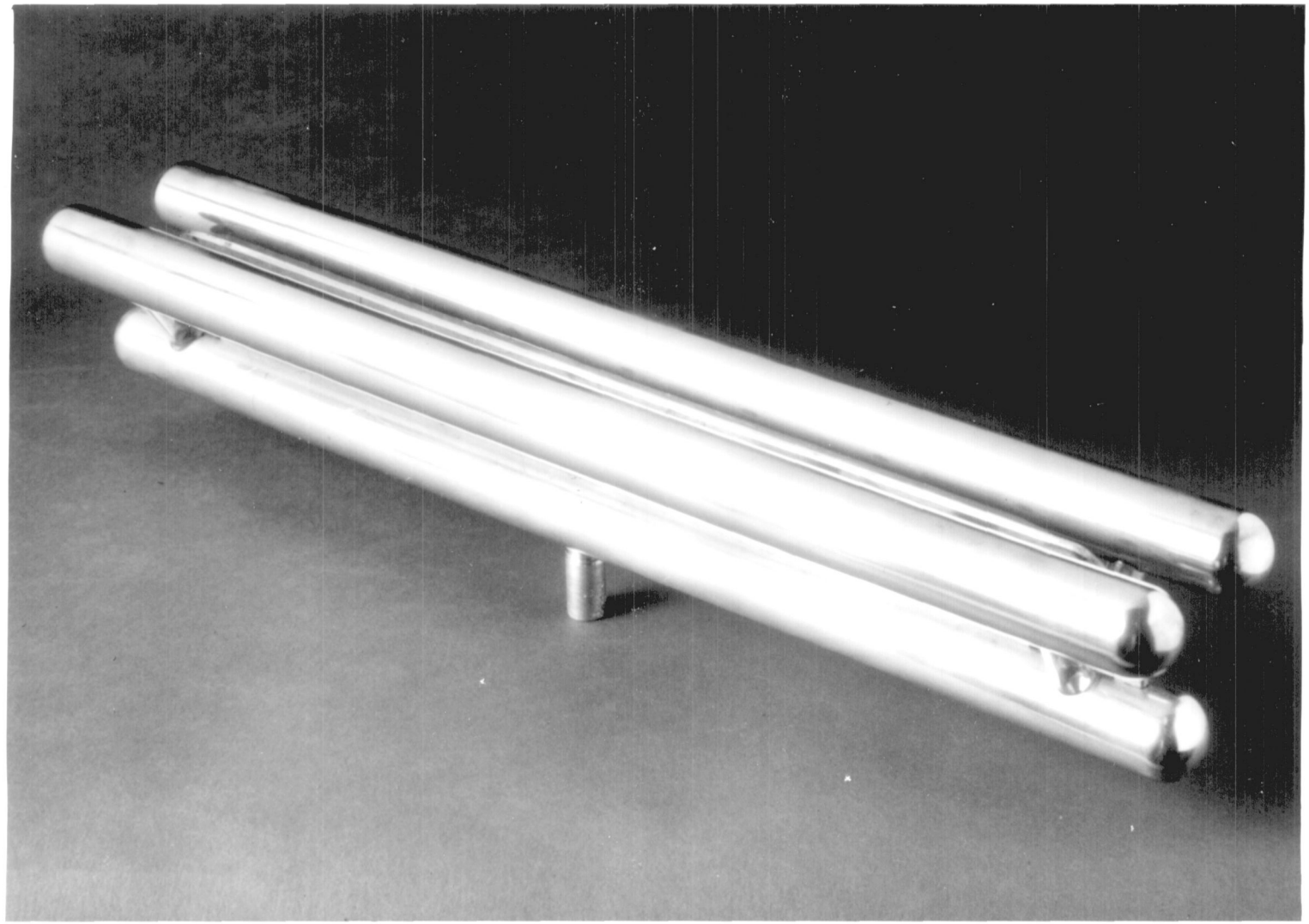


Figure 15 (plate) The focussing electrodes

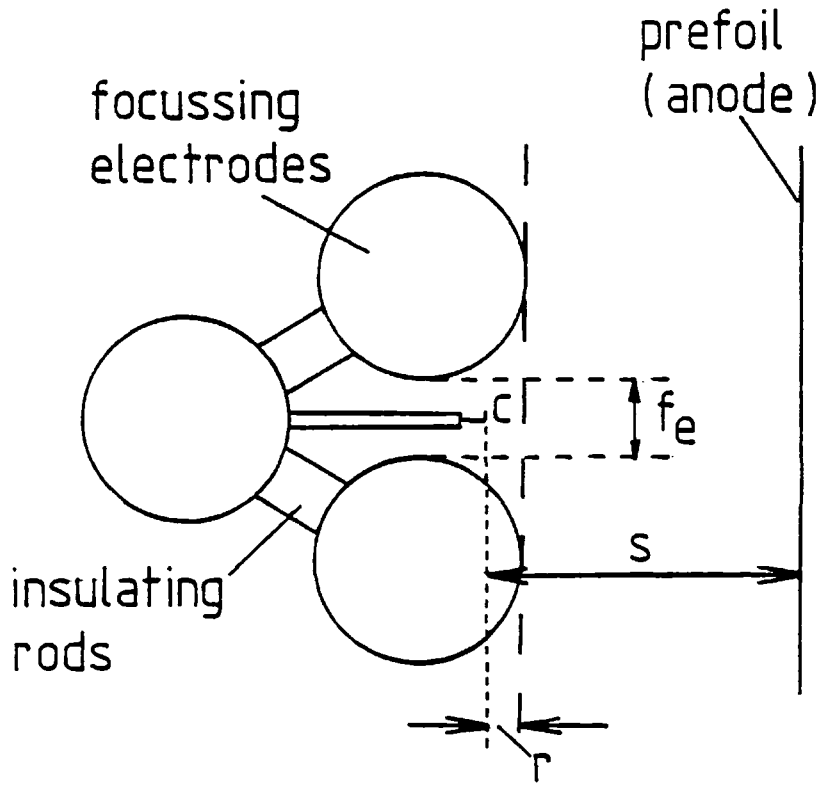
figure 12 and the plate of figure 15). When the negative voltage was first applied to this assembly, the cold cathode emitter behaved as though it was unfocussed and the normal blade emission process was not inhibited. Once the blade started to emit electrons, the focussing electrodes charged up to the cathode potential and the resultant electrostatic field restricted the divergence of the beam as it travelled towards the anode.

The construction of the two cathodes was such that, in the first case, the recess of the blade behind the plane of the focussing electrodes was the only variable, while in the second the actual focussing electrode separation could be changed. In both cases, of course, the anode-cathode spacing could be changed. The impedance of either diode was seen to be mainly dependent on the blade-anode separation.

Although the two types of focussing were difficult to compare directly, experiments indicated that for similar diode impedances a 50% improvement could reliably be achieved in reducing the beam diameter at the anode with the capacitive system. Further work was therefore concentrated on this.

Figure 16 shows the important dimensions of the capacitive focussing system which were varied. In order to generate a high cathode voltage, necessary to allow a reasonable percentage of the electron beam to be transmitted through the foils, the value of the diode impedance and hence s was kept as high as possible. The distance of the cathode stalk to the surrounding structure, however, limited this to $s < 4$ cm, otherwise arcing was found to occur from the stalk. A second limitation was on f_e, the focussing electrode separation. Greater focussing levels could be achieved by reducing this and

Figure 16



c: blade cathode

Variable dimensions of the capacitive focussing system

Table 3

Arrangement	s/cm	r/cm	fe/mm	beam height at prefoil/cm
1	3.5	0.0	8	5.2
2	4.0	0.5	8	3.2
3	3.8	0.3	8	4.0

Diode optimisation results (see figure 16)

increasing the recess of the blade, but eventually a point was reached where the blade was shielded to such an extent that breakdown occurred from the focussing electrodes to the anode foil preferentially to cold cathode electron emission from the blade.

A focussing electrode separation f_e of 8 mm was found to give reliable focussing - for larger values the beam divergence was too great, while for smaller values the diode was unstable. Having decided on a value of f_e, and approximately on s, the blade recess r could then be varied to examine the effect of this on the beam height at the "Hibachi" window. A typical set of results is summarised in table 3. The beam heights given should be compared to a height of 7 cm for an unfocussed beam at a similar diode impedance.

The initial design criteria would lead to arrangement 2 being chosen as the optimum. This, however, would not take into account problems of reliability. It was found that arrangement 3 was the highest focussed position which allowed almost unlimited operation with a minimum of maintenance, and this became the standard set-up in later work.

(iv) the foils and mesh - the e-beam passed into the laser cavity through two foils and a wire mesh. A thin (12.5 μm) aluminium prefoil was taped on to the anode plate to stop low energy electrons produced by the tail of the voltage pulse from the power supply. It was found that, if the prefoil was not used, the energy due to these electrons was deposited in the main pressure bearing foil and led to its early failure. The prefoil also allowed the anode plate to present a uniformly flat surface to the cathode, thereby ensuring a more uniform field in the diode by covering the window recess in the anode plate (figure 12). Finally, any vacuum breakdown or diode

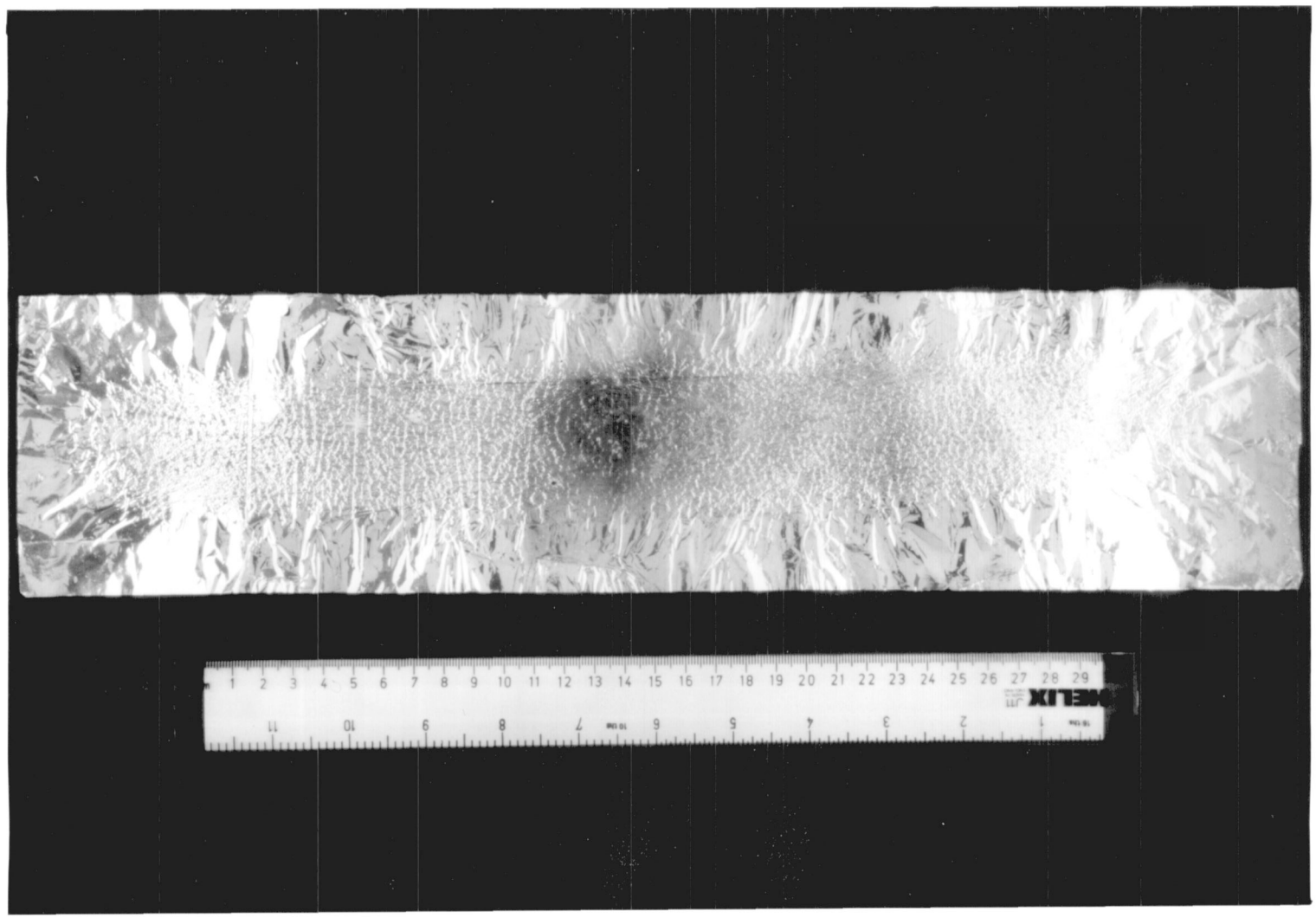


Figure 17 (plate) A prefoil

closure occurred to the prefoil, often damaging it, but again protecting the main foil. Figure 17 shows the effects of upwards of one hundred e-beam shots on a prefoil.

A preferable alternative to the prefoil, which also attenuated the useful fast electrons, would have been to have installed a "crowbar" beyond the SF_6 spark gap SG_2 of figure 7. This would have been a triggerable spark gap, fired as the cathode voltage fell below a certain level and dumping the remaining energy of the power supply to earth through a resistor, hence preventing the production of low energy electrons at the cathode. The spark gap would be pressurised such that it did not self-break at the peak of the transformer output (> 200 kV). However, in this case, the necessary voltage pulse which would have then been required to trigger the gap was not available.

The pressure bearing main foil (3.2.1), supported on a 2 x 38 cm^2 "Hibachi" grill structure, consisted of either 75 μm P.T.F.E. coated "Kapton" polymide film or 30 μm titanium. Figure 18 is a plate of the foil and "Hibachi" from the discharge anode side, showing the grill through the semi-transparent "Kapton".

The titanium foil was found to have a higher tensile strength than the Kapton, although when it failed the foil collapsed totally and often caused damage to the e-beam diode assembly. Kapton failed gradually, as it developed pin-hole-type fractures, and had the advantage over titanium of a slightly higher electron transmissivity.

Finally, the electron beam passed through a stainless steel mesh of 80% transmission which acted as the discharge cathode. A mesh with higher transmission did not give the main foil adequate protection from discharge arcs.

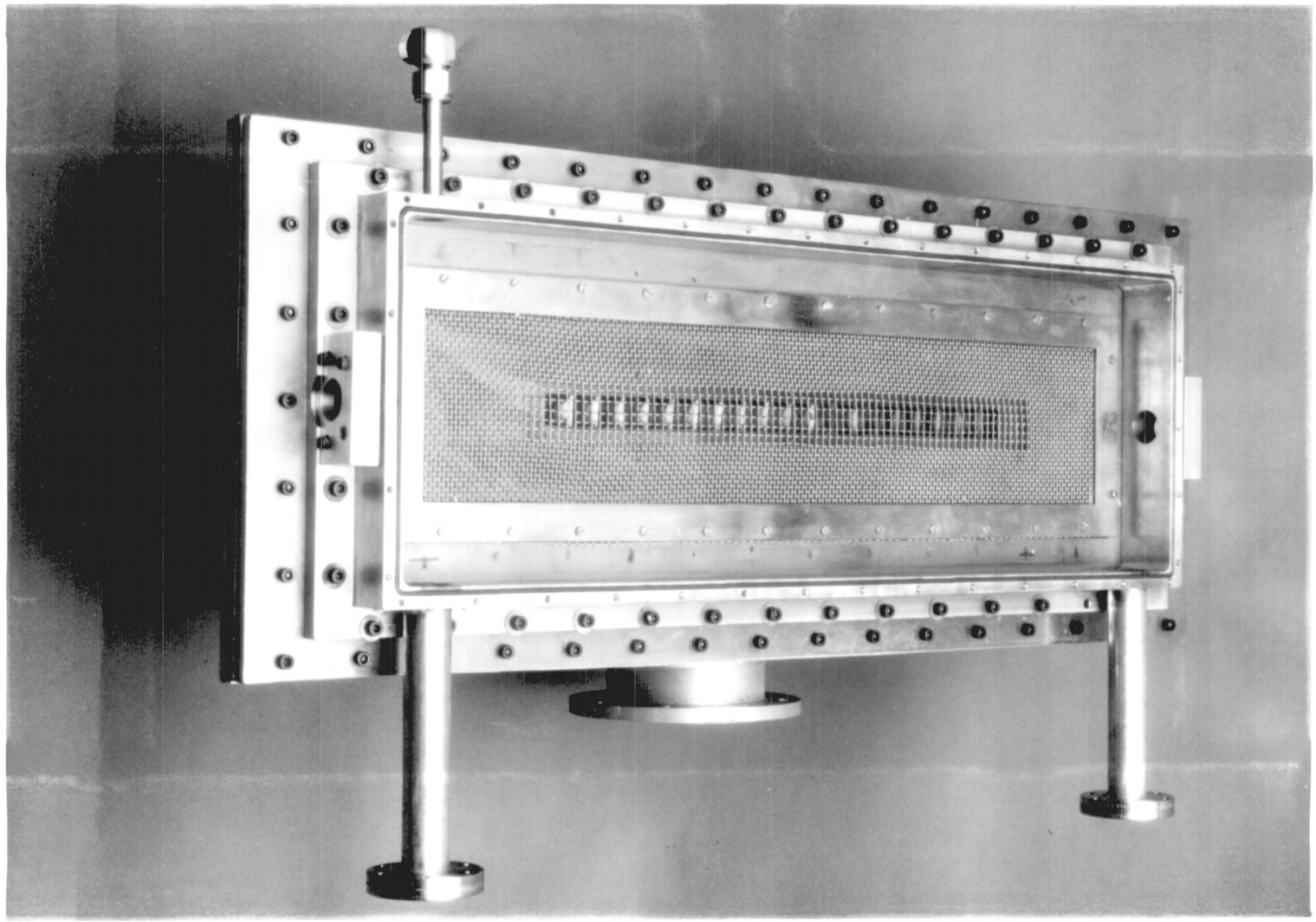


Figure 18 (plate) The discharge cavity

2.5.3 Experimental problems

A protracted amount of time was spent studying the operation of the diode. A typical operation might involve opening the diode or discharge chamber and changing a foil or the position of the cathode. The system would then be pumped down and fired. In the case of dye dosimetry, after one shot the system would again be opened to extract the cellophane and prepare another experiment. This process would take upwards of three hours and therefore the rate of acquisition of data was slow.

When optimisation was complete the arrangement chosen allowed a minimum of maintenance. After several hundred shots it was important to change the cathode blade and to repolish and oil the focussing electrodes. Regularly replacing the blade and polishing the electrodes allowed continued uniform electron beam operation and ensured that parasitic breakdown from the electrodes was kept to a minimum, while replacing the prefoil protected the main foil from damage as the prefoil deteriorated. Replacing the main foil, which needed to form a vacuum seal, was more time-consuming; it involved entering both the discharge and diode cavities and made repassivation unavoidable.

2.6 Standard operating characteristics

With accurate positioning of the cathode (to ± 0.5 mm) and regular maintenance, the electron beam generator could be fired for an indefinite number of shots without replacing the main foil.

The performance in this arrangement, which was the standard set-up for all later work, can now be reviewed (table 4). C_2 was charged to 46 kV, SG_1 pressurised to 22 psi

Table 4

Output voltage (peak into 44Ω load)	189 kV
Pulse duration (FWHM)	450 ns
Rise time	100 ns
Throughput delay	300 ns
Output current (peak into 44Ω load)	4.1 kA
Beam height at the prefoil	4 cm (x 40cm long)
Window size	2 x 40 cm^2
Mean (spatial) current density over the window area at the prefoil	30 Acm^{-2}
Mean (spatial) current density entering the discharge volume	13 Acm^{-2}

Pulsed power supply and diode performance summary

above atmospheric with dry air, and SG_2 to 20 psi above atmospheric with SF_6. Figure 13 shows the voltage and current characteristics of the diode. The peak voltage reached was 189 kV and the peak total e-beam current was 4.1 kA. The current density was uniform to within ± 10% along the length of the Hibachi window, while its cross section across the window is shown in figure 14. The mean current density at the prefoil was calculated to be 26 A cm^{-2} and cellophane dye dosimetry indicated that at the central portion of the foil overlapping the window it was approximately 30 A cm^{-2}. 13 A cm^{-2} of current density was measured to be reaching the discharge cavity.

Figure 13(b) clearly shows the sudden rise in electron beam current as diode closure occurred (at this stage the diode voltage had swung positive). The average speed of diode closure was therefore $\simeq 2.2$ cm μs^{-1}.

A Tektronix 519 oscilloscope with suitable attenuators gave the traces of figure 13. All results should be accurate to better than 10%.

CHAPTER 3

THE ELECTRON BEAM SUSTAINED DISCHARGE LASER

3.1 Introduction

Chapter 2 discussed the development of an electron beam generator. This chapter will go on to consider the design and performance of the discharge sustained by this electron beam, and the resultant laser operation. Results will be given for both XeCl and KrF lasers, together with the outcome of efficiency, gain and unstable resonator experiments.

3.2 The laser cavity

3.2.1 Design and optics

Figure 19 is a plate of the diode chamber and discharge cavity showing the two vacuum connections on the bottom, gas infill connection on the top, and the three discharge anode feeds entering the chamber from the left.

All metallic components of the laser cavity were stainless steel, and the insulating components P.T.F.E. The cell was sealed with 'O' rings made from Viton and lubricated with fluorinated vacuum grease. These precautions were made necessary by the extremely corrosive nature of the laser gas mixtures. The pressure bearing foil was sealed by a single 'O' ring in a metal compression plate and the mesh set in front of it with a second plate. The second discharge electrode was held on three electrical feeds which passed through the rear wall of the cavity. Three spacing rings behind this electrode set the anode-cathode spacing to 3 cm. The output energy of the laser was found to be strongly dependent on the polarity of this discharge electrode. Higher energies were obtained with it connected as an anode,

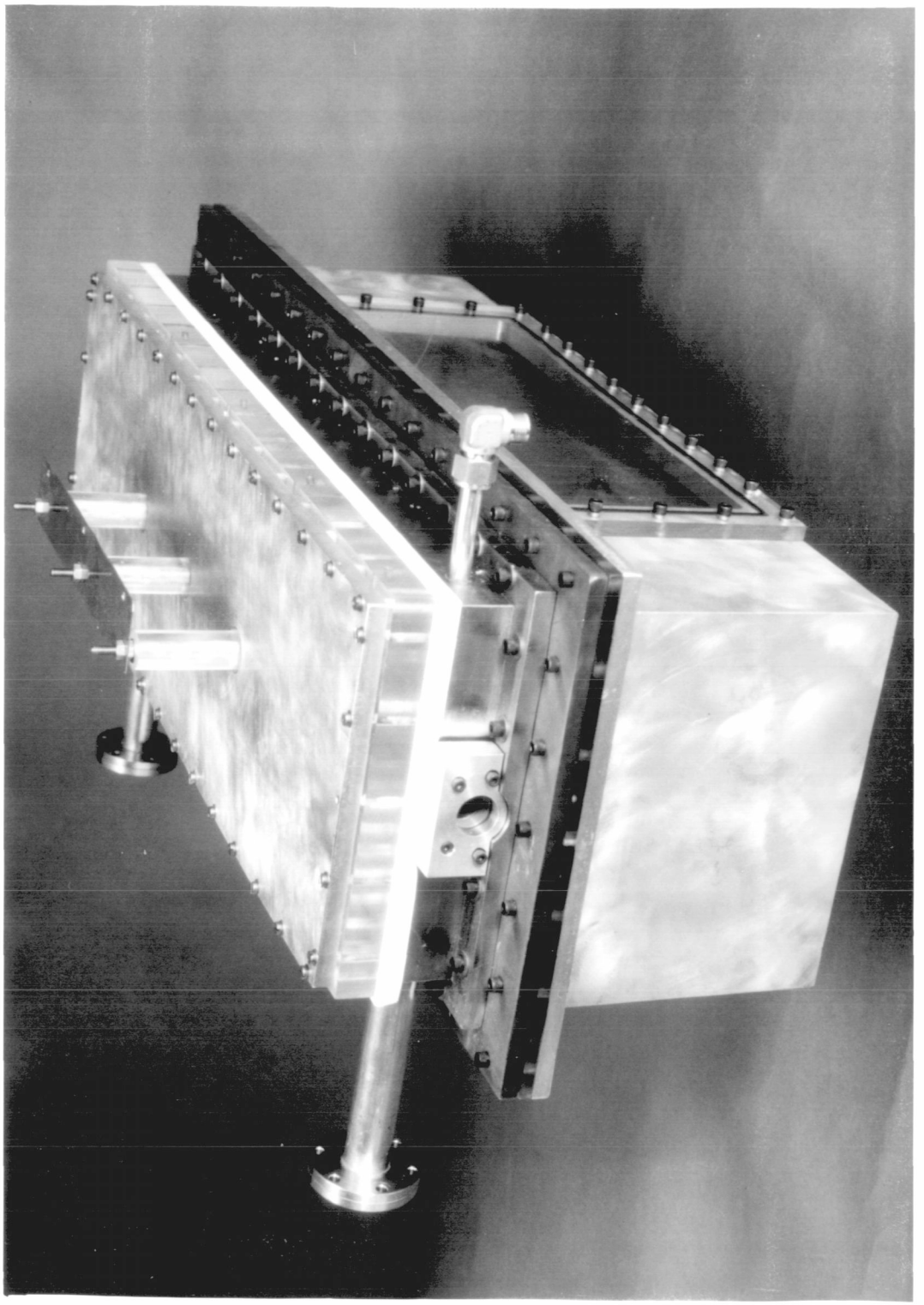


Figure 19 (plate) Diode and discharge chambers

encouraging the flow into the gas of e-beam electrons.

Two end window arrangements were employed. In the first (figure 19), they were mounted on the outside of the discharge chamber and set on two 'O' rings. This allowed them to be aligned parallel to the laser mirrors. Two 2.5 cm diameter polished Spectrosil 'A' quartz or sapphire windows were used. Sapphire windows were less prone to attack from fluorine, but more difficult to polish. Alternatively, when a well defined cavity length was necessary, 7.62 cm diameter Spectrosil 'A' windows could be fitted at Brewster's angle.

Before any experiments were begun with a particular laser gas mixture, the cavity was passivated overnight with $\simeq 50$ torr of the appropriate halogen donor (and with the windows replaced by metal blanks). This was usually sufficient to ensure a reasonable level of passivation and prevent further reactions between the gases and the cavity components taking place. However, it was found that if the system was passivated with HCl for the XeCl laser, it took much longer to then passivate the system with F_2 when converting to KrF. This was probably because a slow exchange reaction occurred between chlorine, in the metallic chlorides of the passivated layer, and fluorine, since fluorine is the more electronegative.

A plane multilayer dielectric mirror of >97% reflectivity and 5 cm diameter formed one end of the laser cavity for both the XeCl and KrF lasers. Either a second multilayer dielectric (60-70% reflectivity for XeCl, slightly more for KrF - 70%) or a three-plate-resonant-reflector was used for output coupling. All mirrors were held in 5 cm kinematic mounts which were either bolted to the ends of the cavity or put on separate optical benches.

3.2.2 Gas handling

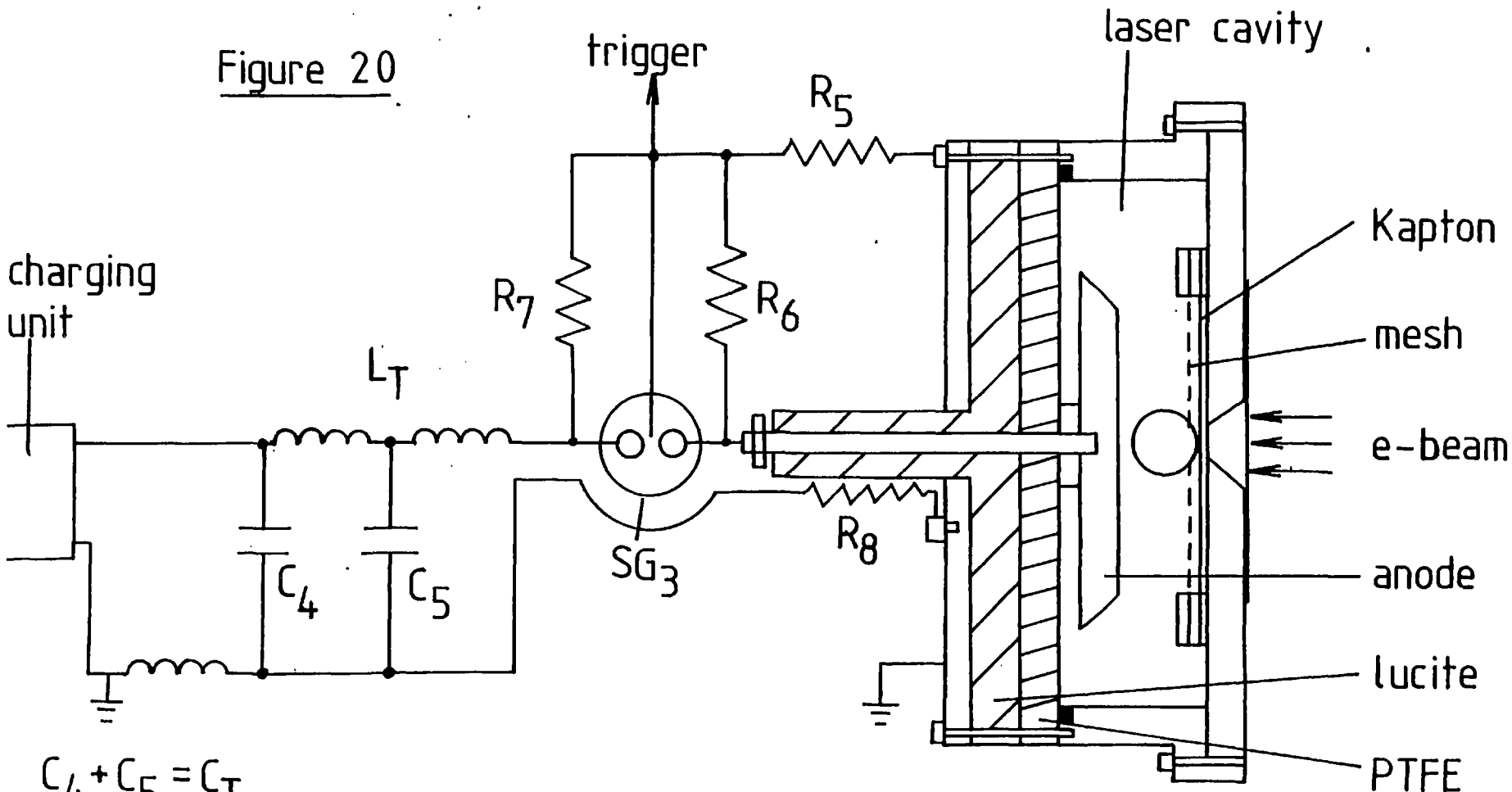
All taps, gauges and tubing were made of stainless steel. The taps were of the bellows variety and the tubing ½" o.d. After evacuation to < 10^{-4} torr the laser cavity was first filled with the halogen bearing gas, the pressure being monitored on an electronic "Capsulon" gauge. The rare gas component of the mix was then added, the pressure being read from a capsule gauge. Finally, the buffer gas was added, and monitored by two "Budenberg" gauges. Gas mixtures were left for about 15 minutes prior to firing to ensure adequate mixing.

At the end of an experimental run the mixture was exhausted through a trap containing concentrated potassium hydroxide solution to absorb the halogen. For very corrosive mixtures the cavity was filled and exhausted with buffer gas several more times before evacuation. This minimised chemical degradation of the pump oils by halogenation.

3.3 Discharge design and operation

Figure 20 shows the connection of the laser cavity electrodes to the external discharge circuit. A Hartley Measurements Ltd. 600 Js^{-1} 50 kV unit charged the main energy storage capacitors C_4, C_5 (total C_T 0.25-0.55 μF) to up to 30 kV. Energy from C_T was then discharged into the laser cavity via spark gap SG_3. This was a low inductance rail gap, of similar design to SG_1, with main electrodes 27 cm long and 0.5 cm apart and pressurised with dry air. It was triggered automatically from the potential divider R_2, R_3 mounted in the pulsed power supply (figure 7). D.C. biasing of the trigger electrode was set with the resistive network R_5, R_6, R_7. A small value resistor R_8, constructed from "Nichrome" foil, provided a means of monitoring the discharge current, by measuring the potential

Figure 20



$C_4 + C_5 = C_T$

$R_6, R_7 = 60\,M\Omega$

$R_5 = 300\,\Omega$

Laser cavity and discharge circuit

developed across it, and a resistive divider allowed the potential being fed to the discharge anode to be measured.

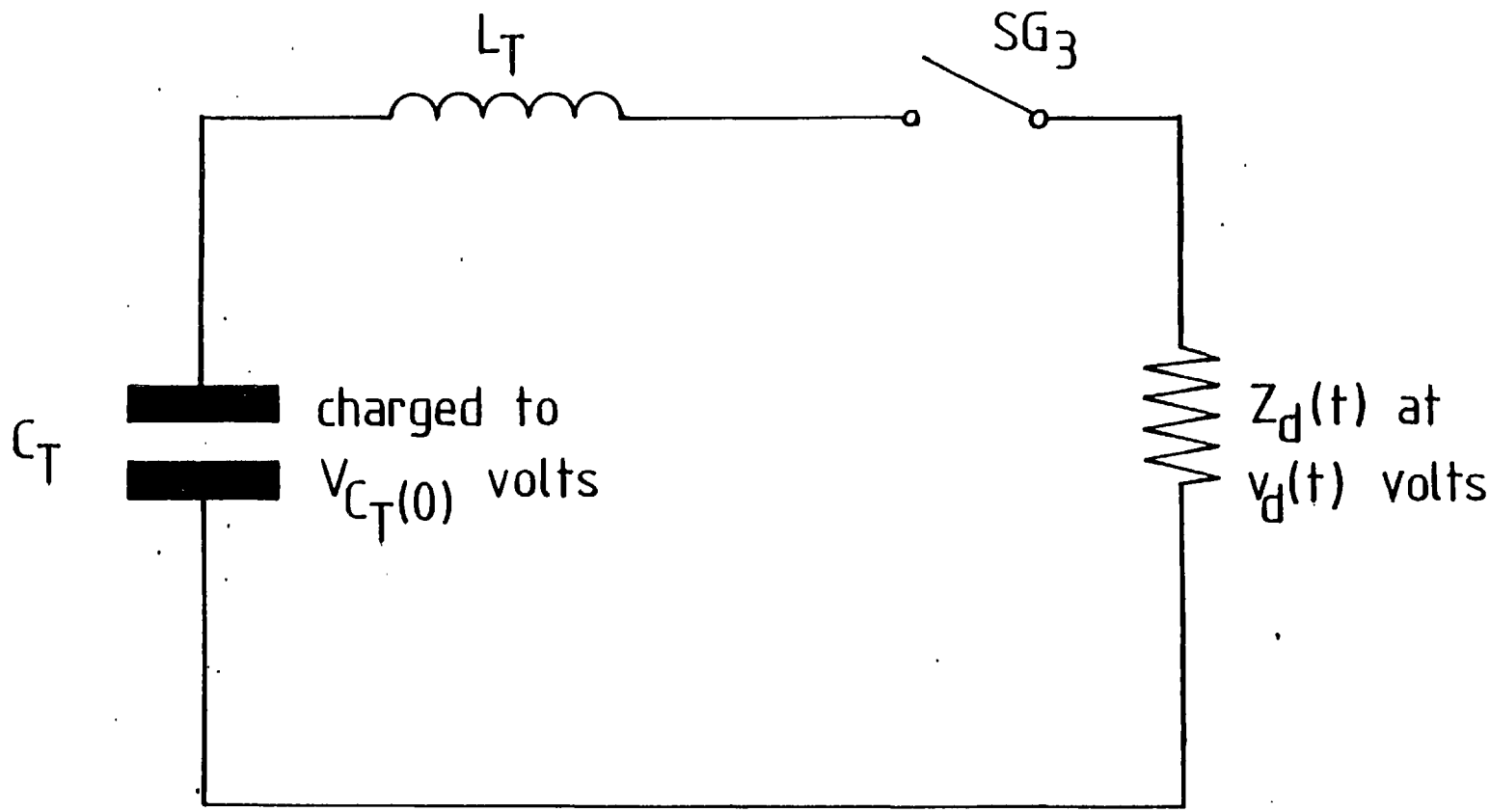
The amount of energy discharged into the cavity was strongly dependent on the overall inductance L_T of the discharge circuit. It was observed, and it has been reported[62], that the discharge impedance in an e-beam sustained excimer laser system falls rapidly to a low but fairly constant value. The particular value is mainly dependent on such factors as the concentration of halogen bearing molecules, gas pressure, e-beam current density and discharge dimensions. If the time varying discharge impedance is denoted by $Z_d(t)$, transient analysis of the discharge circuit of figure 21 leads to an expression for the voltage across the discharge as a function of time of the form (underdamped)

$$v_d(t) \simeq V_{C_T(0)} \frac{Z_d(t)}{\omega L_T} \exp(-\alpha' t) \sin(\omega t) \qquad (3.1)$$

where $V_{C_T(0)}$ is the initial voltage on C_T,

$$\omega = \sqrt{\frac{1}{L_T C_T} - \alpha'^2} \qquad \text{and} \qquad \alpha' = \frac{Z_d(t)}{2 L_T} .$$

The power deposited in the discharge was therefore $v_d(t)^2 / Z_d(t)$. 3.1 implies that the total energy deposited in the gas was maximised by keeping the inductance of the discharge circuit as low as possible. This also served to minimise the discharge voltage risetime. Low inductance parallel plate feeds therefore connected C_T to SG_3 and three feeds were used to connect SG_3 to the anode in the discharge cavity.



Simplified discharge circuit diagram

Figure 21

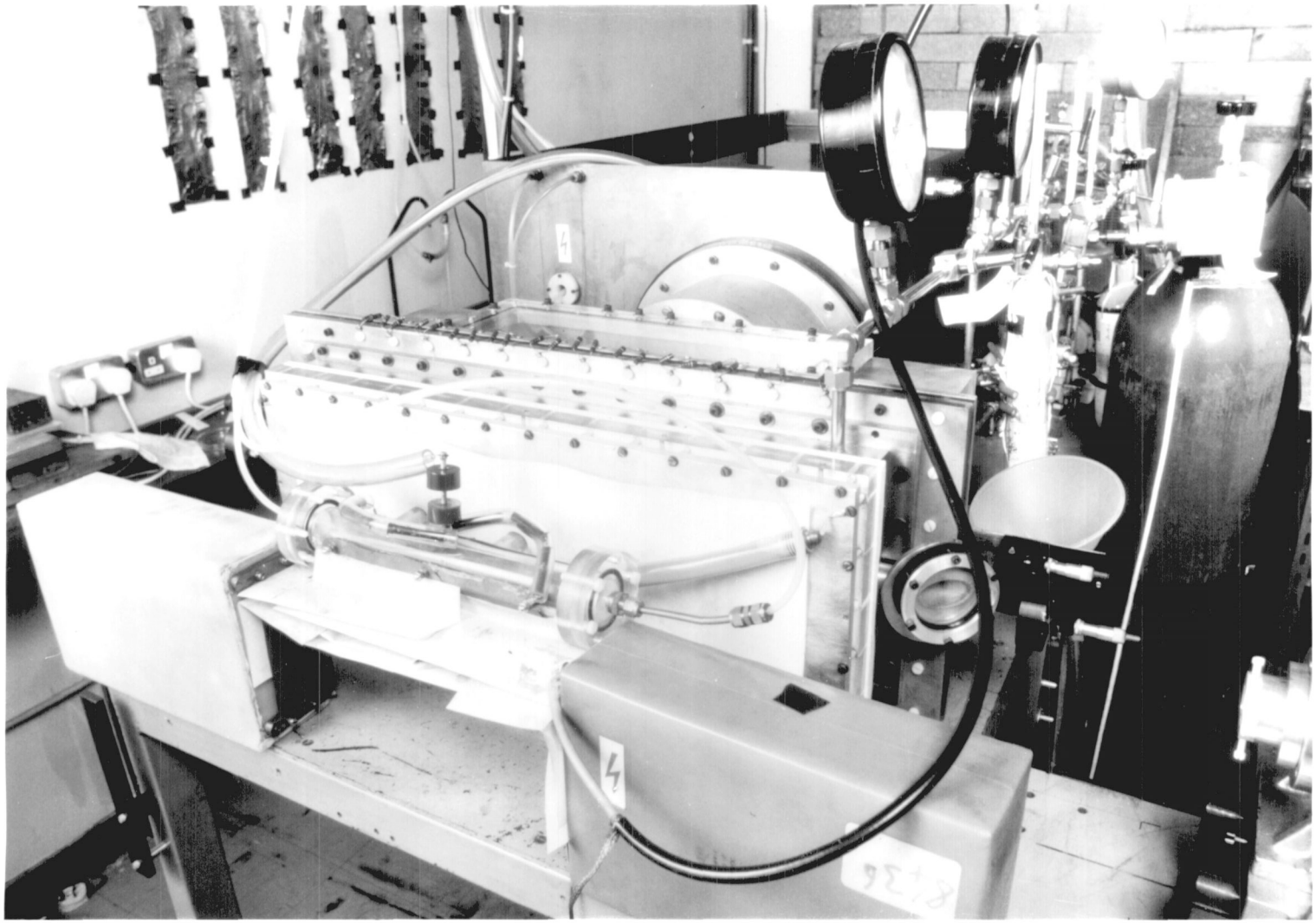


Figure 22 (plate) The complete laser system

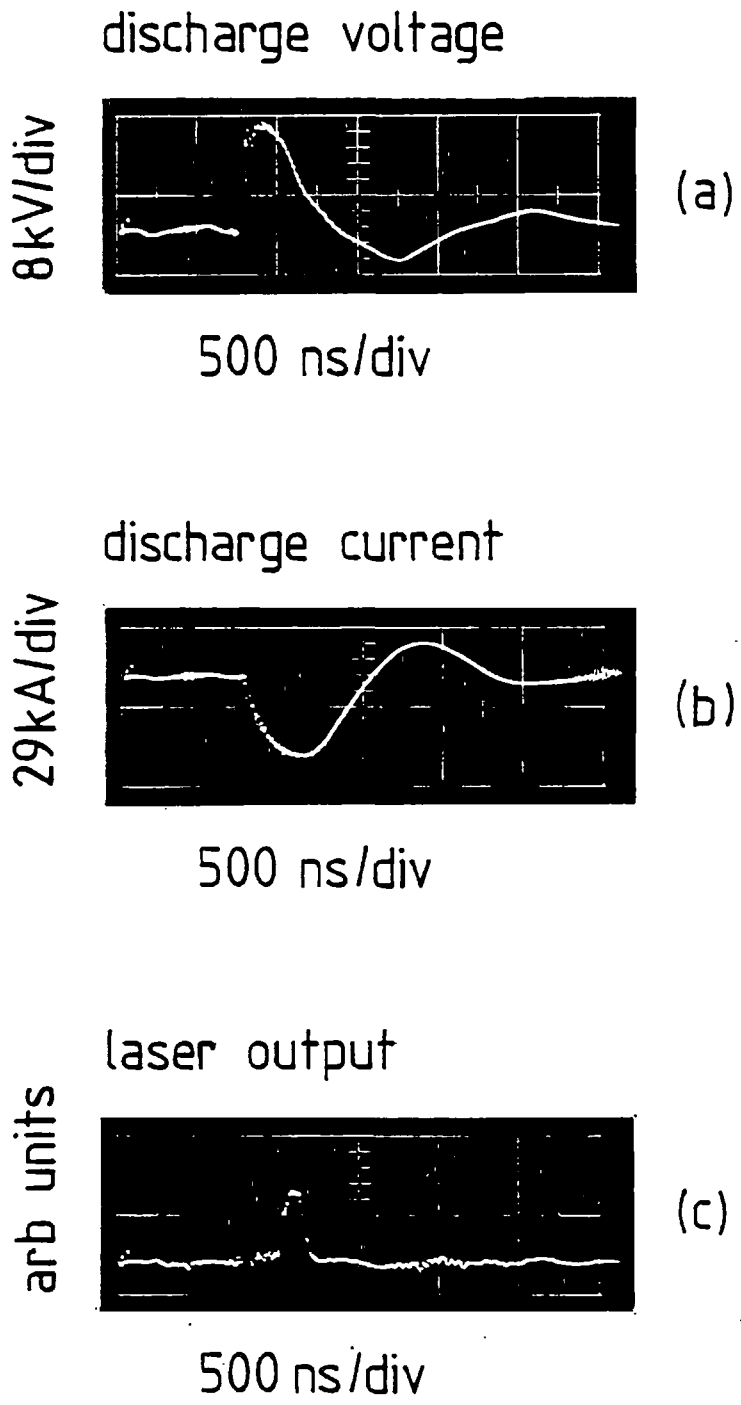
The range of available values of C_T, consisting of two rapid discharge capacitors, was 0.25 - 0.55 μF. Higher values of C_T decreased the discharge voltage risetime and, especially in the upper part of the range, did not appreciably increase the energy deposited. In early work, a single 0.25 μF capacitor was often used since this restricted the amount of energy deposited in the gas and was seen to give longer foil lifetimes. Once the laser had been optimised, however, 0.55 μF was most commonly used.

Figure 22 is a plate of the complete laser system. The plate shows, from background to foreground :- the oil filled pulse power supply, electron beam diode with perspex viewing port, discharge cavity with a single Brewster's angle end window and cavity mirror visible (to the right) and discharge circuit. In this latter, two capacitors lie to either side of the centrally placed spark gap. Also visible, to the right of the plate, is the gas handling apparatus.

Typical synchronised discharge voltage and current waveforms, alongside a laser output pulse, are given in figure 23. The spark gap was pressurised to 15 p.s.i. above atmospheric and C_T, 0.55 μF, charged to 24 kV.

3.4 Performance of the XeCl laser

The results to be reported in the following section were obtained with aligned 2.5 cm diameter end windows and the 60-70% reflectivity multilayer dielectric mirror as the output coupler. An I.T.L. photodiode, in association with a Tektronix 519 oscilloscope, was used to record the time variation of the laser light output, and a Laser Instrumentation Ltd. 142 LR calorimeter was used to measure the laser output energy.



Synchronised electrical characteristics of the discharge and the laser output power

Figure 23

3.4.1 Electron beam pumping

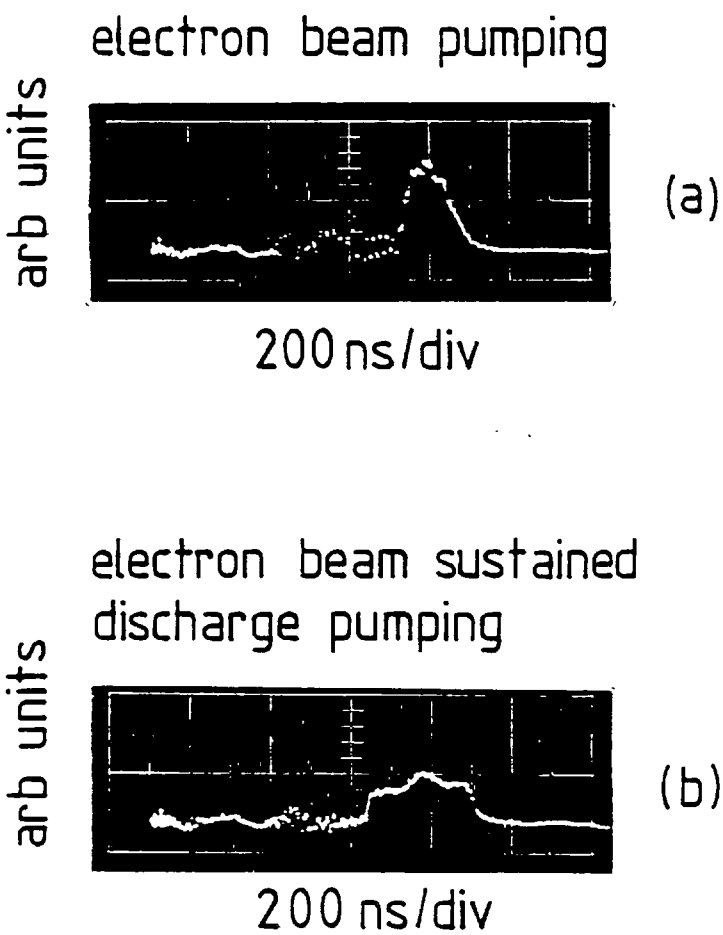
With electron beam pumping alone, a gas optimisation procedure was carried out to discover the gas mixture corresponding to the highest laser output energies. Of the two diluents commonly used in e-beam pumped XeCl lasers, Ar and Ne, Ar was the more successful. A maximum output of 70 mJ in a 140 ns (F.W.H.M.) pulse was recorded (fig. 24(a)) with a gas mixture of HCl:Xe:Ar in the ratio 1:15:1140 at a total pressure of 3 Bar. As an indication of the output variation with gas mix, the output energy fell by $\simeq$30% if the HCl partial pressure was changed by approximately 1 torr, or the Xe partial pressure by 10 torr, or the Ar pressure by 1 Bar.

A measure of the beam profile was made by scanning the small target (0.5 cm) calorimeter across the beam from the mesh side, where the e-beam entered the gas, to the discharge anode. At a total pressure of 3 Bar the output energy was reasonably uniformly distributed around the centre of the aperture, but at 4 Bar most was concentrated in the half of the beam nearest the mesh. Hence, at the lower pressure, the stopping power of the gas was such that the electron beam energy was reasonably uniformly deposited through the gap, but at the higher pressure much more was being deposited near the mesh. These results gave a good guide to the stopping powers which would be optimum for operation in the sustained mode.

3.4.2 Electron beam sustained pumping

A similar procedure was followed for the electron beam sustained discharge pumping of XeCl, with the added complexity of being able to vary the discharge parameters.

With C_T charged to an optimum value of 24 kV, an output pulse energy of 800 mJ was measured in a pulse of 250 ns



Optimised laser output profiles
(a) 70 mJ
(b) 800 mJ

Figure 24

(F.W.H.M.). The optimised gas mix was HCl:Xe:Ne in the ratio 1:17:1260 at a total pressure of 5 Bar. Figure 24 shows the output pulses recorded for both e-beam and e-beam sustained pumping, and figure 23 shows the discharge current and voltage traces corresponding to the latter. The output energy had approximately the same fractional variation with partial pressures of HCl, Xe and Ne as for HCl, Xe and Ar in 3.4.1. Section 3.7 will consider further the characteristics of the laser output and its variation with partial pressures, including a discussion of the use of mixed diluents.

3.5 Laser efficiency

3.5.1 Electron beam energy deposition

Results have so far been given for the electron beam energy and current density in the diode, and the current density transmitted through the mesh into the discharge cavity. In order to calculate the energy deposited in the gas an estimate must first be made of the electron beam energy distribution following the mesh. This would normally involve finding the energy loss of the original beam as it traversed the prefoil and main foil and was attenuated by the mesh. Ideally, a complete Monte Carlo code calculation should be made and deposition profiles computed (as in, for example (63)) but such a facility is not often available. The usual alternative is to begin with the available tables of the loss of energy by electrons as they traverse certain materials[64],[65].

The Berger and Seltzer tables[64] give the stopping powers for particular materials at a range of electron energies, but in relation to the actual distance an electron has travelled rather than the distance travelled along the axis defined by the

original beam direction. These two figures differ greatly due to multiple scattering. A simple scattering factor, 2.8 in (47), is commonly introduced to calculate the energy loss in the direction of the beam, but this oversimplification is particularly inapplicable in cases where, as in this laser, an appreciable fraction of the electron beam does not reach the gas. Further, the Berger and Seltzer tables allow an average energy loss per electron to be found, but assume no reduction of electron number on the beam, which is, again, not the case in this system.

Due to the uncertainties outlined, the possibility of experimentally measuring the deposited electron beam energy has been investigated.

Pressure jump techniques, where a change in gas pressure is related to a temperature rise and hence the deposited energy, would have involved the detection of pressure changes of a few torr in a total pressure of 5 Bar. This small change was due to the relatively small amount of deposited energy expected and the large (litres) volume of gas concerned. A pressure transducer would have been sensitive enough, but such devices had been unsuccessfully used in conjunction with electron beam generators in previous work. The sensitive electronics of the transducer were easily damaged in the "noisy" vicinity of the generator.

An alternative technique involving blue cellophane dye dosimetry was therefore devised. The level of bleaching of a strip of cellophane is directly related to the energy deposited in the cellophane by calibration curves supplied by the manufacturer (Avisco). Therefore, if a certain thickness of gas at a particular pressure could be replaced by a thickness of cellophane of the same stopping power, the sum of the energies

deposited in the cellophane sheets would be equal to that which was deposited in the laser gas.

A consideration of the tables of calculated stopping powers shows that, at down to low kV energies, the stopping powers of materials bear the same ratio to one another, being largely dependent on electron densities. Hence, a certain thickness of gas can be replaced by an equivalent thickness of cellophane found from the relationship

$$t_c = \frac{t_g d_g s_g}{d_c s_c} \qquad (3.2)$$

where t refers to thickness, s to stopping power, and d to density. Subscript c refers to cellophane, g to gas. The densities must be included because the stopping power is defined in terms of MeV cm^2 g^{-1}.

Figures taken from (64) implied, using 3.2, that three layers of 25 μm thick cellophane would therefore be equivalent to 3 cm of Ne at a pressure of 5 Bar.

A single electron beam shot was fired into the evacuated laser chamber, with gas replaced by the cellophane. The resulting pieces of bleached cellophane were scanned on a microdensitometer, at the appropriate wavelength, and the manufacturer's information was used to find the energy deposited cm^{-2} in each. The energy deposited varied spatially across the beam, as in Figure 14, but total deposited energies could easily be found by integrating over its width.

20.1 J were deposited in the cavity at a Ne pressure of 5 Bar, 17.5 J if it was reduced to 4 Bar. Both results were accurate to ± 10% if the manufacturer's data was accepted as correct.

3.5.2 Discharge energy deposition

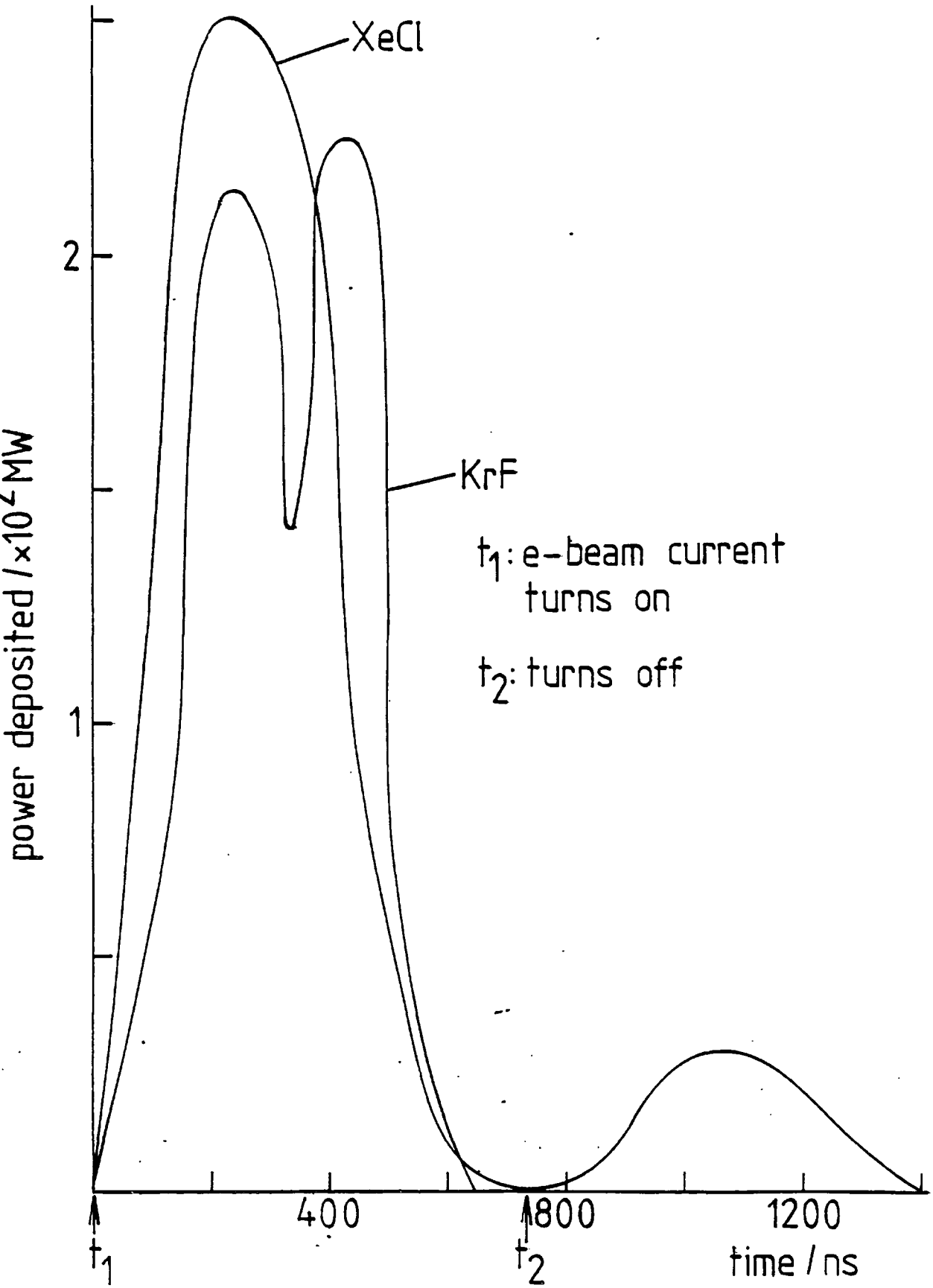
A value for the discharge energy deposited could be found more easily. From the traces of figure 23, of the discharge voltage and current, a plot has been made of the power deposited in the discharge with time, figure 25, assuming that the discharge presented a mainly resistive load. The area under the curve is then the energy deposited, in this case 96 J ± 10%. The energy stored in the 0.55 μF capacitor at 24 kV was 160 J, implying a 60% efficiency of energy deposition.

Figure 25 shows how closely the discharge deposition follows the curve of electron beam deposition, as expected in a sustained laser. Figure 26, also derived from the discharge voltage and current traces, is a curve of discharge impedance against time. Again as expected, the impedance quickly drops to a low, but slowly falling, value for the duration of the electron beam.

The discharge volume was found by dye dosimetry. Thin strips, a few mm wide, were placed at both discharge electrodes and in the mid-plane of the cavity. The strips were thin enough not to affect discharge operation, and the light bleaching caused when the discharge was run was enough to find its dimensions. As expected, the discharge grew from the width of the electron beam passing the mesh ($\simeq$ 2.3 cm) to the height of the anode (5 cm) and was 3 cm wide in mid-cavity. Its cross-sectional area was therefore 10.3 cm^2.

3.5.3 Efficiency calculations

Measured from burn marks, the laser beam area was 4.9 cm^2, implying an extraction volume which was 4.9/10.3 or 48% of the total pumped volume. This means that 800 mJ of energy was



Discharge energy deposition profiles

Figure 25

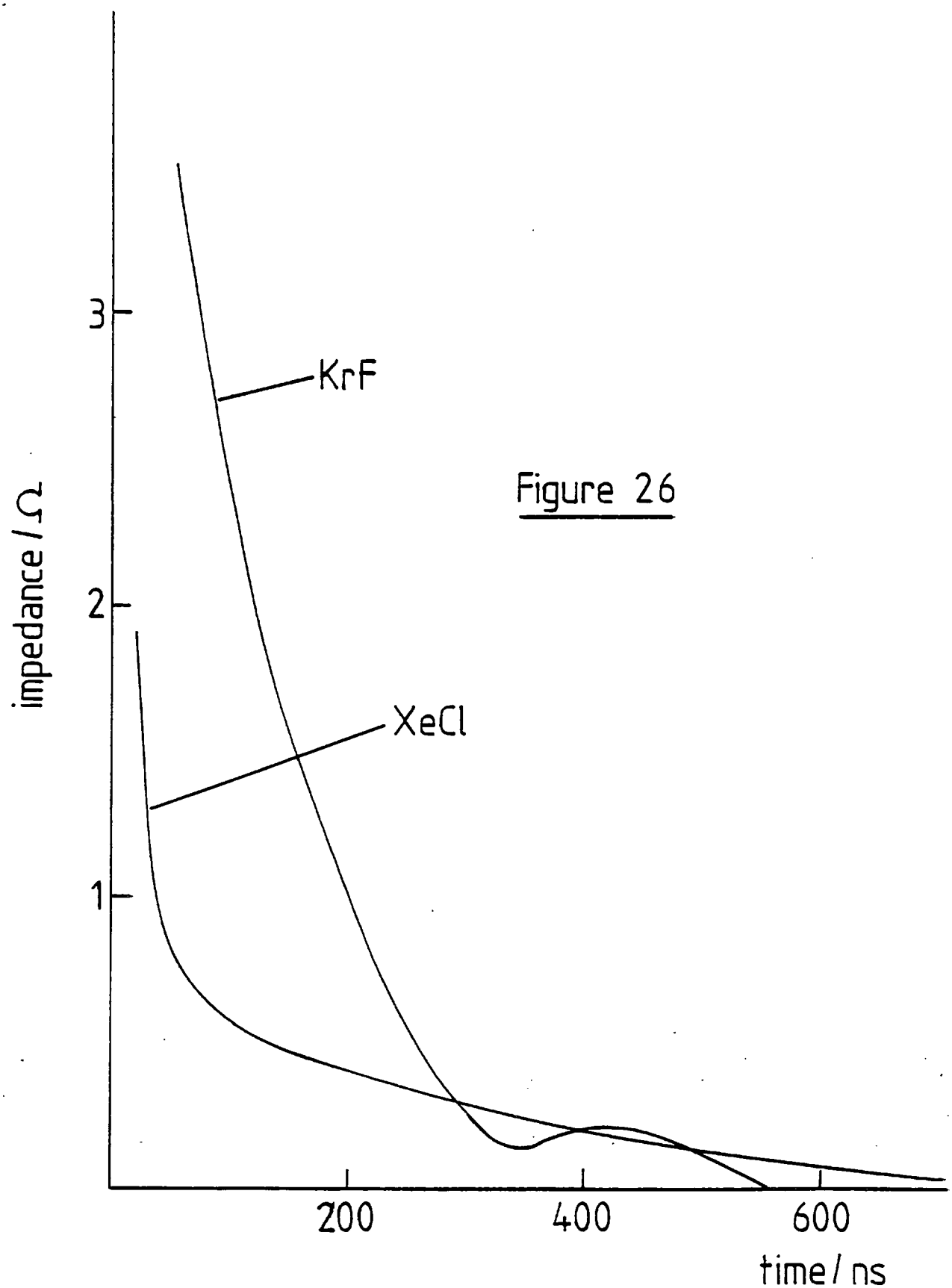


Figure 26

Discharge impedance profiles

extracted from a volume in which the deposited energy was 0.48 (96 + 20) = 56 J, and therefore the extraction efficiency was 1.4%.

A further interesting result was the average power efficiency. This was calculated by considering the average laser output power and the average deposited power during this period, which was rather shorter than the total pumping duration. The figure produced in this way was 3.2%.

3.6 Measurement of laser gain

The gain of the laser has been estimated by the single pass/double pass A.S.E. ratio method. With the arrangement of figure 27, this involved the comparison of the signal received by the photodiode with (S_2) and without (S_1) the back reflector M, a 100% silvered mirror. The cavity windows were set at Brewster's angle and did not contribute to the feedback.

Assuming a gain coefficient instantaneously the same over the entire pump length, and that a one dimensional treatment is adequate (d, L >> window diameter, an important approximation), the Beer-Lambert and inverse square laws imply that[66]

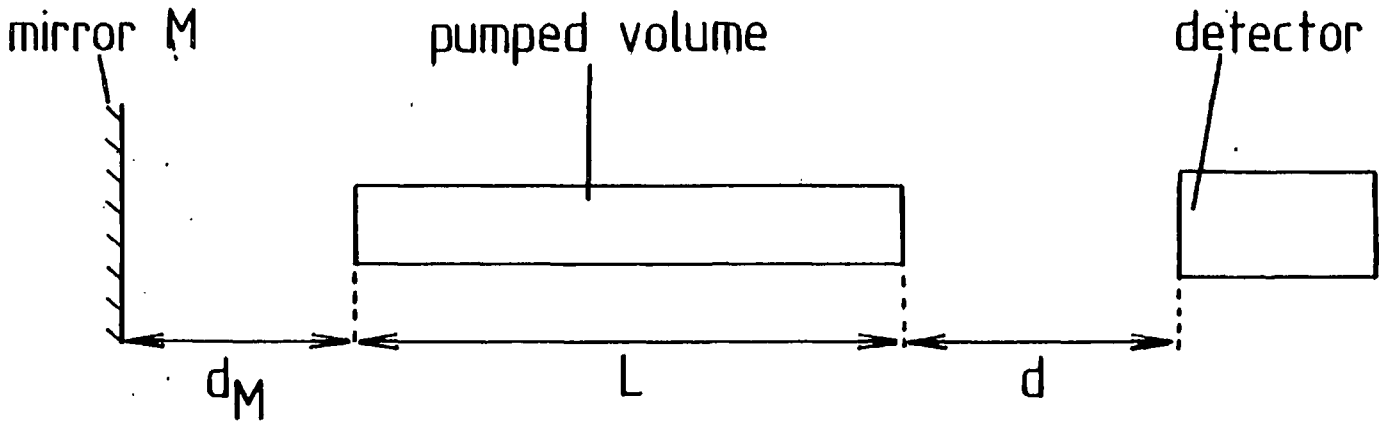
$$S_1 \propto \int_0^L \frac{\exp(\alpha z)}{(d + z)^2}\, dz$$

or

$$S_1 = k\int_0^L \frac{\exp(\alpha z)}{(d + z)^2}\, dz \qquad (3.3)$$

where k is a constant. Similarly, on addition of the reflector M,

Figure 27



The experimental arrangement to measure the laser gain

$$S_2 = S_1 + Rk\int_0^L \frac{\exp[\alpha(z + L)]}{(p + z)^2}\, dz \tag{3.4}$$

where $p = d + L + 2d_m$ and R is the effective reflectivity of mirror M, accounting for the losses at the Brewster's angle window (R = 0.76).

Taking the ratio

$$\frac{S_2}{S_1} = 1 + R\exp(\alpha L)\frac{\int_0^L \frac{\exp(\alpha z)}{(p + z)^2}\, dz}{\int_0^L \frac{\exp(\alpha z)}{(d + z)^2}\, dz} \tag{3.5}$$

and defining a function $F(\alpha)$ such that

$$F(\alpha) = \frac{\int_0^L \frac{\exp(\alpha z)}{(p + z)^2}\, dz}{\int_0^L \frac{\exp(\alpha z)}{(d + z)^2}\, dz} \tag{3.6}$$

(3.6) may be expanded in a MacLaurin series

$$F(\alpha) = F(0) + \alpha F'(0) + \frac{\alpha^2}{2!}F''(0) + \cdots \tag{3.7}$$

It can be easily shown that

$$F(0) = \frac{(d + L)d}{(p + L)p} \tag{3.8}$$

and

$$F'(0) = \frac{(d + L)d}{L}\left[\ln\left(\frac{L + p}{p}\right) - \frac{L}{L + p}\right]$$

$$- \frac{(d + L)^2 d^2}{(p + L)Lp}\left[\ln\left(\frac{L + d}{d}\right) - \frac{L}{L + d}\right] \qquad (3.9)$$

In this case,

$L = 38$ cm, $d = 39.3$ cm, $p = 133.4$ cm ($d_m = 28.1$ cm).

Substituting in (3.8), (3.9) implies that

$$\frac{F'(0)}{F(0)} \simeq 0{\cdot}4 \qquad (3.10)$$

Thus, for a realistic gain value of $\lesssim 10^{-1}$ cm^{-1}, the second term of (3.7) is significantly smaller than the first. To a reasonable approximation, the ratio S_2/S_1 can therefore be rewritten as

$$\frac{S_2}{S_1} = 1 + R\exp(\alpha L)\frac{(d + L)d}{(p + L)p} \qquad (3.11)$$

For the arrangement of gas, discharge, e-beam, etc., which allowed an 800 mJ output, the peak net small signal gain coefficient has been found in this way to be $\alpha = 0.05$ cm^{-1}.

Other methods exist to calculate the gain of a laser[67], but this calculation allows a reasonable estimate to be simply made. The result produced is approximately one third of that reported in typical short pulse discharge[67] or e-beam pumped[68] excimer systems.

3.7 Discussion of results

3.7.1 Optimised operation

Despite the relatively high peak gain of the laser it does not quickly achieve threshold. On electron beam pumping

alone, with a 70 mJ output, laser action only lasts for approximately one third of the period of the pumping pulse. Adding the discharge (figure 24) extends the period of laser operation in both directions, but still laser action only occurs for 250 ns.

The seemingly very high enhancement ratio found by taking the ratio of laser output energies in the e-beam sustained and pure e-beam cases (800/70) is not a fair reflection of the performance of the laser. A better value is the ratio of deposited energies, i.e. 96/20 = 4.8, which is still a high value in comparison with other systems (1.4.1), and reflects the care taken in designing the laser.

Similarly, 800 mJ of extracted energy at a specific energy of 4 J l^{-1} and an average power of 3.2 MW (0.63 MW cm^{-2}) compares favourably with the best results so far reported[47].

3.7.2 Standard operation

The electron beam generator was reliable and with regular maintenance would not lead to the failure of the pressure bearing foil for thousands of shots. To ensure safety against failure due to discharge instability over a similar period, the laser was slightly underrun. This high reliability for the whole system was very important for the success of the experiments to be described in chapters 4-6.

It was found adequate to reduce the charging voltage on the capacitor bank from 24 kV, at a spark gap pressure of 15 psi above atmospheric, to 20 kV at 12 psi. This reduced the amount of energy deposited from the discharge from 96 J to 67.5 J, and from the electron beam from 20.1 J to 17.5 J. The lower electron beam deposition energy was due to the lower stopping power gas mix used: HCl : Xe : Ar : Ne in the ratio

1 : 25 : 190 : 1140, at a Ne pressure of 3 Bar. The total gas pressure was reduced to minimise the strain on the main foil.

Ar was added for two reasons. First, due to its higher density, it increased the stopping power without increasing the total pressure to the same extent as Ne. Second, the laser output pulse length was found to be increased by 30 - 40 ns with a small addition of Ar. There is some indication of the possible improvements which may be made with mixed diluents to the output of an e-beam pumped KrF laser[48], and it has recently been proposed that XeCl efficiencies can be improved by the use of Ar which promotes more rapid vibrational relaxation of the B-state[69]. This improvement must be balanced against the increased absorption at 308 nm by Ar_2^+ molecular ions as the Ar partial pressure is increased. In this case, the addition of 0.5 Bar of Ar to 3 Bar of Ne was optimum.

When a well-defined cavity length was required, Brewster angled laser cavity end windows were fitted. In the standard operating arrangement, output energies were then $\simeq$ 250 mJ (200 ns F.W.H.M. pulse) (the arrangement for 3.8, chapters 4-6). The gain, however, was too great to allow this set-up to produce a polarized output ($0.04\ cm^{-1}$).

In conclusion, these precautions allowed the laser to be fixed at a typical rate of 20 shots $hour^{-1}$ for thousands of shots with a 10% shot-to-shot reproducibility, without failure of the main foil.

Table 5 summarises the performance of the XeCl laser.

Table 5

	Optimised	Standard operating
Output energy/mJ	800	250
Pulse duration (F.W.H.M.)	250	200
Gas mix	Ne:Xe:HCl	Ne:Ar:Xe:HCl
	1260:17:1	1140:190:25:1
Total pressure/Bar	5	3.5
Deposited e-beam energy/J	20	17.5
Deposited discharge energy/J	96	67.5
Extraction efficiency %	1.5	0.5
Gain/cm^{-1}	0.05	0.04

Laser performance summary

3.8 An unstable resonator

The operation of the XeCl laser in an unstable resonator configuration has been studied. Unstable cavities have the capability to provide both good transverse mode discrimination and large mode volume simultaneously.

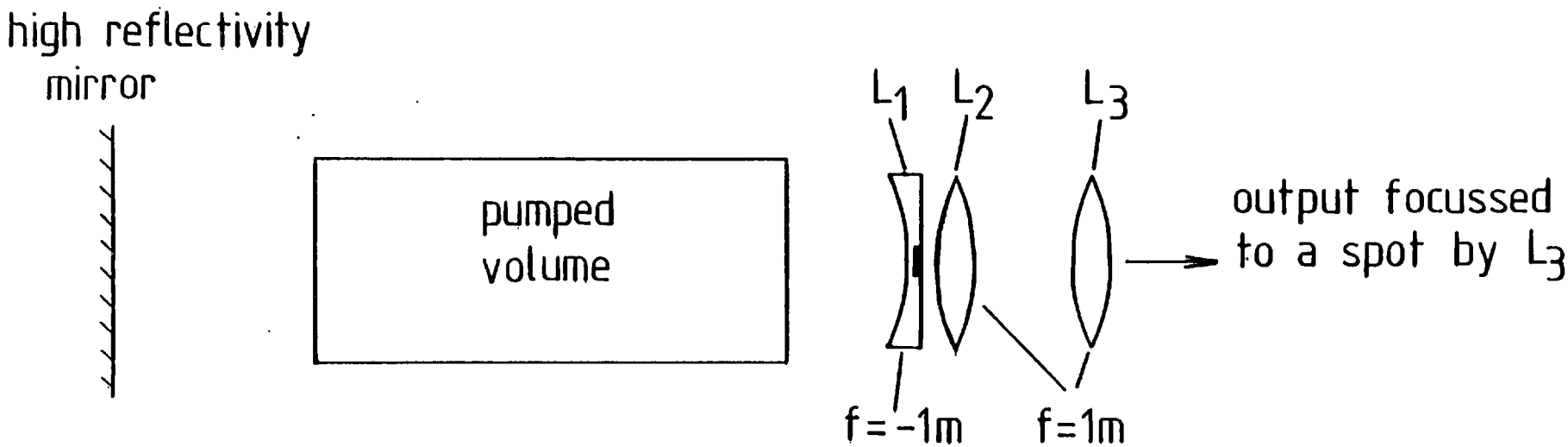
Figure 28 shows the experimental arrangement of the positive-branch unstable resonator chosen. One end of the cavity was formed by the > 97% reflectivity multilayer dielectric mirror and output coupling was effected via lens L_1, a quartz lens with an aluminised, 3 mm diameter central spot coated onto its plane surface. This reflecting spot behaved as a mirror of focal length $\simeq$ -50 cm, and the overall magnification of the combination was 5.8. Lens L_2 rendered the output beam parallel, and L_3 was available to focus the beam down to a spot.

Siegman [70] has shown that for this particular half-symmetric resonator the diffraction loss per mirror "bounce" is $\simeq$ 80%. A much higher magnification would increase this to such an extent that laser action could never build up. Since both the magnification and cavity length, limited by the size of the discharge chamber to be > 1m, of the system were therefore set, so also was the required focal length of L_1 since

$$M = \frac{(1 - R/L)^{1/2} + 1}{(1 - R/L)^{1/2} - 1} \qquad (3.12)$$

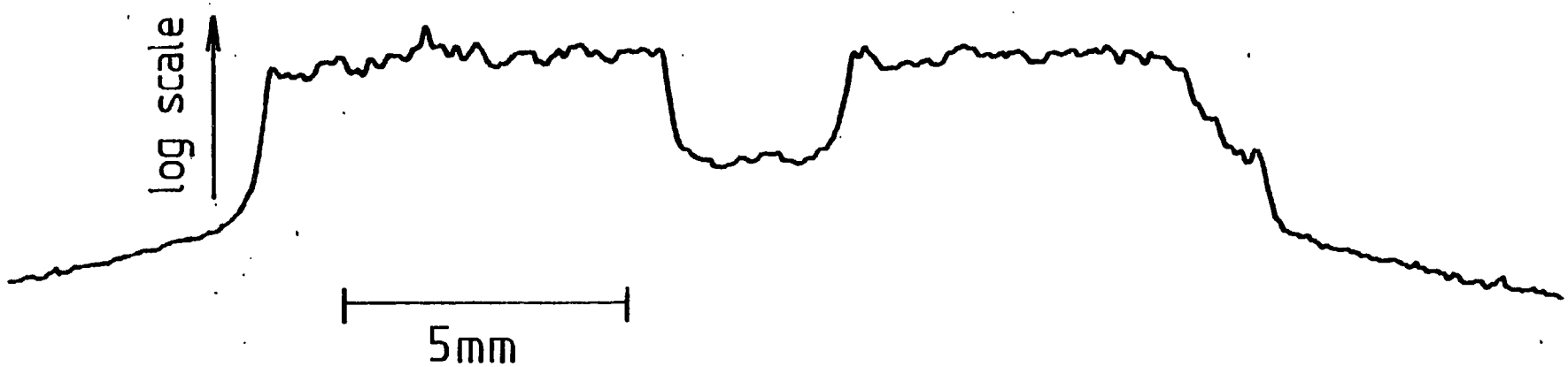
where M is the magnification, L the cavity length and R the radius of curvature of the reflector formed by L_1. The limiting aperture of L_1 was 2 cm, therefore a 3 mm high reflectivity spot was chosen so that this was filled after a double pass of the cavity.

The near-field beam pattern was recorded on Type 665 Polaroid



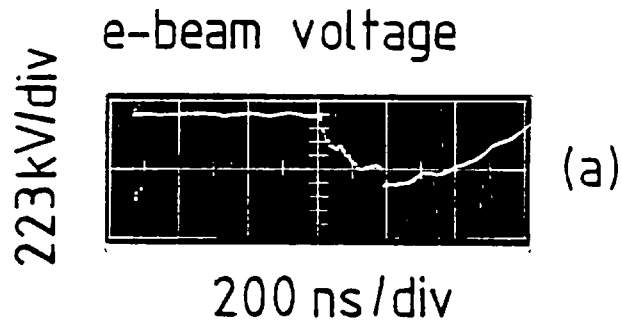
Experimental set up of the XeCl unstable resonator

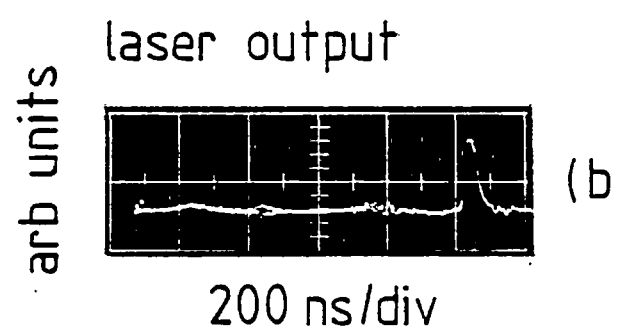
Figure 28



The near-field spatial beam profile at L_2

Figure 29





The laser output from the unstable resonator compared to the e-beam pumping pulse

Figure 30

(Positive/Negative) and figure 29 shows a resultant micro-densitometer trace. The output was calibrated by using known attenuators, and it was seen to be uniform to better than 10% across the whole beam area. Carefully recorded spot burns at the focus of L_3 allowed the beam divergence to be measured : the full angle divergence was $\lesssim$ 0.5 milliradians. 36 mJ was, on average, recorded in the pulse of $\simeq$ 42 ns F.W.H.M. (figure 30), corresponding to an average output power of 0.86 MW and a focussed power density of 0.44 GW cm^{-2}. By comparison, the beam divergence for the case of plane-parallel mirrors (3.7.2) was $\simeq$ 2 milliradians, the average output power 1.25 MW and focussed power density 0.04 GW cm^{-2}.

The use of an unstable resonator has therefore greatly decreased the beam divergence and increased the obtainable power densities by an order of magnitude, but at the expense of total pulse duration. In terms of beam divergence, these results are comparable to those found with positive or negative branch unstable resonators on short pulse discharge excimer lasers[71],[72]. However, the round trip cavity losses have substantially shortened the period for which the laser is above threshold. Figure 30 shows how this duration has been reduced in comparison to the electron beam voltage waveform. A lower magnification arrangement would be necessary to increase the output pulse length but would reduce the output coupling. With a lower loss system it might also be possible to introduce an intra-cavity tuning element, possibly a grating, to produce a beam with both high spatial and spectral quality.

3.9 An electron beam sustained KrF laser

3.9.1 Performance results

While the laser system had been specifically designed to

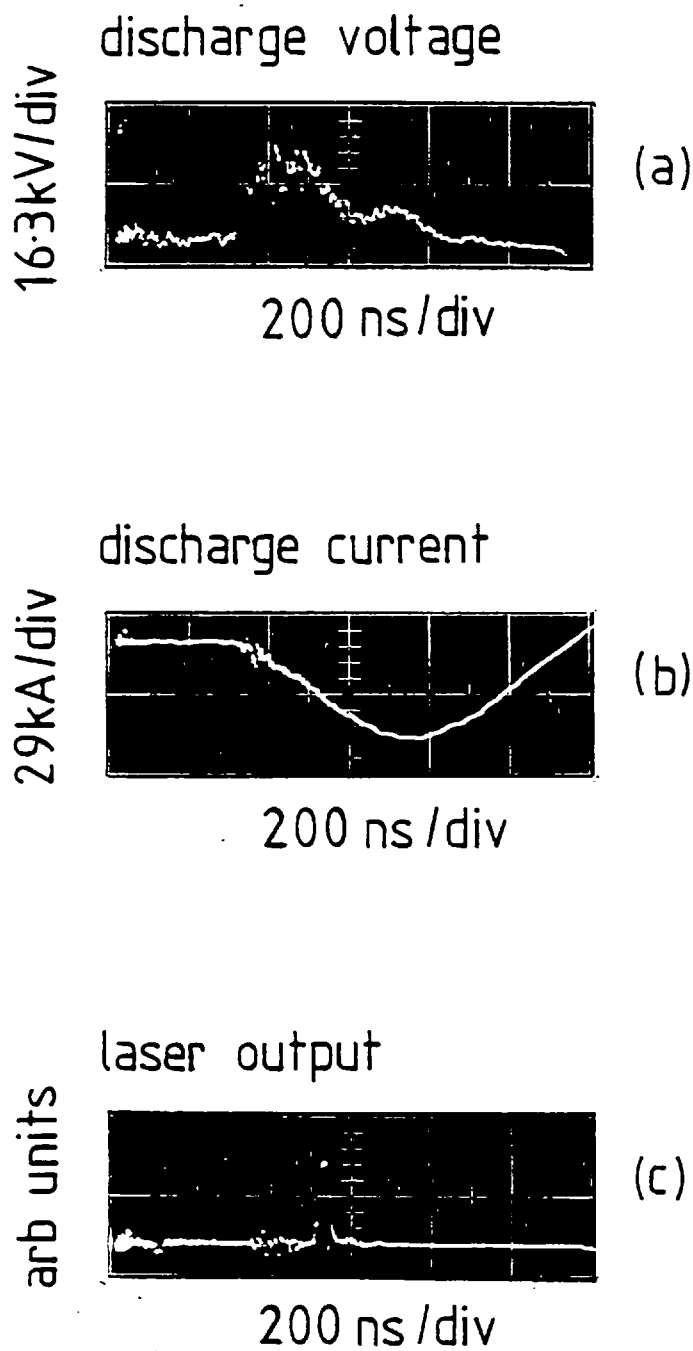
pump the XeCl excimer, it was originally thought that it would prove equally suitable for other rare gas halide excimers. This section, describing a KrF laser, will show that this was not the case, because of the much more electronegative nature of fluorine.

These experiments were carried out on a gas mixture of F_2 and Kr with either Ar or Ne as the buffer gas. The total pressure was estimated from the XeCl results for optimum e-beam energy deposition, and the partial pressures of F_2 and Kr from other discharge or e-beam pumped KrF lasers. The pressure of each constituent gas was then varied in the search for the highest output energies.

Problems of passivation and gas purity were originally considered and rejected as possible causes of the poor results to be described. F_2 for this laser was supplied by a small bomb kept at sub-atmospheric pressure and regularly refilled from a larger cylinder. A leak in this refill system was suspected for some time to be a source of contamination, but when the leak was stopped no improvement in laser output was seen.

Best results were obtained with Ne as the buffer gas at a total pressure of 4 Bar, the other gases being present in the ratio Ne : Kr : F_2 507 : 20 : 1. Laser action began approximately 40 ns before XeCl action would have begun, relative to the e-beam, but lasted for only 30-40 ns (F.W.H.M.). The peak power reached was one third of that observed with XeCl, i.e. $\simeq$ 1 MW corresponding to a pulse energy of 15 mJ.A 0.55 μF capacitance charged to 24 kV made up the discharge circuit.

Figure 31 shows the laser output pulse, together with synchronised discharge voltage and current traces for KrF. The curves of discharge power deposition and impedance,



Characteristics of the KrF laser

Figure 31

figures 25 and 26, have been generated from these. Unlike the case of XeCl, the discharge impedance does not fall to a low but fairly constant value. Similarly, the energy deposition profile begins by following the electron beam but sharply falls off, before rising again, as the discharge impedance collapses. These results imply that the discharge was not being successfully sustained by the electron beam. The rapid, continuous fall of the discharge impedance and the fluctuation in the energy deposition profile after approximately 300 ns, a time corresponding to the end of laser action, must coincide with the discharge becoming unstable.

3.9.2 Explanation of the instability

Long[62] [73] has carried out the most extensive study of electron beam sustained discharge stability.

Onset of an instability was shown to be dependent on the concentration of F_2, the total gas density, the field within the cavity E, and the electron beam current density entering the cavity J_{eb}. With N as the neutral gas density (cm^{-3}), Long gave data for the maximum E/N allowable for stable discharge operation and showed how it was affected by variations in J_{eb}/N and the F_2 concentration. These results were derived with Ar as the buffer gas. For the system under consideration, with Ar as the buffer gas, the best outputs were obtained for a mixture in the ration 190 : 20 : 1 (total pressure 1.5 Bar), while no laser action was observed for half of this Kr concentration (as studied by Long) at any F_2 concentration.

Comparison of this data with the results of Long shows that an instability could be expected to set in, for this F_2 concentration and J_{eb} = 13 A cm^{-2}, at E/N $\simeq$ 16 Td where 1 Td = 10^{-17} V cm^2. Experimentally, the highest voltage reached was

18 kV, corresponding to E/N = 15 Td and reasonable agreement. Long further showed how, for a particular discharge cavity arrangement, there is a minimum electron beam current density which is required before stable discharge operation can occur. As has been seen, J_{eb} = 13 A cm^{-2} was therefore not sufficient to sustain discharge operation for any available set of discharge parameters.

Higher e-beam current densities were not easily available, since they would have required a redesigned electron beam generator. 13 A cm^{-2} appeared to be near the minimum current density required for stable operation, and in this region the uniformity of e-beam energy deposition would also be important. First, longitudinally, e-beam deposition falls off with distance from the mesh and so to maintain current uniformity the electric field is higher in the region of lower charge densities. Thus, the discharge is harder to stabilise. Second, the rib structure supporting the foil causes transverse non-uniformities by a shadowing effect and discharge instabilities may begin in the region of highest current density between the ribs.

CHAPTER 4

A FAST, HIGH REPETITION RATE OPTICAL SHUTTER

4.1 Introduction

The principle of mode-locking when applied to excimer lasers, which will be introduced and discussed in Chapter 6, should allow the large optical energies available to be concentrated into intense ultra-short UV pulses. Chapters 4 and 5 will consider the basic component required for active mode-locking, a fast optical shutter which can be regularly re-opened at the roundtrip frequency of a laser cavity.

The shutter can be simply considered as providing loss modulation at a frequency c/2L, where L is the cavity length. Thus, light incident on the modulator, situated at one end of the cavity, during a certain part of the modulation cycle, will again be incident at the same point of the next cycle after one roundtrip of the laser resonator. Light which sees a loss at one time will again see a loss after one roundtrip of the resonator. Hence, all of the light in the resonator will experience loss, except that which passes through the modulator when the modulator loss is zero. Light therefore builds up in narrow pulses in these low-loss time positions. The narrowness of these pulses is governed by both the speed of the modulator and the number of passes the pulse of light generated makes through it (determined by the time for which there is optical gain) neglecting other shortening mechanisms such as gain saturation.

Most conventional active mode-locking experiments have involved the application of a broad loss modulation, e.g. (74), and allowed short pulses to build up after many roundtrips.

However, in the case of excimer lasers, where even the sustained discharge technique permits only a relatively limited number of roundtrips, such techniques are not ideal, although they have been used to give pulses of $\simeq$ 2ns duration[75]. A preferable arrangement would therefore be to begin with a fast, efficient optical gate - in the case to be considered, a train of short duration voltage pulses applied to an electrooptic modulator.

Such a fast gate was first demonstrated in pulse shaping experiments[76] and has been used for both visible[77] and UV[78] mode-locking. This chapter will consider in detail the operation of the optical shutters of (77) and (78), an electrooptic phase modulator driven from a GaAs semiconductor switch. Chapter 5 will then outline a design study which was carried out, in the light of these results, to improve the operation and consider the limitations of this technique, and will describe the much faster light modulator which was developed.

Although the mode-locking of excimer lasers was the motivation behind this work, it is not wavelength selective, and the results are equally applicable to many visible and UV wavelengths.

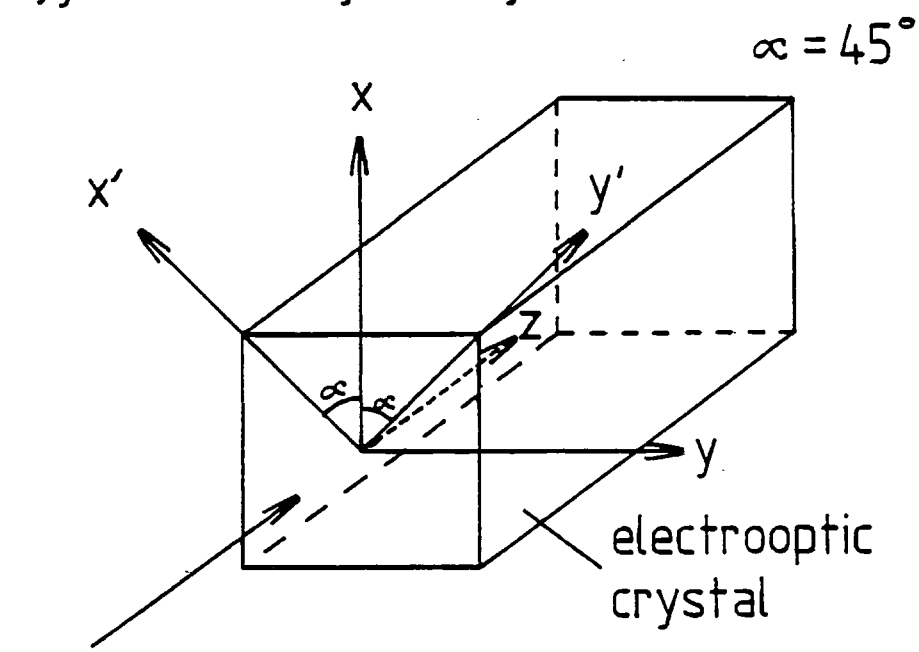
4.2 Optical pulse generation by electrooptic phase modulation

In certain crystals the application of an electric field produces a change in the refractive index of the material which is proportional to the field applied. The crystals which will be considered in this work are those commonly supplied in commercial modulators : potassium dihydrogen phosphate, (KH_2PO_4) known as KDP, potassium dideuterium phosphate,

Figure 32

z : fourfold optic axis

x, y : twofold symmetry axes.



Symmetry axes of $\bar{4}2m$ crystals

(KD_2PO_4) or KD*P, and ammonium dihydrogen phosphate, ($NH_4H_2PO_4$) or ADP. All three have the same crystal symmetry ($\bar{4}2$ m), and their response to an applied field takes the same form.

Consider the crystal of figure 32, where x, y and z are the symmetry axes (z fourfold), with a field E_z applied along the z-axis. Any light incident and travelling parallel to the z-axis can be split into two polarizations along the orthogonal directions x' and y' as shown. On the application of E_z, these two polarizations travel through the crystal with different velocities corresponding to different refractive indices. For a $\bar{4}2$ m symmetry, these are

$$n_{x'} = n_o - \frac{n_o^3 r_{63} E_z}{2} \qquad (4.1)$$

and

$$n_{y'} = n_o + \frac{n_o^3 r_{63} E_z}{2} \qquad (4.2)$$

where n_o is the ordinary and n_e the extraordinary refractive index of the crystal, and r_{63} is an electrooptic coefficient.

A phase retardation Γ is therefore generated between these two components at the output plane of the crystal. If a voltage V is applied to the crystal of length l, then

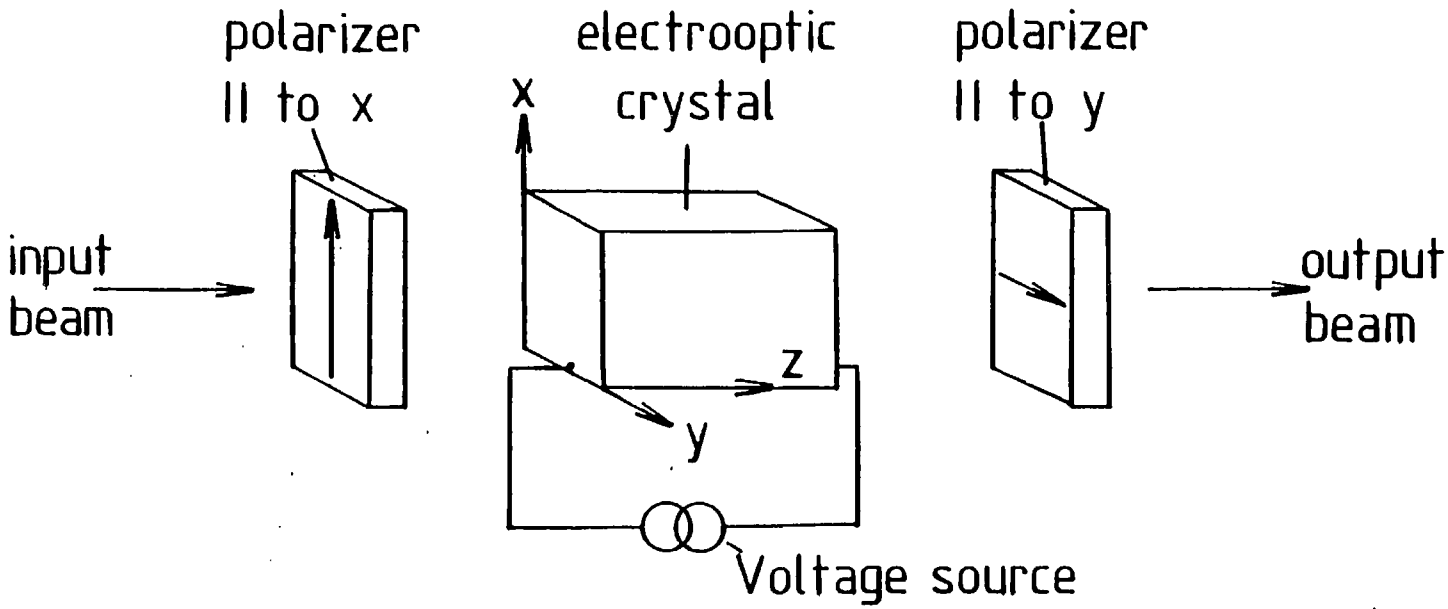
$$\Gamma = \frac{\omega n_o^3 r_{63} V}{c} \qquad (4.3)$$

or

$$\Gamma = \pi \frac{V}{V_\pi} \qquad (4.4)$$

where ω is the angular frequency and λ the wavelength of the light. V_π is known as the "half-wave" voltage and is given by

Figure 33



Simplified diagram of an electrooptic amplitude modulator

$$V_\pi = \frac{\lambda}{2 n_o^3 r_{63}} \qquad (4.5)$$

A simplifed electrooptic amplitude modulator is shown in figure 33. It consists of an electrooptic crystal (in this case a Pockels cell) placed between two crossed polarizers, whose polarization axes lie at angles of 45° to the x', y' axes. The incident field is parallel to x at the input face of the crystal and thus has equal, in-phase, components along x' and y'. A simple analysis[79] shows that the output intensity I_o emerging from the analysing polarizer is related to the input intensity I_i by

$$\frac{I_o}{I_i} = \sin^2\left[\frac{\pi V}{2 V_\pi}\right] \qquad (4.6)$$

This is the loss-free, steady state condition. Amplitude modulation results when V varies as a function of time. If a voltage pulse is applied to the crystal, this results in the generation of an optical pulse from the modulator. The following section will consider how fast voltage pulses may be repetitively generated for this purpose.

4.3 The repetitive generation of short duration, high voltage electrical pulses

The use of Pockels cells for the high-speed switching of optical pulses is not a new technique. Pulse slicing with fast risetimes has recently been achieved with laser triggered spark gaps[80], krytrons[81] or avalanche transitors[82]. None of these options has the capability of low jitter, high (100 MHz)

repetition rate operation which is necessary for mode-locking experiments. However, the advent of light actuated semiconductor switches has now made it possible to manipulate high voltage pulses with picosecond precision.

4.3.1 Auston switch technology

Photoconductive switches[83] generally consist of a piece of high resistivity or semi-insulating semiconductor, such as Si[84] or GaAs[85], incorporated in a microstrip transmission line structure (e.g. figure 37). As an intense, ultrashort laser pulse illuminates the gap between the switch electrodes, electron-hole pairs are created and quickly establish the continuity of the line so that the voltage applied is efficiently transmitted. To end the switching action, a second light pulse shorts the input to ground or, alternatively, the recombination of carriers re-establishes the high dark impedance of the device.

For a semiconductor with a bias voltage V_o applied, assuming that a delta-function-like light pulse activates the device at time $t = 0$, that the number of carriers decays exponentially with a single time constant τ and that the dark conductance of the device is negligible, the conductance across the gap can be expressed as

$$G(t) = G_0 \exp(-t/\tau) \qquad (4.7)$$

where G_o is the conductance immediately following the illumination of the semiconductor. G_o can be related to the gap length l and pulse energy ϵ by (86)

$$G_0 = Z_0^{-1} = \frac{4n_r}{(n_r + 1)^2} \cdot \frac{e\epsilon\mu}{h\nu l^2} \qquad (4.8)$$

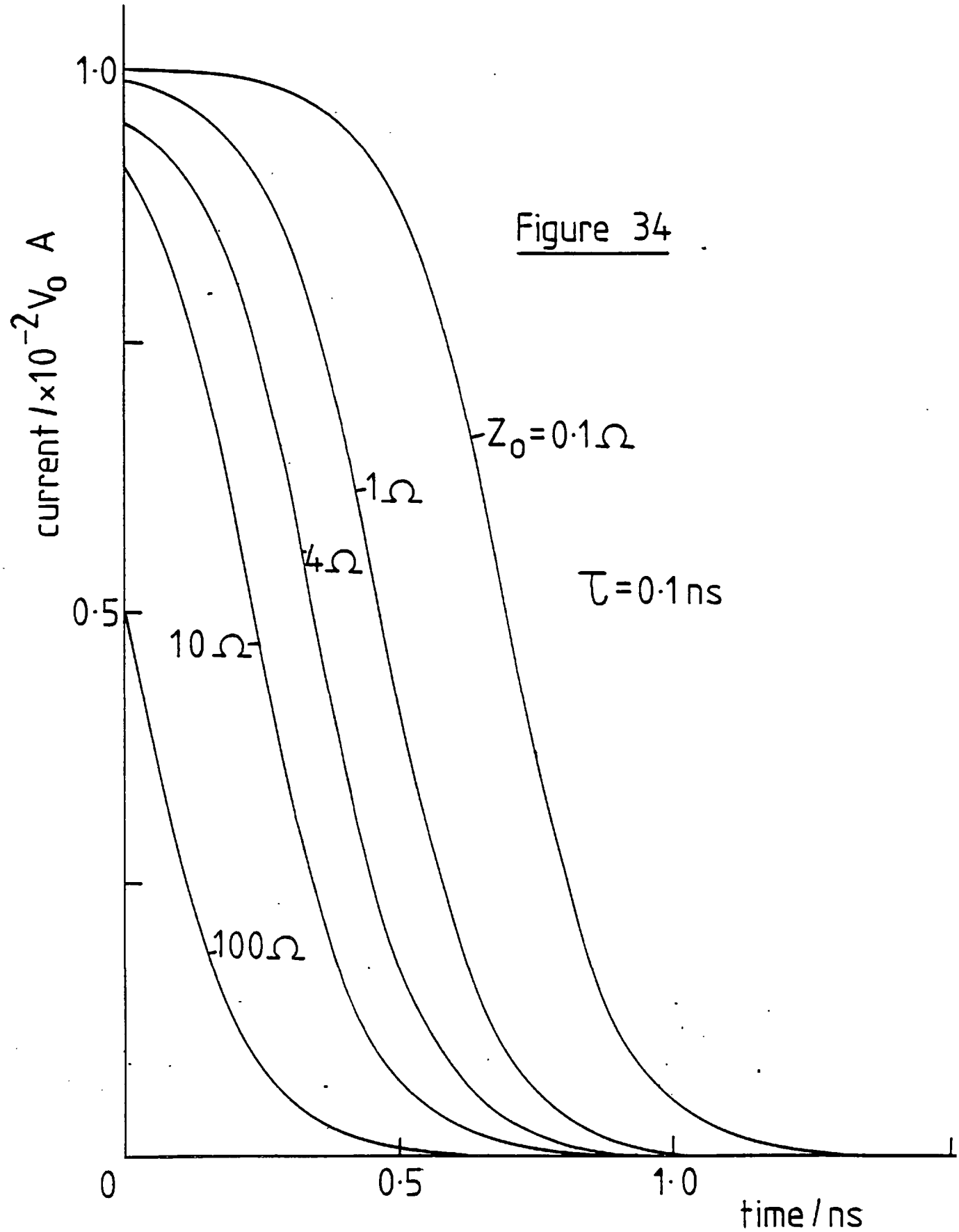


Figure 34

Current delivered to a 50Ω load from a GaAs switch

where n_r is the refractive index of the crystal and $4n_r/(n_r + 1)^2$ accounts for light lost by reflection, $h\nu/e$ is the energy of the photons in eV, and μ is the sum of the electron and hole mobilities.

The total impedance of the device can be expressed by

$$Z(t) = R_c + G(t)^{-1} = R_c + Z_0 \exp(t/\tau) \qquad (4.9)$$

where R_c is the contact resistance of the electrodes, and the current switched into a load of impedance Z_L is

$$i(t) = \frac{V_0}{2Z_L + R_c + Z_i \exp(t/\tau)} \qquad (4.10)$$

if the impedance of the charging cable is also assumed to be Z_L. Although the conductance of the gap decreases exponentially, the current has an exponential shape only if the device is not saturated by the light pulse.

In the experiments to be reported in this chapter, a GaAs switch doped with Cr was used. The switch had a dark resistivity of $10^8\,\Omega$ cm and the carrier recombination time τ was $\lesssim$ 100 ps [87],[88]. Light pulses were applied to the switch from a mode-locked dye laser. Figure 34 shows a set of curves representing the time evolution of the current switched as given by equation 4.10 [87]. Z_L is 50Ω and R_c is assumed negligible compared to 100Ω. The maximum voltage which can be switched in this combination is $V_o/2$, corresponding to a maximum current of $V_o/100$ into a 50Ω load. This limit is approached if $Z_o << 100\Omega$.

4.3.2 The mode-locked dye laser

The dye laser had the capability of delivering pulses of

Schematic diagram of the dye laser

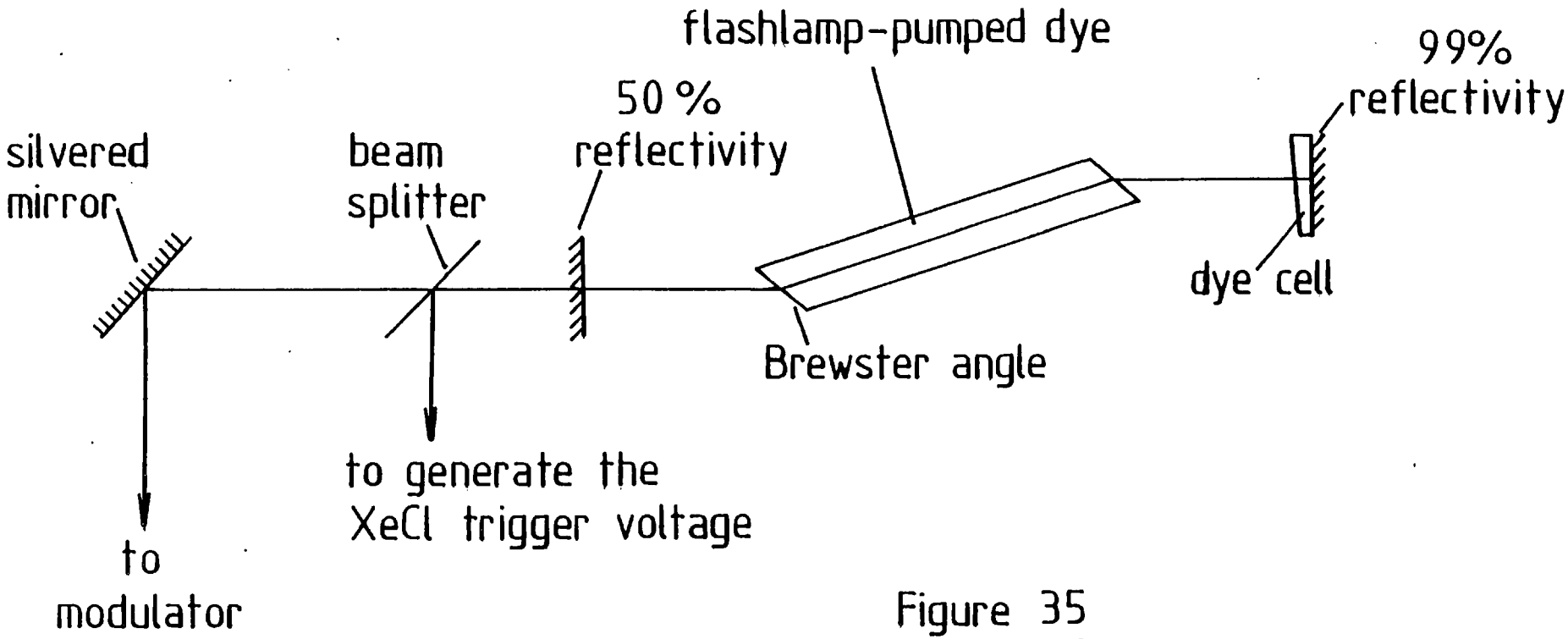


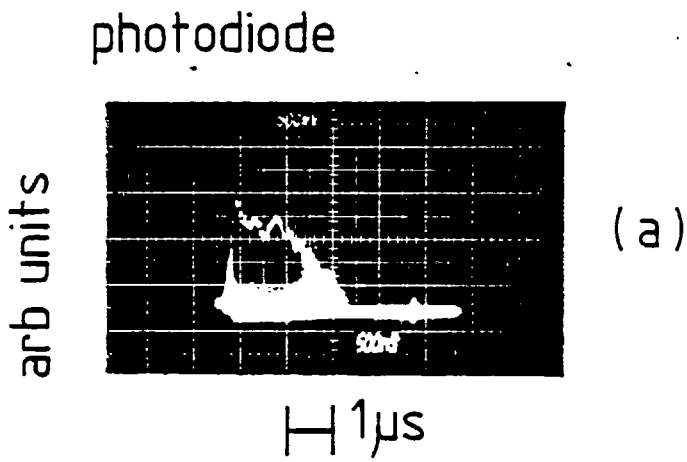
Figure 35

light to the GaAs switch with energies of tens of μJ and durations of less than 10 ps. A schematic diagram of it is shown in figure 35.

The laser[77], [89] consisted of an 18 mm o.d., 10.5 mm i.d. ablative flashlamp and a 13 mm o.d., 6 mm i.d. dye cell placed along the focal lines of a 180 mm long reflecting elliptical cavity head. Brewster angle windows were set on the dye cell. The flashlamp was triggered by applying a pulse of $\simeq$ 30 kV to the centre pin of a commercial motor spark plug screwed into the earthed connection to the flashlamp. This pulse was obtained by stepping up the output from a low voltage thyratron trigger unit, fired manually, with a small pulse transformer. Energies of typically 1000 J were deposited in the flashlamp from a 5 μF capacitor. In such an ablative system, where the flashlamp is evacuated, the discharge first begins to run on the residual low pressure gases. Wall material is then fed back into the discharge by ablation, and a high pressure discharge is quickly set up.

The light from the lamp pumps the flowing laser dye in its cell. In this case the dye used was Rhodamine 6G at a concentration of 2×10^{-4}M in ethanol. It is relatively simple to passively mode-lock such a laser (see Chapter 6 for a discussion of mode-locking). The cavity was formed by a 50% reflectivity multilayer dielectric output coupler and a 99% reflectivity mirror (at 600 nm) onto which a 2 mm thick contacted dye cell was placed, containing an approximately 5×10^{-5}M solution of DODCI (3,3'-Diethyloxadicarbocyanine Iodide) in ethanol. The cavity length was > 1m. Without tuning elements and un-mode-locked, the laser output was $\simeq$100 mJ in a pulse of 3 μs duration at 610 nm. Figure 36(a) shows a photodiode trace

Figure 36



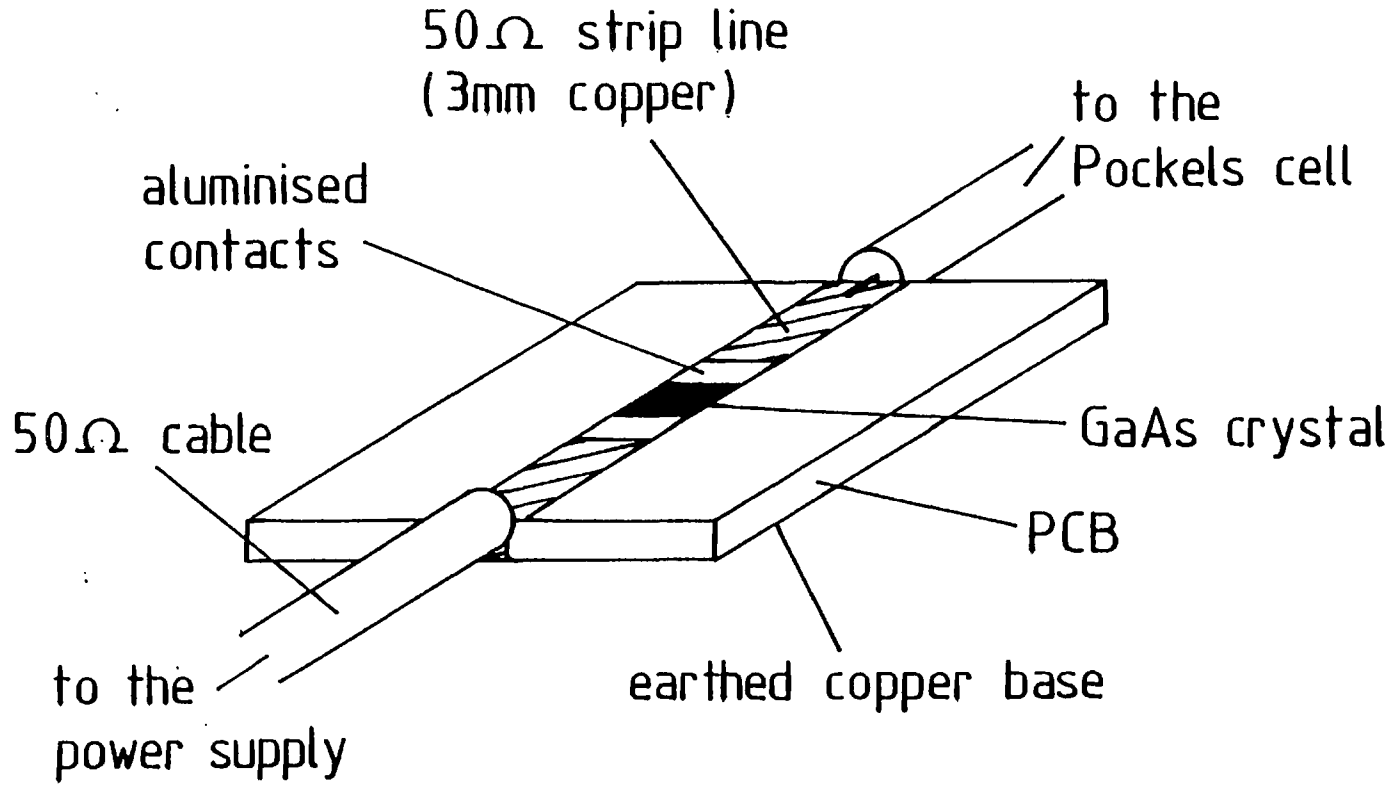
Dye laser output and the resultant voltage pulse train generated from a GaAs switch

of a mode-locked pulse train obtained from this configuration. The total output energy was $\simeq 30$ mJ, corresponding to an average energy per pulse of $\simeq 30$ μJ. Pulse widths of 5 ps have been measured from this laser on a Photocron streak camera[77], and the fluctuation in the total output energy was better than 10%.

4.3.3 Pulse generation

Most of the light from the dye laser illuminated the GaAs switch, constructed and mounted as shown in figure 37. Sharp aluminium electrodes were evaporated onto a piece of GaAs to define a 3-4 mm gap which could be charged to greater than 3 kV without breakdown. The crystal was then cemented onto a piece of printed circuit board which was impedance matched to 50Ω co-axial lines for charging and pulse transmission. Silver-loaded conducting paint was used to contact the copper lines of the circuit board to the aluminium crystal electrodes.

The switch was changed to up to 3.5 kV from an E.H.T. unit, and the voltage pulse train produced by the dye laser light was either attenuated and monitored on a Tektronix 7834 oscilloscope (figure 36(b) for 3 kV charging) or applied to the contacts of the Pockels cell in the light modulator. The efficiency of operation of Cr doped GaAs switches and the difficulties of measuring the short pulses generated from them, due to the limiting bandwidths of oscilloscopes, has been studied[87]. Equations 4.8 to 4.10 can, however, be used to predict the performance of the switch when illuminated with 30 μJ pulses from the dye laser. In equation 4.8, where $n_r = 3.3$[90], $\epsilon = 30$ μJ, $\mu \simeq 9000$ cm^2/V$_s$[91], $l = 3$ mm, and $\nu = c/610 \times 10^{-9}$Hz, then Z_o, the impedance of the switch immediately following illumination, is 1.3Ω. This is a lower limit on Z_o and on the peak current switched in figure 34. Under normal circumstances only a portion of the dye laser light would fall on the switch



The GaAs switch in a 50Ω line

Figure 37

to ensure reasonably uniform illumination between the electrodes. This would increase this limiting impedance to 2-3Ω. Also, the equations used depend on the validity of a number of assumptions and, most importantly, that $R_c << 100\Omega$. This may be over-optimistic[91] and the effect of contact resistance could substantially reduce the efficiency of operation of the switch.

Focussing the light such that the full pulse energy fell between the switch electrodes could increase the efficiency of switching, but more often meant that one of the Al-GaAs junctions was not fully illuminated. When this occurred, the contact would not behave ohmically, the efficiency of the switch would fall, and surface tracking could often proceed between the unilluminated electrode and the illuminated conducting region. Once a track developed in the surface of the crystal it was necessary to replace it. This problem was always present, and led to regular switch failure, but it was made less critical by, at first, not focussing the dye laser output, and later by covering the switch with a transparent epoxy resin.

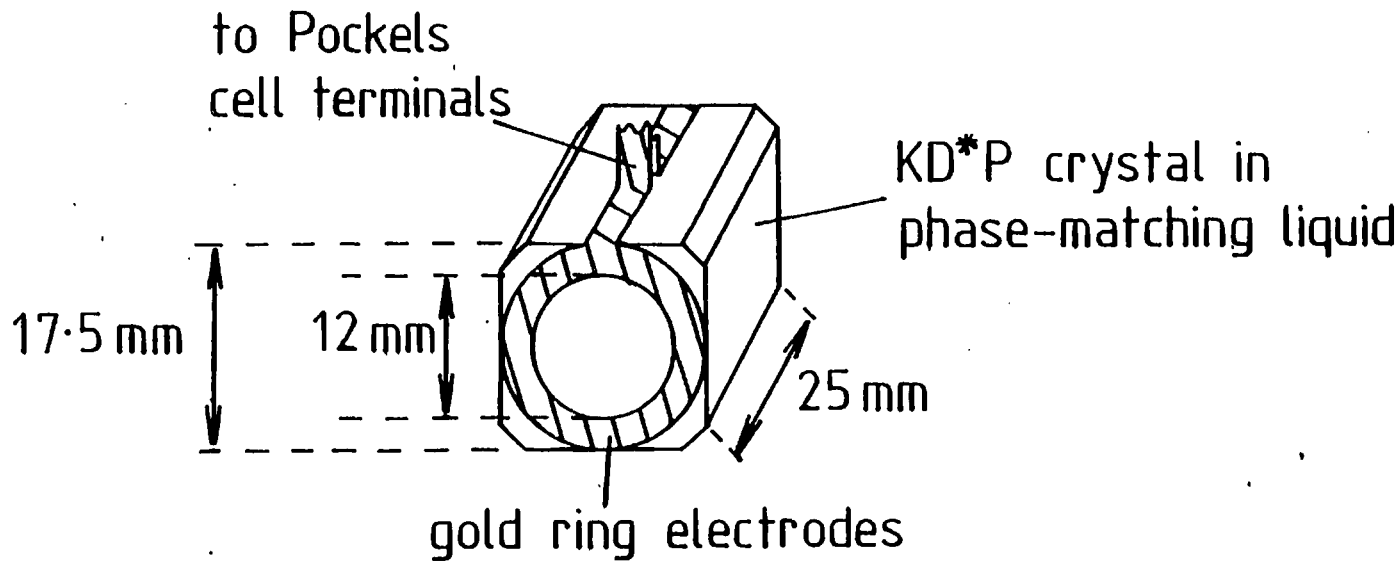
The calculations given, and a consideration of the pulse trains recorded from a GaAs switch (figure 36(b)) along with a recognition of the limiting effects at these frequencies of cable dispersion, oscilloscope risetime, etc., would imply that the total switch impedance was several ohms, with the resultant current output of figure 34. Section 4.4 will consider the results obtained when these pulses were used to drive an electrooptic phase modulator.

4.4 A Pockels cell as an optical shutter

4.4.1 The Pockels cell

Experiments were carried out to study the operation of the

Figure 38



The Pockels cell crystal and electrodes

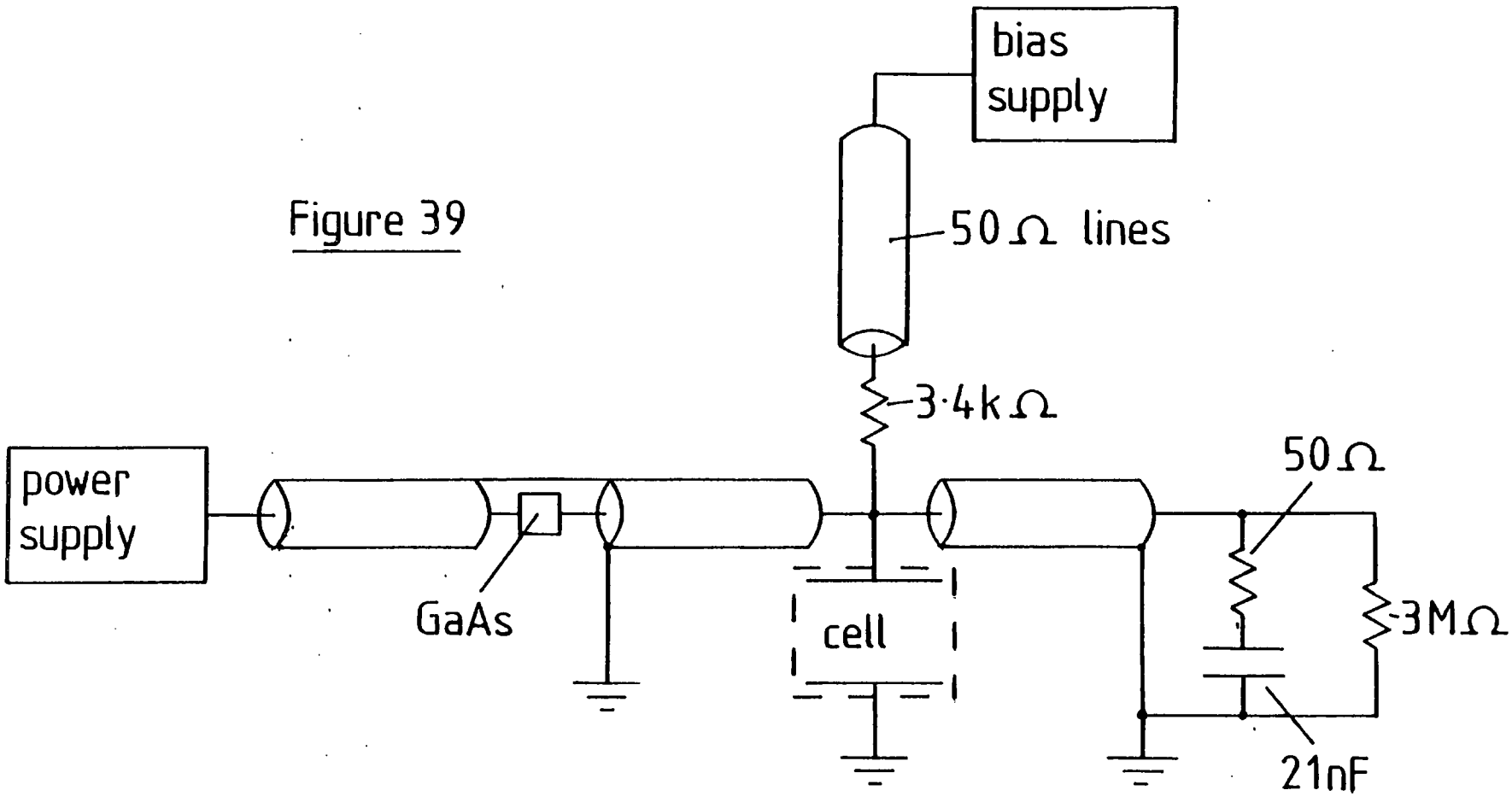
electrooptic phase modulator driven by voltage pulses from a GaAs switch and previously used for mode-locking[77],[78]. This modulator took the form of a commercial Pockels cell, model 12KD, supplied by Electro-Optic Developments Ltd. of Basildon, Essex. Its construction is shown in figure 38. The crystal was z-cut, 97% deuterated KD*P, with gold ring electrodes providing the longitudinal electric field. The circular electrode aperture was of 12mm diameter, and the crystal length was 25mm. A half-wave voltage at 633nm of 4kV and a capacitance of 5pF were specified by the manufacturers. The crystal was placed in the cell between two BK7 laser quality windows and surrounded by a phase-matching solution.

A light amplitude modulator was formed by setting the Pockels cell between two crossed Glan Thomson polarizers (figure 33). Alignment was carried out by the "Maltese Cross" method, with the He-Ne laser used to align the XeCl laser cavity, as follows. A short focal length converging lens placed after the first polarizer and before the Pockels cell cast a dark image of a (Maltese) cross with a red background onto a screen beyond the second polarizer. When the centre of the cross coincided with the original direction of the red beam, the z-axis of the crystal was accurately aligned (i.e. lay colinear with the beam). The position of the cross was varied by changing the angle of tilt of the Pockels cell, and care was taken to send the alignment laser through the centre of the cell and polarizers.

4.4.2 Triggering and synchronisation

The modulator was probed with the XeCl laser. This work could have been carried out more easily with a faster repetition rate laser, but it was decided that the modulator should be tested with the laser it was finally intended to mode-lock, in

Figure 39



The Pockels cell driving circuit

order to have to solve the problems of triggering and synchronisation only once.

Approximately 8% of the output of the dye laser was reflected from a beam splitter and projected onto a second GaAs switch with a 1 mm interelectrode spacing. This was charged to 800V and a voltage edge was generated from it as soon as the dye laser began operation. The edge was fed into the 10V external trigger of the Maxwell trigger unit, and hence the XeCl laser was fired (Chapter 2). A total delay of $\lesssim$ 2 μs was measured between the dye laser firing and the excimer laser light pulse emerging, which meant that the excimer probe beam was passing through the modulator as it was being driven by pulses produced from the late centre of the dye laser train (figure 36). This situation was adequate and could not easily be improved.

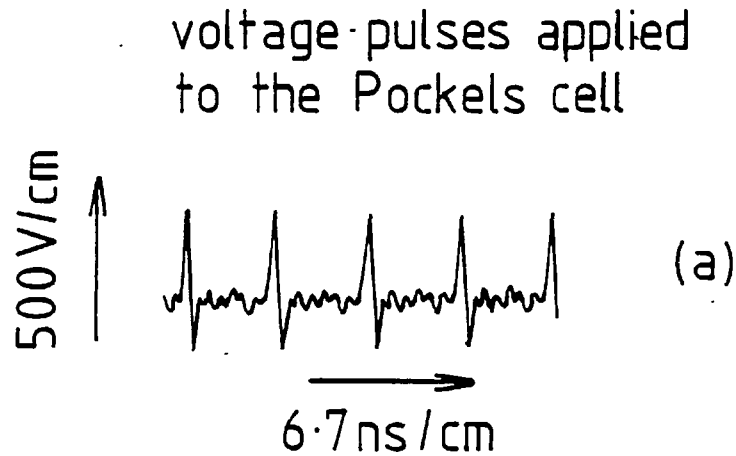
4.4.3 The Pockels cell driving circuit

Figure 39 shows the circuit developed to efficiently drive the Pockels cell with voltage pulses from the GaAs switch.

The bias power supply, isolated from the short voltage pulses by a 3.4 kΩ resistor, allowed a standing voltage to be applied to the Pockels cell (necessary for mode-locking). Theoretically, pulses from the illuminated GaAs switch would be efficiently transmitted down a short length of 50Ω coaxial cable, across the Pockels cell, and into the second terminated piece of 50Ω cable which prevented pulse reflection. Since the switch had a finite impedance when unilluminated, a 3MΩ resistor was added across the termination to prevent slow voltage build-up across the Pockels cell.

With the switch charged to 3kV, 600V pulses were transmitted towards the Pockels cell (oscilloscope measurement). When the 50Ω input oscilloscope was then used as a termination in figure 39 in place of the 50Ω/21 nF combination, the pulse height was

Figure 40



Pockels cell driving voltage and response

reduced to 65% of this value and no substantial ringing or reflected pulses were observed. Hence, a clean train of short pulses was being applied to the connections of the Pockels cell.

4.4.4 Modulation results

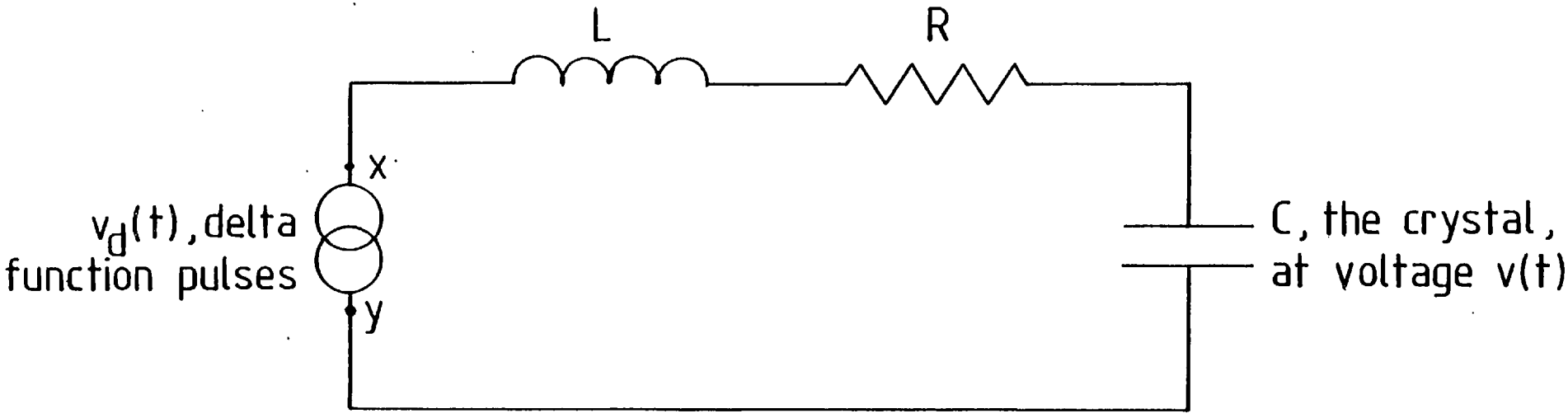
With no bias voltage, the modulated light output of figure 40(b) was recorded when the train of voltage pulses of figure 40(a) was applied to the Pockels cell. The light output of the modulator is a direct representation of the voltage between the Pockels cell ring electrodes (equation 4.6), therefore the sharp pulses of figure 40(a) have been broadened and begun to ring in their transmission from the cell contacts to the ring electrodes.

In order to estimate the peak voltage being developed across the Pockels cell crystal, a plot was made of the signal recorded by the photodiode against a bias voltage applied to the cell. The modulated light output was then recorded (figure 40(b)) with the same attenuation/photodiode arrangement. A direct comparison of the two showed that only $\simeq$ 150V was being developed across the crystal (V_π measured to be 1.4kV).

4.4.5 Circuit analysis

To explain the form of the voltage train appearing across the Pockels cell crystal, an analysis of the equivalent circuit diagram of figure 41 was carried out. R and L are the resistance and inductance respectively of the circuit connecting the ring electrodes to the cell connections (figure 38), and the crystal is modelled as a pure capacitance C. The driving voltage $v_d(t)$ is that voltage which appears across the Pockels cell terminals, a series of short pulses from the GaAs switch (figure 40(a)). The circuit response to a single pulse can be simply calculated if its shape is approximated to a delta function, or infinitely

Figure 41



x, y: Pockels cell terminals

Circuit to model the performance of the Pockels cell

sharp spike, at t = 0. If v(t) is the required voltage at the crystal electrodes, a Laplace Transform analysis shows that

$$v(t) = \frac{\exp(-Rt/2L)\sin(\omega t)}{\omega LC} \qquad (4.11)$$

where $$\omega = \sqrt{\frac{1}{LC} - \frac{R^2}{4L^2}}$$

Since the peaks of transmission for the modulator correspond to maxima in $v(t)^2$, the pairs of peaks in 40(b), occurring in response to each incident sharp voltage pulse, must appear at times of $t = \pi/2\omega$ and $t = 3\pi/2\omega$ (from equation 4.11).

At these GHz frequencies, the simple gold leaf contacts of the Pockels cell (figure 38) may have a substantial inductance and resistance. An approximate skin depth calculation would imply that R is small enough such that

$$\frac{R^2}{4L^2} \ll \frac{1}{LC} \qquad (4.12)$$

and therefore the period of figure 40(b) gives a value for L, assuming that C = 5pF, as claimed by the manufacturers, of $L \gtrsim 100$nH. Although the total contact and loop inductance of the cell is difficult to calculate, available formulae[92] would suggest that this value is of the correct order.

4.5 Conclusion

Limited by the available light and the need for a reliable device, a GaAs switch has been used at voltages of $\gtrsim$ 3kV.

Illumination by mode-locked dye laser pulses has allowed voltage pulses of $\gtrsim$ 1kV to be transmitted from the switch into a 50Ω line with a shortest pulse length of perhaps 200 ps. However, the combination of Pockels cell inductance and capacitance has prevented more than a fraction (15%) of this peak voltage from being developed across the crystal electrodes, and that in a broad ringing waveform. Therefore this method of light pulse generation, although successfully used in mode-locking experiments largely wastes the narrow, high voltage pulses from the semiconductor switch by inefficiently coupling them to the electro-optic crystal. Furthermore, because of the phase matching solution and BK7 windows, the transmission of light by this cell at 308 nm is only 67%.

In Chapter 5 the methods which were considered to solve the problems outlined above will be reviewed, leading to the description of a successfully redesigned, simple, fast modulator. Chapter 6 will compare the mode-locking results achieved with both modulators.

CHAPTER 5

REDESIGNING THE ELECTROOPTIC PHASE MODULATOR

5.1 Introduction

In response to the results and conclusions of Chapter 4, a number of different techniques have been considered to efficiently drive a light modulator with the short voltage pulses from a GaAs switch. This chapter will begin by discussing some of the limitations of the high frequency operation of electrooptic modulators. It will then describe the experiments which were carried out to assess the usefulness of a complete KDP crystal removed from a commercial Pockels cell. This will include a discussion of the possibility of using a Blumlein pulse forming line as a means of producing controllable, short duration voltage pulses to drive an electrooptic crystal. Finally, the design and performance of a fast, efficient modulator based around a smaller aperture, shorter active length KD*P crystal will be described.

5.2 Design criteria

At the modulation frequencies considered in this chapter, the voltage across an electrooptic crystal may appreciably change in the time it takes for the probe light to traverse the crystal. Although a voltage pulse with a certain peak value V_p may be applied to the crystal, the phase retardation produced in the light pulse (section 4.2) is less than that which would have been caused by a static voltage V_p. The following analysis will show at which frequencies this becomes important.

From equation 4.3, the retardation produced in a crystal of length l due to a steady field E is

$$\Gamma = Eal \tag{5.1}$$

where $$a = \frac{\omega n_o^3 r_{63}}{c}$$

However, if E changes during the transit time of the crystal $\tau (\simeq n_o l/c$) then equation 5.1 must be rewritten as

$$\Gamma(t) = \frac{ac}{n_o}\int_{t-\tau}^{t} E(t')\,dt' \tag{5.2}$$

where E(t') is the instantaneous field, taken as constant throughout the crystal, and the integral refers to a wave which enters the crystal at a time $t - \tau$ and emerges at t.

If E(t') varies sinusoidally, the frequency of this function ν_m at which the peak retardation is reduced to 90% of its unmodulated value is given by (93)

$$\nu_m = \frac{c}{4ln_o} \tag{5.3}$$

For a crystal of KDP or KD*P with an active length of 2cm ($n \simeq 1.5$), then $\nu_m = 2.5 \times 10^9$ Hz. If the length is reduced to 1cm, then ν_m becomes 5×10^9 Hz. A GaAs switch can supply pulses of less than 150ps duration and therefore the problem of crystal transit time may be of substantial importance.

The limiting pulse duration which can be obtained with a modulator of this form is set by the size of the Pockels cell clear aperture, since the voltage wave which sets up the field within the crystal must take a finite time to cross the aperture. The crystal can be considered as the insulating part of a transmission line with its electrodes forming the conductors. The

speed of an electric wave travelling down this line can be calculated and provides a limit to the risetime of the optical modulator. Commercially, the fastest Pockels cell available[94] has a 2.5 mm clear aperture and a risetime of 50 ps, limited by the aperture of the KD*P crystal used.

For the 12.5 mm aperture, 25 mm long crystal of Chapter 4, a 250 ps risetime should therefore be the theoretical limit, if the inductance of the driving circuit could be substantially decreased. Section 5.3 will describe an investigation to study this.

5.3 Low inductance driving of a KDP electrooptic crystal

The following experiments were carried out on a complete KDP crystal extracted from a Pockels cell. Its dimensions were 17.5 x 17.5 mm^2 (polished parallel faces) x 24.5 mm. Although KDP is less electrooptically active than KD*P, it was more readily available as a complete undamaged crystal and was perfectly adequate for preliminary experiments. Without the protection of the phase matching solution, the faces of the KDP crystal deteriorated with time as they were attacked by moisture in the atmosphere. This was slowed by shining a lamp on the crystal to keep the surrounding air warm, but it was necessary to repolish the crystal after several weeks. Since the gold ring electrodes of the original cell were removed to allow the crystal to be polished, and since this occurred regularly, it was necessary to use a much cheaper and simpler electrode arrangement. Aluminium foil with a 5 mm diameter circular aperture was therefore placed across the whole crystal face and attached with an impact adhesive ("Evostik"). This proved satisfactory and could be improved in a more permanent modulator.

5.3.1 The crystal as a section of a 50 Ω transmission line

The impedance of a parallel plate transmission line, of conductor width b and separated by a dielectric of thickness a, in the case where edge effects are negligible (a << b), is given by

$$Z_0 = \frac{a}{b \epsilon_r^{1/2} \epsilon_0 c} \qquad (5.4)$$

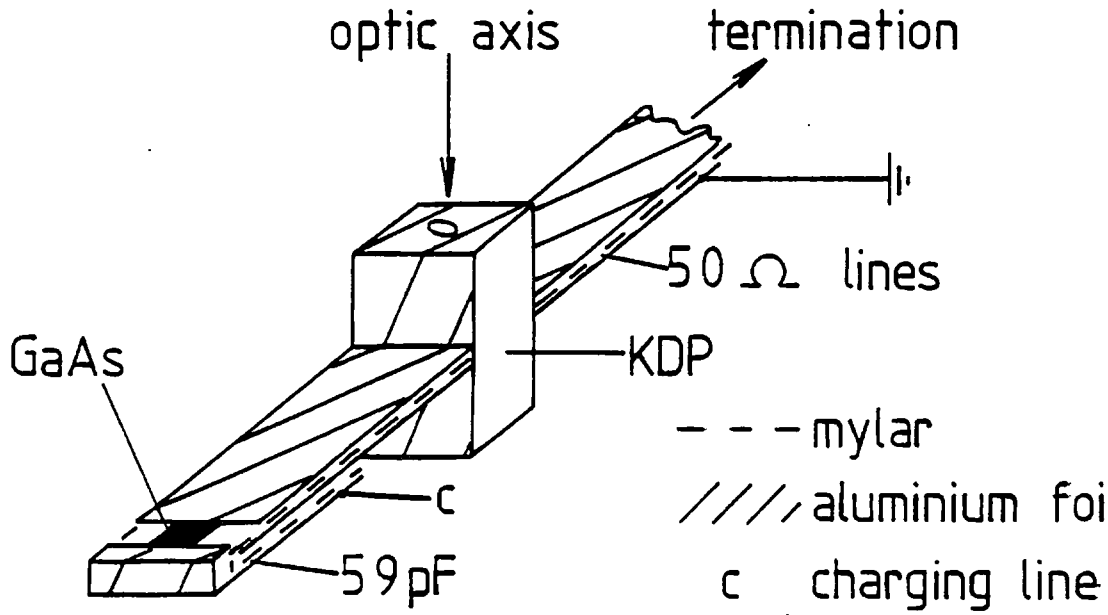
where ϵ_r is the dielectric constant. If the condition a << b does not apply, this must be rewritten as

$$Z_0 = \frac{k a}{b \epsilon_r^{1/2} \epsilon_0 c} \qquad (5.5)$$

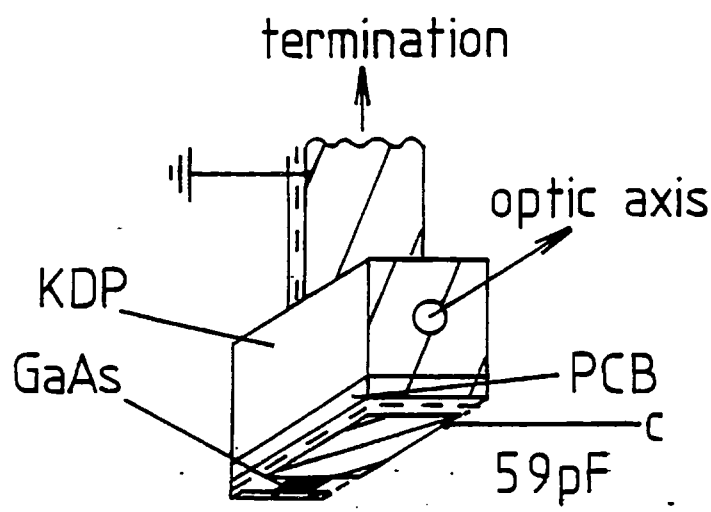
where k is a constant which is a function of the ratio a/b. To set up a field within the KDP crystal, a voltage wave must propagate across the aperture, i.e. along the transmission line formed by the electrodes and the KDP crystal and orthogonal to the crystal (z-)axis. For this line $\epsilon_r = 20$[95] and a/b = 1.43, which implies a value of k = 0.41[96]. Hence the impedance of the line is Z_o = 49 Ω (equation 5.5), if the effect of the 5 mm aperture is ignored.

The arrangement of figure 42(a) was constructed to incorporate the crystal into a 50 Ω transmission line and drive it from a GaAs switch. Theoretically, a voltage pulse generated from the switch would efficiently sweep across the crystal aperture and provide equally rapid light modulation. The approximately 50 Ω line leading to the crystal was constructed from layers of 0.25 mm thick mylar and impact adhesive with two parallel plate, 17.5 mm wide, aluminium electrodes. The energy for each pulse was supplied by a 59 pF low inductance capacitor. This

Figure 42



(a) transmission line



(b) direct discharge

Low inductance driving of KDP

was formed from two 17.5 x 17.5 mm^2 aluminium electrodes separated by 0.125 mm of mylar. A 4.7 nF capacitor recharged the 59 pF capacitor between dye laser pulses and itself had enough energy storage to not be significantly depleted by the whole pulse train. The second half of the 50Ω line, leading away from the crystal, was terminated with either a resistor or a 50Ω input impedance oscilloscope. The oscilloscope showed that pulses of comparable magnitude to those monitored directly from the GaAs switch were propagating across the KDP crystal without significant reflection or attenuation.

This arrangement was further improved (figure 42(b)) by removing the possibly dispersive 50Ω charging line and discharging the 59 pF capacitor directly through the switch and on to the KDP crystal. The crystal, driven as in figure 42(b), was placed between crossed polarizers and probed with the XeCl laser, as in Chapter 4. When the switch was illuminated a train of UV pulses, which were oscilloscope limited in duration, was observed with a peak intensity which was approximately an order of magnitude lower than the longer pulses switched with the commercial Pockels cell of Chapter 4 (figure 40). Although the integrating effect of the oscilloscope makes this a somewhat pessimistic figure, and allowing for the fact that these results were for KDP rather than the more electrooptically active KD*P, the peak efficiency of the modulator was poorer than before. Therefore, although the problem of applying rapid voltage pulses to the crystal electrodes appeared to have been solved, the limitations of crystal length and aperture described in section 5.2 were restricting the efficiency of light pulse generation. Section 5.4 will discuss the specific crystal and electrode structure which was designed to improve this situation. First, however,

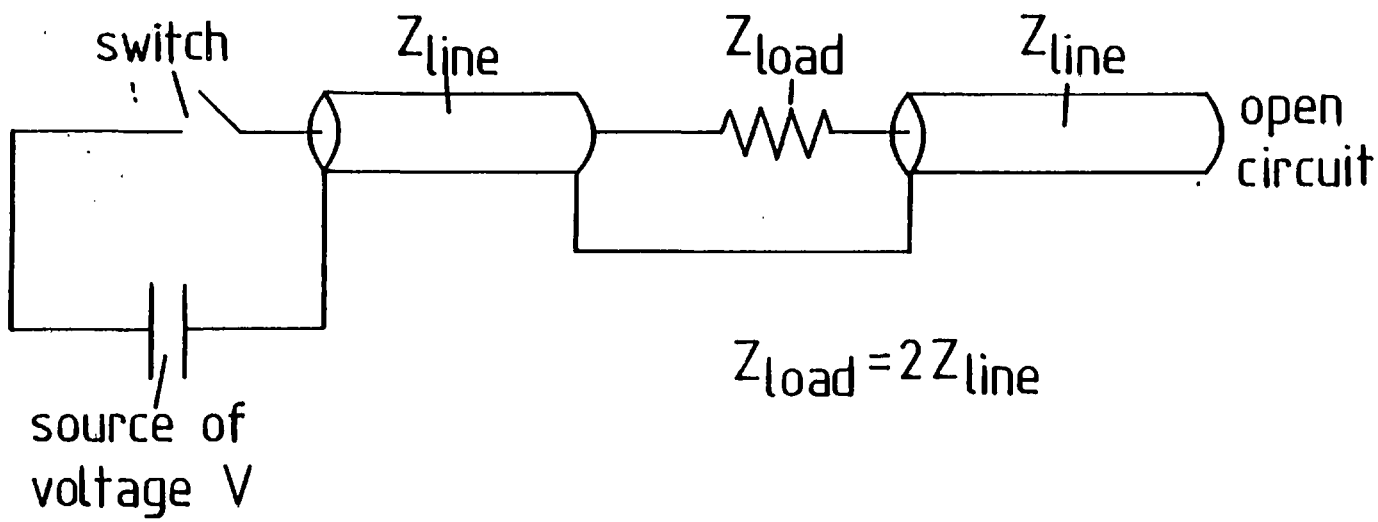
some preliminary results obtained with the KDP crystal as the load of a Blumlein line will be described.

5.3.2 The crystal as the load of a Blumlein pulse forming line

In the modulator of Chapter 4 only half of the GaAs switch charging voltage could ever be developed across a matched load, even under optimum conditions. Putting the crystal across the load of a Blumlein pulse forming line, in a low inductance configuration, could allow the full charging voltage to be developed across the crystal in a pulse of controllable duration.

This situation is analogous to the pulse forming of the high voltage output of a pulsed power supply. A single pulse forming line (the charging line of the GaAs switch of Chapter 4) with a matched load must be charged to twice the voltage required at the load. The Blumlein line was developed to allow the full voltage to appear across the load. Figure 43 shows schematically a Blumlein pulse forming line[97],[98]. When the switch closes, a step of magnitude V is transmitted down the line towards the load. If the load and lines are matched ($Z_{line} = Z_{load}/2$), the pulse is split into two at the load, V/2 which is reflected and 3V/2, which is transmitted. The transmitted portion is itself divided into V across the load, and V/2 transmitted into the second half of the line. Both V/2 edges travel up and down equal lengths of line and return simultaneously to the load, but the component reflected from the closed circuit suffers a π phase change, becoming -V/2. The two edges of opposite polarity cancel at the load, reducing the load voltage to zero. A pulse of magnitude V therefore appears across the load with a duration of Δt, where

Figure 43



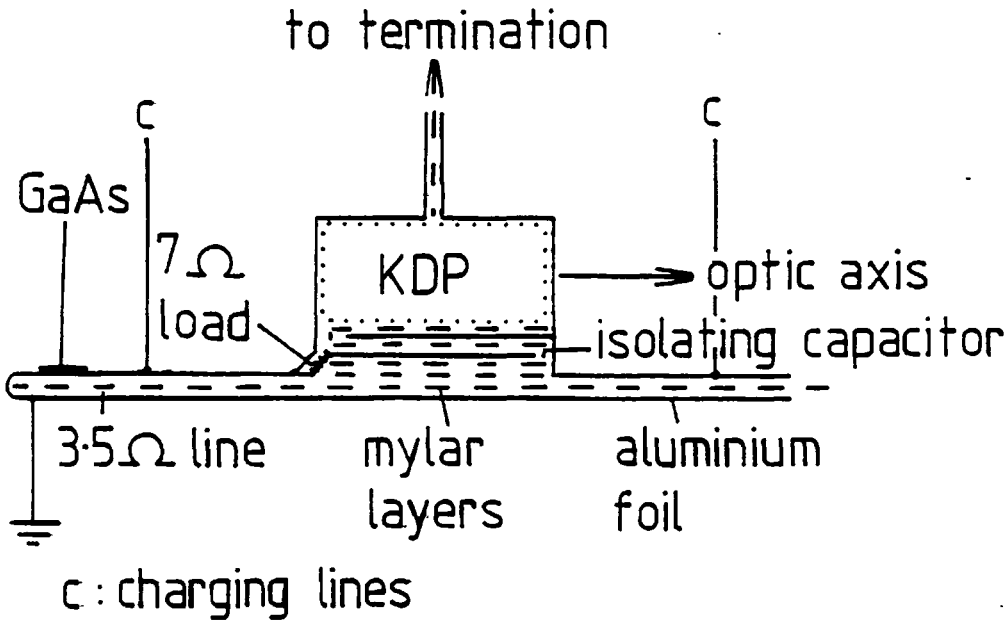
A Blumlein pulse forming line

$$\Delta t \simeq \frac{2 \times \epsilon_r^{1/2}}{c} \qquad (5.6)$$

x is the physical length of each branch of the line (figure 43), and ϵ_r is the dielectric constant of the insulating material between the conductors.

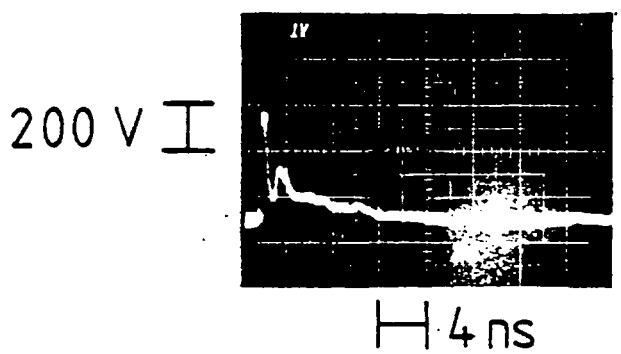
A Blumlein line was constructed to drive the KDP crystal (figure 44). Section 5.3.1 showed that the characteristic impedance of the transmission line formed with the KDP crystal as the dielectric was 49Ω. Since this impedance was to be placed across the load of the Blumlein line it was necessary for it to be large compared to the load, which was itself twice the characteristic impedance of the branches of the Blumlein line. 17.5 mm wide strips of aluminium foil attached with impact adhesive to either side of a piece of 0.25 mm thick mylar formed a line of characteristic impedance $\simeq 3.5\Omega$ - small compared to 50Ω, and with a width matching the crystal width (assuming ϵ_r 2.7 for mylar[99]). A 7Ω resistor and a capacitor formed the load of the Blumlein line. The capacitor was constructed from 0.025 mm thick mylar with plane parallel aluminium electrodes and had a capacitance of $\simeq$ 300 pF, to allow the two arms of the Blumlein line to be charged differentially if a bias voltage across the crystal was required. The low inductance, small value resistor was formed by immersing carbon fibres in "Simplex" acrylic resin (Howmedica Ltd.), to provide strength, and then cutting the resultant solid resistor until the required resistance was obtained. Electrical connection was made between the various components with conducting paint. These precautions were necessary to allow the efficient low inductance operation of the Blumlein line at

Figure 44



A KDP crystal as the load of a Blumlein line

Figure 45



Voltage appearring across the load of the Blumlein line

the frequencies under consideration. From equation 5.6, the pulse duration which would be derived from this line was 200 ps.

A low inductance, 50Ω monitor replaced the KDP crystal in preliminary tests. Single shot operation was achieved by mechanically shorting out the GaAs switch with the head of a screwdriver. With the line charged to 1.5 kV the output of figure 45 was generated. The peak height observed of 470 V was lower than the charging voltage because the expected 200 ps pulse width was much shorter than the oscilloscope risetime ($\gtrsim$ 0.7 ns, Tektronix 7834) and the values of the attenuators used were uncertain at this frequency.

The successful single-shot operation of this device has been shown. In order for it to be useful in the repetitive generation of pulses, a semiconductor switch illuminated by a dye laser must be used. The switch would need to have an impedance, immediately after illumination, small compared to 3.5Ω, which stayed at a low value for several hundred pico-seconds to ensure the successful operation of the Blumlein line. The switch would then have to recover its dark impedance in the $\simeq$ 8 ns before the arrival of the next dye laser light pulse. These properties could not be achieved with GaAs switches (section 4.3). Similarly, the other commonly used semiconductor, S_i, has the problem of a too long recombination time of 20 μs[100].

To conclude, a simple method for the efficient generation of very short voltage pulses with a controllable duration has been demonstrated. However, the available semiconductor materials were such that this method could not easily be used for the generation of pulses at the required repetition rate. The search for a faster electrooptic modulator therefore turned

back to the considerations of section 5.3.1 and the question of electrooptic crystal design and electrode structure.

5.4 Construction of an improved electrooptic modulator

5.4.1 The crystal and electrodes

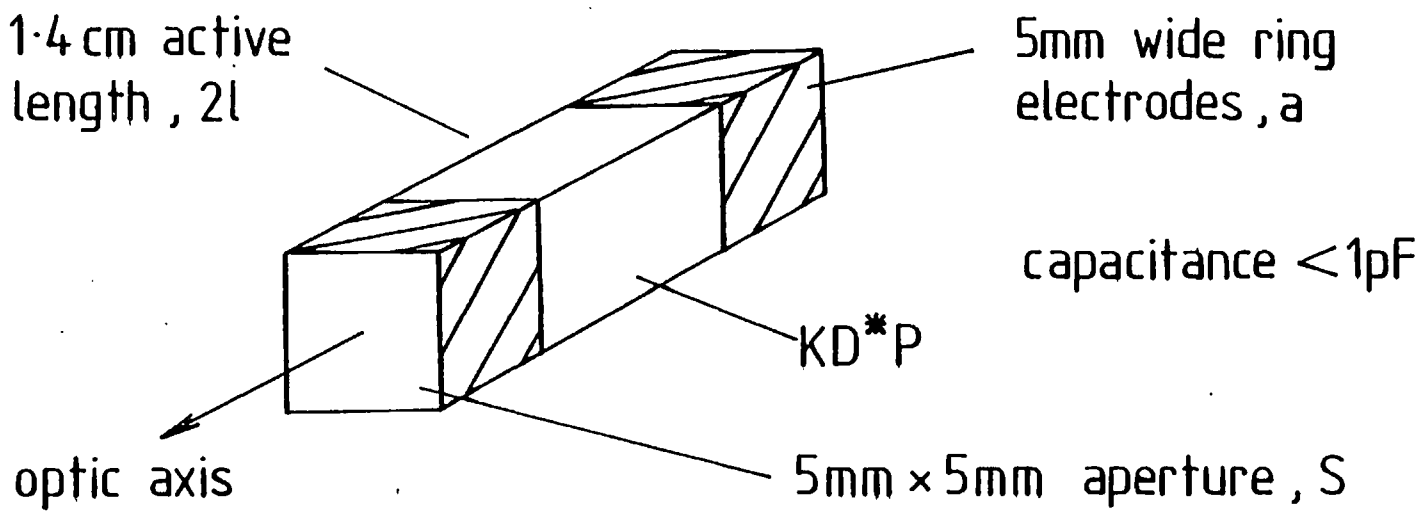
A 5 mm x 5 mm crystal aperture was chosen, which gave a limiting risetime for the optical pulse of $\lesssim$ 100 ps (for KD*P). This was short enough to be of the order of the GaAs switch conduction period. Similarly, the active length of the crystal was reduced to allow a greater electric field to be developed in the crystal, and therefore more phase retardation in the limited period of voltage application. An active length of 1.4 cm gave a light transit time of 70 ps. The final crystal design is shown in figure 46. Strip electrodes were chosen for a number of advantages they have over the conventional ring electrodes so far used. First, they have a higher transmission uniformity across the cell aperture, although preferably for a cylindrical crystal, and allow the whole crystal face to form the aperture[101]. Second, they are known to have a subnanosecond switching capability[102].

The capacitance of the crystal and electrodes is an indication of the expected risetime. In this case the capacitance is given by (103)

$$C = \frac{S \epsilon_r \epsilon_0}{2(l - a)} \qquad (5.7)$$

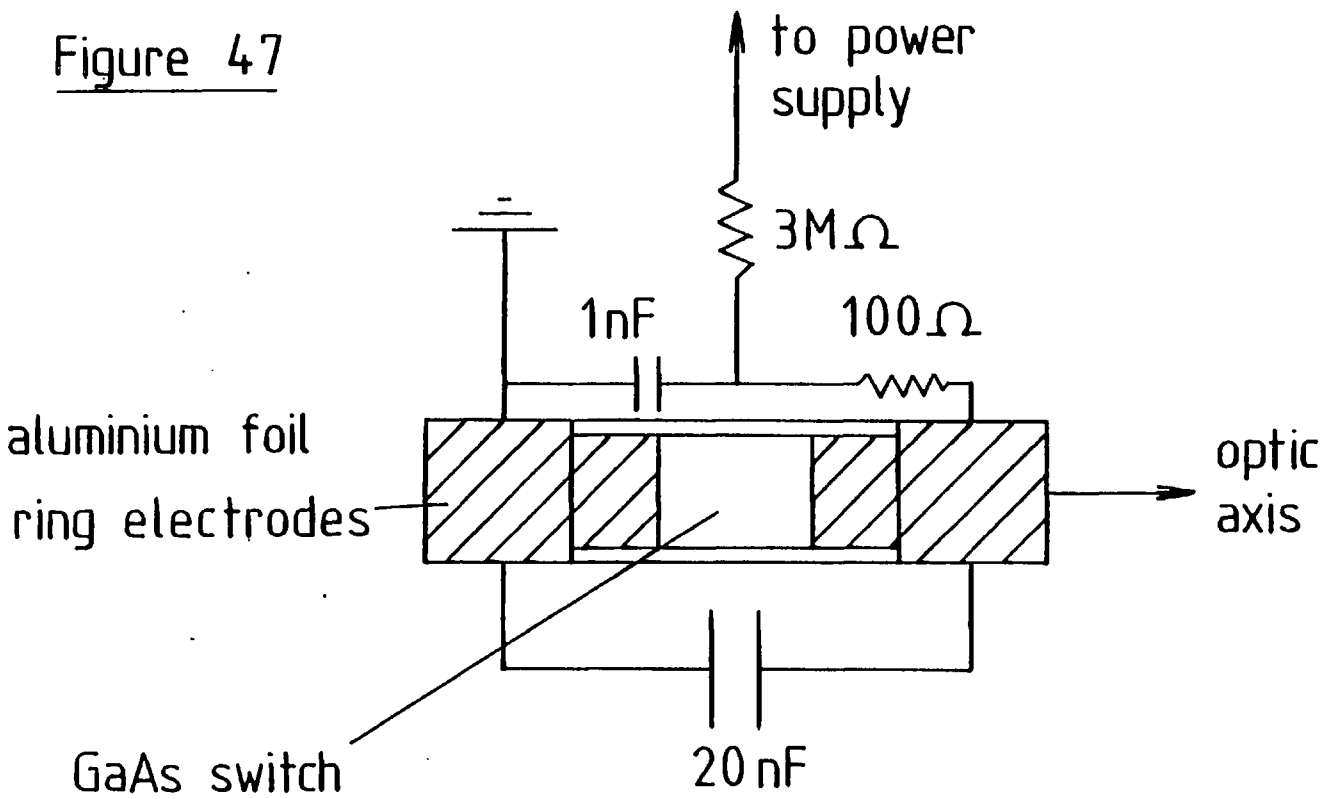
which, for the dimensions of figure 46, implies a value of $C \simeq 0.8$ pF compared with a typical commercial Pockels cell value of 5 pF.

Figure 46



The redesigned crystal and electrodes

Figure 47



Schematic diagram of the crystal and charging circuit

The crystal was cut from a larger piece of damaged KD*P which had been incorporated in a Pockels cell. The electrodes were 5 mm wide strips of aluminium foil attached with contact adhesive to the sides of the crystal.

5.4.2 The driving circuit

The driving circuit of figure 47 differed from that used for the larger crystal in that, instead of charging the crystal with a short voltage pulse, it was to be kept charged and then discharged for a short period. As the GaAs switch was illuminated, the crystal capacitance would discharge through it. The carriers in the switch would then recombine following the short light pulse, and the crystal would again charge up through the 100 Ω resistor from a 1 nF capacitor. The 1 nF disc ceramic capacitor and 100 Ω carbon composite resistor were kept as close to the crystal as possible to minimise the circuit inductance. A further 20 nF capacitor was added, as shown, to recharge the 1 nF capacitor between pulses of light from the dye laser. Without this, the 1 nF capacitor had insufficient storage to sustain the original charging voltage as it was gradually drained of energy by successive dye laser light pulses. The 20 nF capacitor was connected in a slight loop, such that it did not affect the crystal voltages on the time-scale of operation of the switch. Finally, the 20 nF capacitor was itself charged through an isolating 3 MΩ resistor by a stabilised power supply. Figure 48 is a plate of the final mounted modulator.

5.5 Performance of the modulator

5.5.1 Experimental results

The new crystal was placed in the modulator of figure 33, but in this case the transmission axes of the polarizers were aligned parallel to one another by crossing them both with

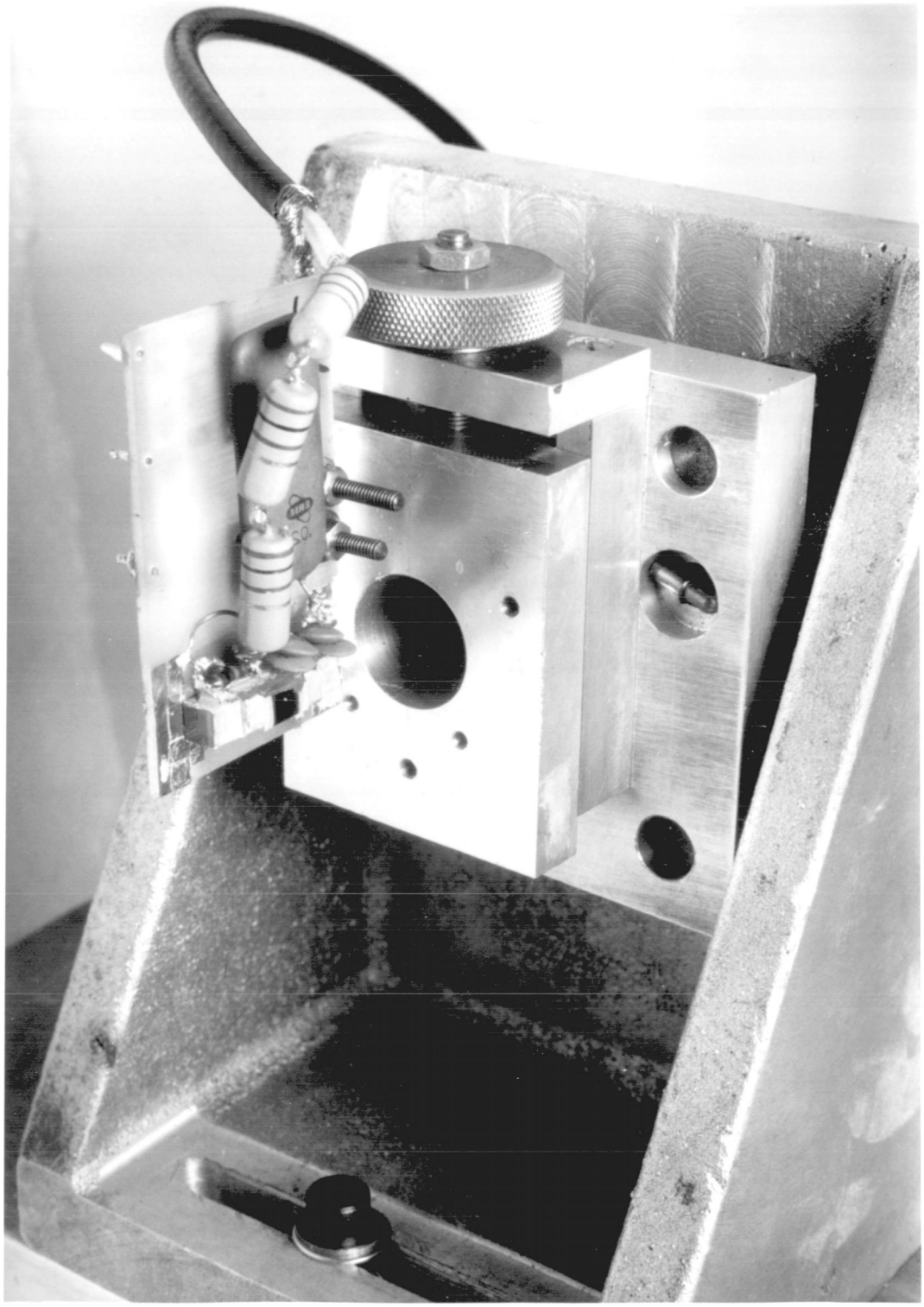


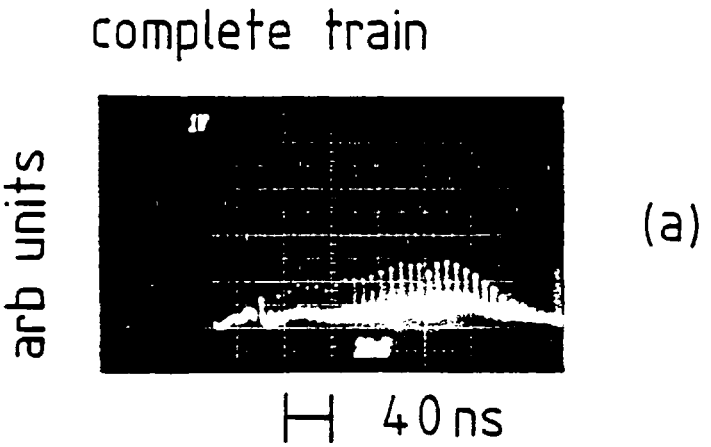
Figure 48 (plate) The redesigned modulator

respect to a third, and the half-wave voltage was found by applying a bias to the crystal and monitoring the background level of light leaking through the modulator. This produced a value of V_{π} = 2.2 kV when the light intensity transmitted was a minimum (at 308 nm). With the crystal charged to 2.2 kV the switch was activated by the dye laser in synchronism with the probe XeCl laser, as before, and the photodiode trace of figure 49(a) was obtained.

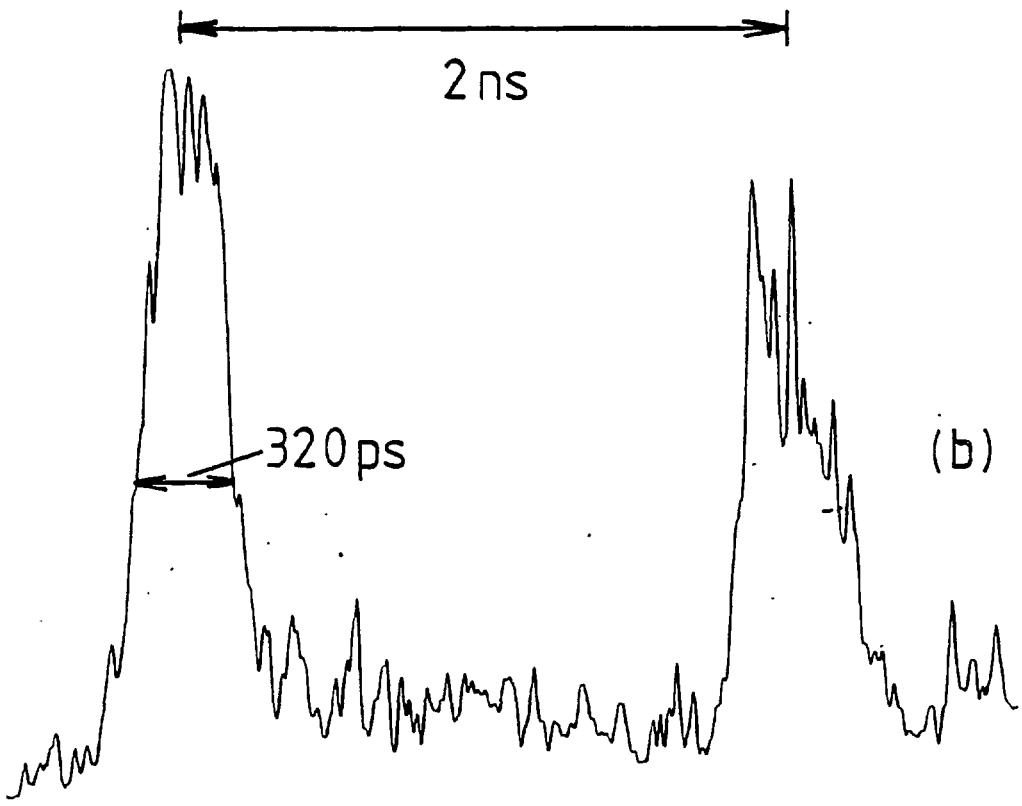
An electrooptic streak camera was used to measure the duration of the pulses switched out by the modulator. In a streak camera (figure 50) the photons incident on a photocathode generate electrons which are rapidly accelerated by an adjacent high voltage mesh. The beam of electrons is then swept electrostatically by a ramp voltage applied across the deflection plates. This process converts the temporal information of the original light pulse into spatial information which is more convenient for analysis. The image appearing at the phosphor is then intensified with an image intensifier to allow photographic recording.

A Photocron II streak camera with a S-20 UV-photocathode[104], [105] which had a sapphire substrate and windows to allow operation into the UV was used. The experimental arrangement for streaking the pulses is shown in figure 50. A fraction of the beam was projected via a UV filter and a piece of diffusing quartz onto the slit of the streak camera before being imaged onto the photocathode with UV optics. The majority (> 90%) of the beam fell unattenuated onto a UV photodiode, the signal from which triggered a Tektronix 519 oscilloscope, whose 10V gate output was then used to trigger the krytron circuit, which provided the ramp voltage for the deflection plates. Various integrators placed in series with the ramp voltage generator

Figure 49

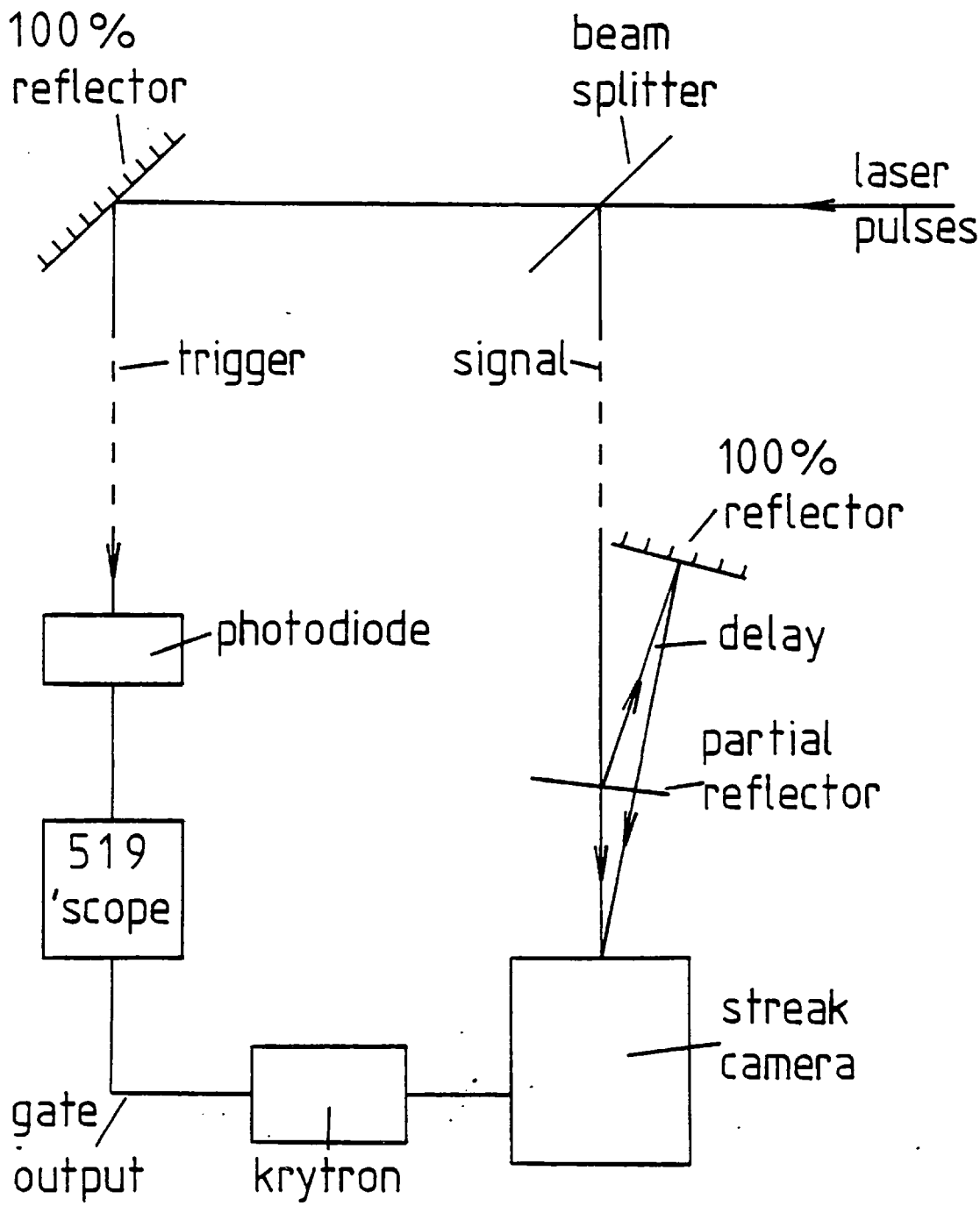


microdensitometer trace of streaks obtained (a single pulse split by the delay line)



Modulated output of the XeCl laser

Figure 50



Schematic streak camera arrangement

were available to control the streak speed.

A 0.5 - 1.0 ns optical delay line provided a double pulse with a known separation for the purposes of calibration. A relatively slow sweep speed of $\simeq 3 \times 10^6$ ms^{-1} with a resolution of a few tens of picoseconds gave a 12 ns sweep duration, which ensured that if a pair of pulses struck the camera slit they were recorded (pair separation 8 ns). A total delay of 60 - 70 ns occurred between the beginning of the XeCl laser pulse train and the camera sweep, so pulses towards the centre of the train were being recorded. There were no problems of jitter on this timescale.

Many experimental difficulties were encountered in recording the pulses. Streak cameras had not previously been used in association with electron beam generators, and the noise problems were not unexpected. The krytron would fire prematurely unless the camera was kept several metres from the laser, and careful attention was paid to shielding, earth connections and the avoidance of mains spikes. The photodiode head was found to be especially sensitive to noise and was often the source of the early triggering of the oscilloscope and krytron.

At the streak camera slit, 5 m from the laser, the position of the light output from the laser varied spatially over several centimetres between shots and only illuminated the slit infrequently. Apparently the laser mirrors were physically changing their orientation slightly each time the electron beam generator was fired. The problem was solved by mounting the mirrors on optical benches out of contact with the pulsed power supply.

Finally, to align the streak camera and produce reproducible streaks, first on polaroid and then on cut film, it was necessary

that the XeCl laser, dye laser and modulator worked reliably for perhaps 100 shots in a single run. This was not easy to achieve - over 100 shots the dye laser output could deteriorate, or a switch might fail, or the electron beam generator could become more noisy as the quality of e-beam emission became poorer (covering the switch in clear epoxy resin protected the switches in later work).

Successful streaks were eventually obtained from the camera and recorded on Kodak 35mm HP5 film. A microdensitometer scan of a pulse pair is shown in figure 49(b). Calibration (step) wedges recorded on the same film allowed both the F.W.H.M. duration of the pulses and the level of background to be found. Pulse widths (deconvolved) of 300 ps with a 10% shot-to-shot variability were obtained with a modulation depth of greater than 80%. The results were found for a 2.5 mm circular beam apertured at the modulator crystal.

5.5.2 Analysis of results

The peak light intensity in the pulses was $\gtrsim$ 30% of that transmitted by the uncharged crystal, estimated from streak camera and photodiode traces and assuming linearity of photodiode response over a factor of three change in light intensity.

A 300 ps pulse is somewhat more than could ideally be obtained from a 2.5 mm aperture crystal. The most important factor in this is the inductance of the 1 nF - 100Ω circuit recharging the crystal which increases the voltage risetime. At the frequencies under consideration, the inductance associated with the 1 nF disc ceramic capacitor and the $\simeq$ 1 cm length of 1 mm diameter wire making up the charging circuit is $\simeq$ 10 nH[92]. A Laplace transform analysis of the equivalent circuit of figure

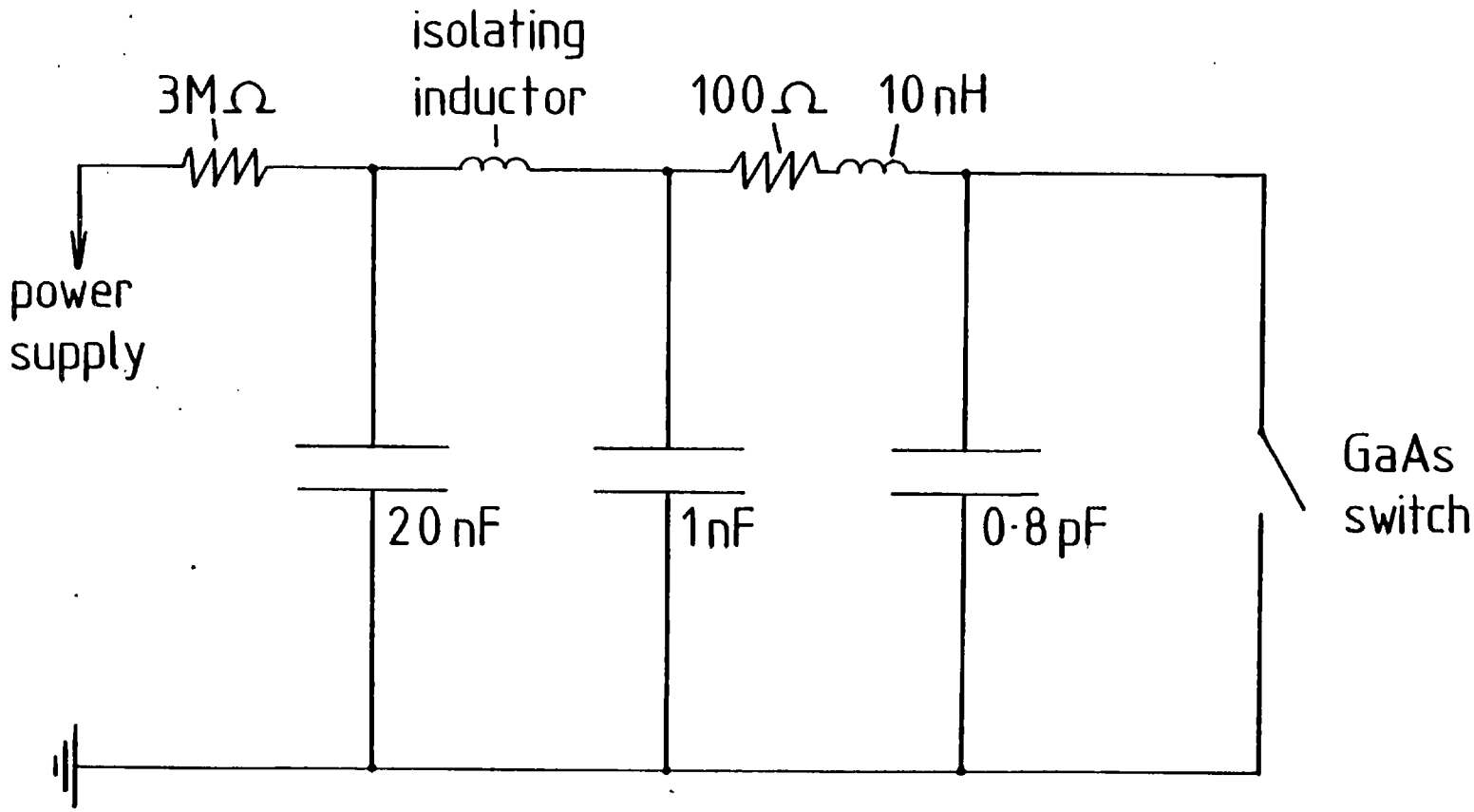
51 can therefore be carried out, with the crystal modelled as a 0.8 pF capacitor. If the crystal begins to recharge from t = 0 and its voltage is v(t), then

$$v(t) = \frac{C_2 V_0}{C_1 + C_2}\left[\frac{m_2 \exp(m_1 t)}{m_1 - m_2} - \frac{m_1 \exp(m_2 t)}{m_1 - m_2} + 1\right] \qquad (5.8)$$

where $$m_1, m_2 = -\frac{R}{2L} \pm \sqrt{\frac{R^2}{4L^2} - \frac{C_1 + C_2}{LC_1C_2}}$$

and V_o is the voltage on the 1 nF capacitor at t = 0. For the component values of figure 51 the e-fold risetime of the voltage across the crystal is therefore $\simeq$ 180 ps. This agrees reasonably well with the pulse shapes observed from the streak camera, and again shows the importance of minimising circuit inductances at these frequencies.

An aperture was introduced to remove the light traversing the crystal near the electrodes, where non-uniformities of transmission were observed to be greatest. This allowed a modulation depth of 80% to be achieved. The background light was mainly produced due to non-uniformities of the applied electric field - a square electrode geometry was not ideal, and a cylindrical one would have been preferable, but difficult to fabricate. Also, some investigation could have been made of the improvements which might be made with alternative foil materials and the cement used to bond them to the crystal. Two final contributions to the background were a slight birefringence which existed even in the uncharged crystal, and observed with the HeNe alignment laser, and the difficulty of accurately aligning the polarizers



Circuit to model the electrical behaviour of the modulator

Figure 51

and crystal with respect to one another.

5.5.3 Summary and improvements

A very fast high repetition rate Pockels cell has been developed. Allowing for the complexity of the dye laser, the modulator itself is extremely cheap, simple to fabricate and very reliable. Although unnecessary for active mode-locking (see Chapter 6), the duration of the switched pulses could be reduced to perhaps 150 ps, with a subsequent loss of efficiency, by minimising the already small circuit inductances. Only standard electrical components have been used so far - the resistor could be replaced by a graphite felt-in-Simplex alternative, and the capacitor by foil and mylar. Connected by foil instead of thin wires, this would be a substantial improvement. The modulator could be repetitively operated at up to 3-4 GHz.

Faster switching with a reasonable efficiency can only be achieved by bypassing the transit time problems of section 5.2. One method which can in principle do this involves applying the modulating voltage signal in the form of a travelling wave propagating in the same direction as the light beam. This is known as transverse modulation, the applied electric field being perpendicular to the direction of travel of light, as opposed to the longitudinal effect exclusively considered so far. If the optical and modulation voltage phase velocities are equal to one another, then a portion of an optical wavefront will experience the same instantaneous modulating electric field, which corresponds to the field it encountered at the entrance face, as it propagates through the crystal. The transit time problem is therefore eliminated. Matching of phase velocities is not, however, a trivial problem[106],[107],[108], and cannot

be achieved in a simple structure. While the fast optical switch of Le Fur and Auston[84] does use the transverse electro-optic effect, the electrical wave still travels in a direction perpendicular to the light.

Finally, it seems most likely that the behaviour of semiconductor switches will be characterised most accurately in experiments such as these, where the switched voltage can be related to a measurable light pulse[84],[88]. By considering the duration and magnitude of the pulse generated as the illumination intensity at a switch is varied, effects such as switch saturation, efficiency of operation[87] and the importance of contact resistances should be more directly observable.

CHAPTER 6

MODE-LOCKING OF EXCIMER LASERS

6.1 Introduction

The output of a longitudinally mode-locked laser takes the form of a series of intense, short duration pulses. This chapter will consider the extension of various mode-locking techniques to the electron beam sustained discharge XeCl laser. It will describe the results achieved actively with the electro-optic modulators of Chapters 4 and 5, and will discuss the problems of passively mode-locking such systems.

The output of a laser is dependent on the amplitude, frequency and phase of the longitudinal modes which are allowed to resonate. A simplified analysis can indicate the effect of the coupling of these modes together. The (angular) frequency separation ω of successive modes of a resonator of length L is given by

$$\omega_{q+1} - \omega_q = \omega = \frac{\pi c}{L} \qquad (6.1)$$

(assuming unit refractive index, and where c is the velocity of light). The total optical electric field resulting from multimode oscillation, at an arbitrary point within the resonator, is therefore given by, using complex notation,

$$E(t) = \sum_n E_n \exp\left[i\left((\omega_0 + n\omega)t + \phi_n\right)\right] \qquad (6.2)$$

where the summation is over the oscillating modes n and ω_o is a reference frequency, ϕ_n is the phase of the nth mode. In a typical laser, ϕ_n varies randomly with time. Mode-locking occurs

when the phases ϕ_n are locked together, for example at zero. In this case, assuming $E_n = 1$ for simplicity,

$$E(t) = \sum_{-\frac{(N-1)}{2}}^{\frac{(N-1)}{2}} \exp[i(\omega_0 + n\omega)t] \tag{6.3}$$

$$= \exp(i\omega_0 t)\frac{\sin(N\omega t/2)}{\sin(\omega t/2)} \tag{6.4}$$

for N oscillating modes. Hence the laser power output is given by

$$P(t) \propto \frac{\sin^2(N\omega t/2)}{\sin^2(\omega t/2)} \tag{6.5}$$

Equation (6.5) implies that the laser power is emitted in the form of a train of pulses with a period $t_R = 2\pi/\omega = 2L/c$. The individual pulse width is $t_p = \tau/N$, or, if $\Delta\nu$ is the gain linewidth,

$$t_p \simeq \frac{1}{\Delta\nu} \tag{6.6}$$

For an excimer laser, this bandwidth limit for the obtainable pulse duration is < 1 ps[109]. Where mode-locking is not complete as is the case in the experiments to be described in this chapter, the pulse duration is somewhat longer than this.

This analysis is only strictly applicable to an inhomogeneously broadened laser system where, in the absence of any loss modulation, many modes are allowed to oscillate. In the case of a homogeneously broadened excimer laser only one mode can normally oscillate. However, in the presence of internal modulation, power is transferred continuously from the high gain

mode to those of lower gain[110]. This is equivalent to the generation of sidebands at ($\omega_o \pm n\omega$) of the mode at ω_o created by modulation at ω. The net result is that of a large number of oscillating modes with equal frequency spacing and fixed phases, as in the inhomogeneous case, leading to ultrashort pulses.

Sections 6.2 and 6.3 will describe the active and passive techniques of producing mode-locking, and their success when applied to the XeCl laser.

6.2 Active mode-locking

6.2.1 Introduction

Chapter 4 introduced the concept of active mode-locking, when an optical modulator placed inside a laser cavity is driven at a frequency near the laser cavity roundtrip frequency. The analysis of the mode-locking of continuous and pulsed lasers has been reviewed for the case of electrooptic or acoutooptic modulators driven by a sinusoidal signal[111]. The decrease in pulse width with number of passes around the laser cavity for both a Q-switched Nd:YAG laser and a CO_2 TEA laser was considered. Typically it was found that the time required for a pulse to reach its steady state value was more than an order of magnitude greater than the period of laser action ($\lesssim$ 1 μs). These results, which did not consider the effects of gain saturation on the pulse shape, imply that this form of modulation cannot be expected to generate ultrashort pulses from simple discharge pumped lasers. This is borne out by the active mode-locking of a discharge pumped XeF laser with an acouto-optic modulator carried out by Christensen et al[75]. Less than five pulses were obtained, of $\simeq$ 2 ns duration in a 15 ns train, with a

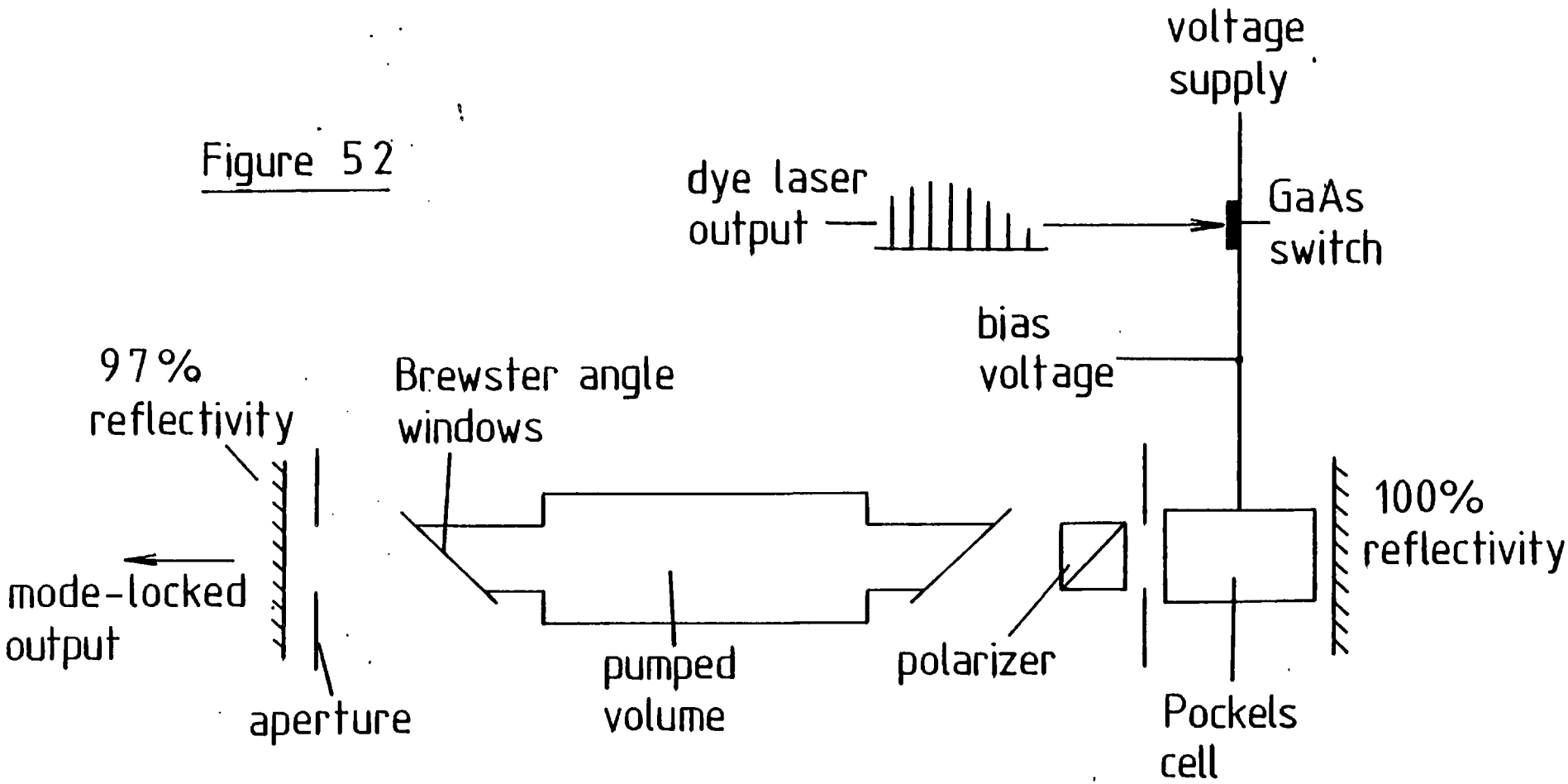
modulation depth of 70% - and it was predicted that a gain duration of several microseconds would be required to achieve pulse lengths of $\simeq$ 100 ps[112]. The advantage of fast, efficient modulators for excimer lasers is therefore that they encourage the generation of short pulses which would otherwise require microseconds to build up with conventional modulators. The modulator of Chapter 4 has been shown to be capable of mode-locking a discharge pumped XeCl laser, producing a 100% modulated train of pulses with durations as short as 310 ps[78]. This section will consider the active mode-locking of the long pulse XeCl laser with both this modulator and the much faster modulator described in Chapter 5.

6.2.2. Active mode-locking with a commercial Pockels cell

Figure 52 is a schematic diagram of the arrangement employed to actively mode-lock the laser. As usual, the laser was run in the standard operational mode, described in Chapter 3, for reliable, low maintenance performance. A cavity was formed around the discharge chamber and modulator by a 100% reflectivity silvered and a > 97% multilayer dielectric mirror. The low output coupling was necessary to allow laser operation through the relatively lossy Pockels cell. The modulator was aligned by replacing the silvered mirror by a second polarizer, crossed with respect to the first, and using the "Maltese Cross" method. This second polarizer was then replaced by the reflector

With the Pockels cell driven from the circuit of figure 39, a steady bias was first applied to the cell, and the voltage found where laser action was reduced to a minimum. This was 700V, and the light passing through the first polarizer, and being polarized by it, was undergoing a 90° rotation in its plane of polarization, or a π phase retardation between its two

Figure 52



Active mode-locking with a commercial Pockels cell

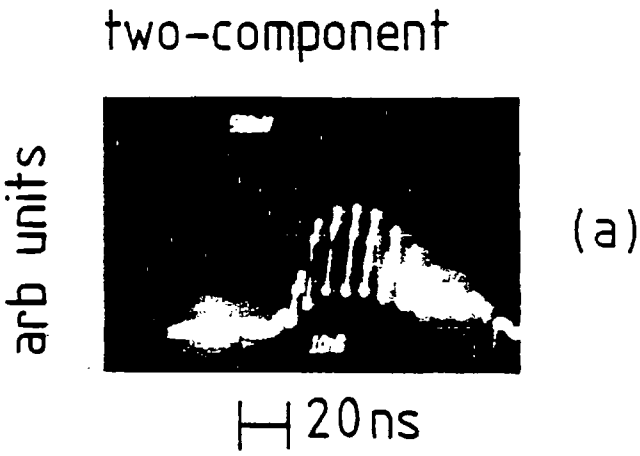
components, on passing twice through the Pockels cell before being rejected by the polarizer (i.e. 700V = V_{π} /2). Laser action could not therefore begin.

To mode-lock the XeCl laser, it was necessary to apply voltage pulses at the round trip frequency of this laser to the Pockels cell biased at 700V. The dye laser cavity length was therefore first set to be roughly equal to that of the excimer laser such that its pulses would strike the GaAs switch at the required frequency. Ideally, the voltage across the Pockels cell should be raised by the pulses from the switch to V_{π} or 1.4 kV. In this case, light would undergo a 180° rotation in its plane of polarization on passing through the cell twice and be efficiently coupled back into the discharge cavity by the polarizer. Practically (Chapter 4), however, only $\simeq$ 100V was added from the switch, with a subsequent reduction in efficiency.

A bias voltage of 700V was applied to the Pockels cell and the GaAs switch charged to 3-3.5kV. The XeCl and dye lasers were fired in synchronism and typical and optimised output trains from the XeCl laser, recorded with a photodiode-Tektronix 7834 oscilloscope combination, are shown in figure 53. To obtain reasonably "clean" pulses, it was necessary to match the cavity lengths to within ± 5 mm, corresponding to a time difference after 10 roundtrips of 330 ps. Laser action occurred for only $\simeq$100 ns due to modulator losses.

In the position of best alignment for the Pockels cell, for most efficient electrooptic modulation, its windows were parallel to the laser mirrors, and laser action could build up between the cell entrance face and the 97% reflectivity mirror. In consequence, the pulse train was developed upon a continuous unmodulated background. To remove the background, the Pockels

Figure 53



Output of the actively mode-locked XeCl laser (Pockels cell)

cell was gradually misaligned until the 100% modulation depth of figure 53(b) was achieved. Further misalignment was necessary to produce pulses without the double pulse structure of figure 53(a).

In order to explain this structure, consider a pulse of light approaching the modulator from the gain region. None of this is coupled back from the polarizer, which has a large acceptance angle allowing it to be considerably misaligned. However, a part of the 4% reflected from the front window of the slightly misaligned cell is transmitted back down the cavity. Due to the inefficiency of the modulator (Chapter 4) only a small fraction of the light passing through it returns back through the polarizer and into the discharge cavity. If the effect of the switch is to add $\simeq$ 100V to the 700V bias, this fraction is $\simeq$ 5% (neglecting losses) from equation 4.6. Hence effectively two pulses are retransmitted down the discharge cavity of similar orders of magnitude, with one running slightly off axis and leading the second by $\simeq$ 0.5 ns. This explains the observed pulse structure and why this structure disappeared with further misalignment of the Pockels cell - since less light due to reflection from the cell entry window then emerged through the aperture at the output end of the cavity.

The total energy in the pulse train was a fraction of a mJ and not measured directly. Peak pulse powers were estimated in two ways. First, by considering the amount of optical attenuation needed to produce the equivalent photodiode signal from a much larger pulse of known energy (the un-mode-locked XeCl laser), and second, by comparison with the pulses switched out by the modulator external to the cavity in Chapter 4 (figure 40), whose energy could be estimated from

the known efficiency and losses of the modulator. Both techniques imply peak powers in the range 1-3 kW corresponding to an energy $\simeq 2$ μJ in a 1 ns F.W.H.M. pulse.

Some pulse shortening was observed through the pulse train, and pulses of $\simeq 1$ ns duration were observed towards the end. Section 6.2.3 will now describe the results found when using the faster, more efficient modulator of Chapter 5 for mode-locking.

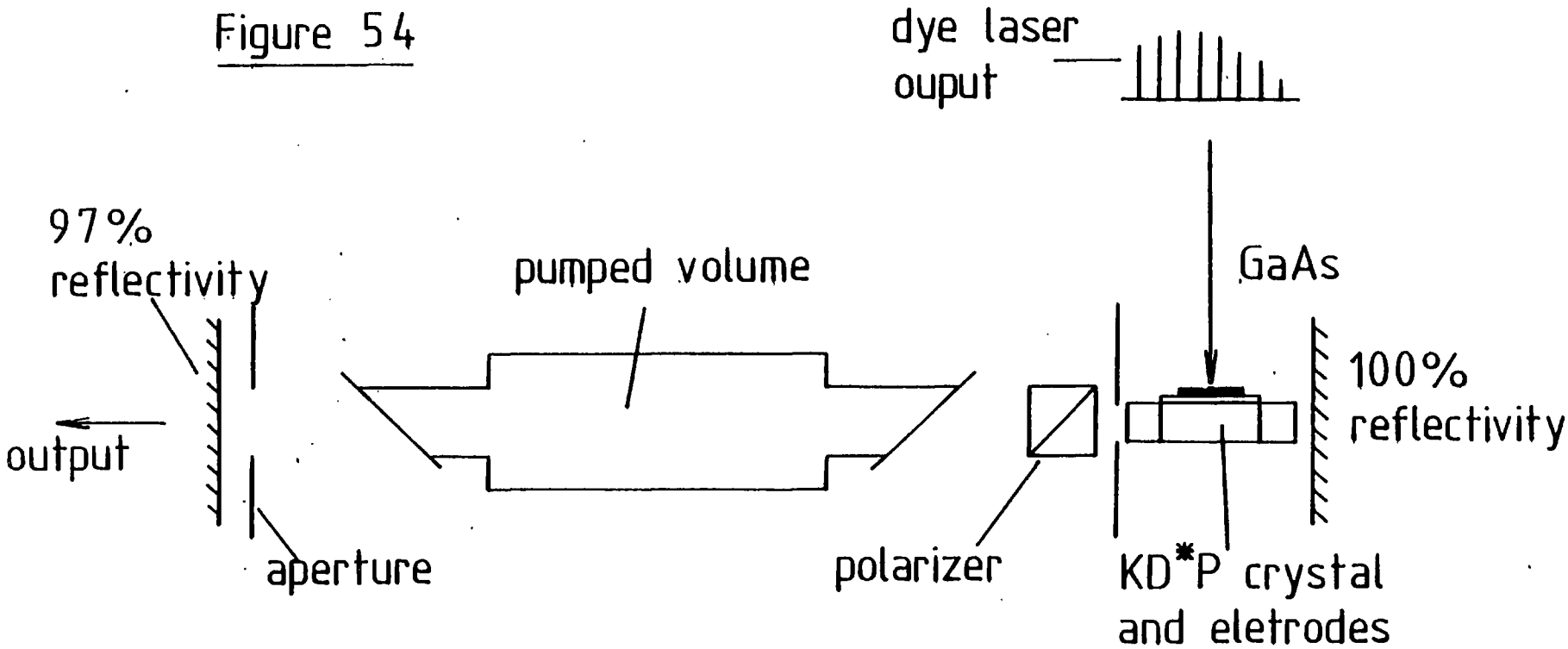
6.2.3 Active mode-locking with the redesigned modulator

The commercial Pockels cell was replaced by the fast modulator in the arrangement of figure 54. The alignment procedure was carried out as before, and the full 5 x 5 mm^2 aperture of the KD*P crystal was used.

When a bias voltage of 1.2 kV was applied to the crystal no laser action was observed. With application of the dye laser pulse train to the GaAs switch, the output of figure 55(a) was recorded. In an effort to produce a longer pulse train, the crystal bias voltage was increased to 3.6 kV, such that light would undergo a 270° rotation of its plane of polarization on a double pass through the crystal. Figure 55(b) was the recorded output in this case when the switch was illuminated. A longer output train was achieved because efficient operation could only occur in the first case if the voltage across the crystal dropped to nearly zero on illumination of the switch, whereas in the second a drop to only two thirds of the original voltage would be equivalent to a 180° rotation in the plane of polarization of the incoming light on a double pass of the modulator, and therefore efficient coupling back into the gain region.

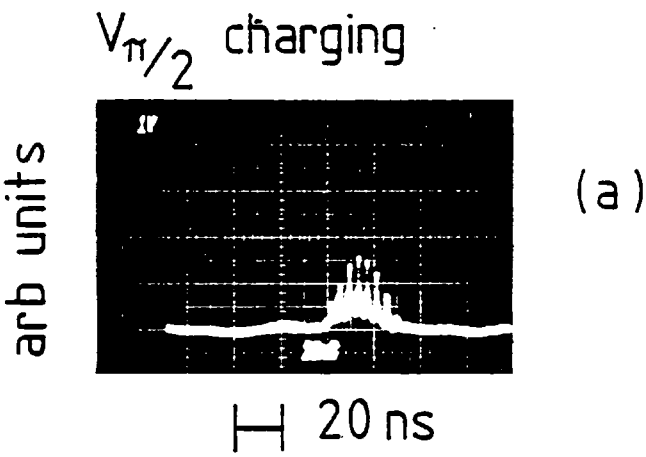
Peak powers were estimated as before to be 1 kW in the first case ($V_{\pi/2}$) and 4 kW in the second ($V_{3\pi/2}$), accurate to no

Figure 54



Mode-locking with the redesigned modulator

Figure 55



Output of the actively mode-locked XeCl laser (redesigned modulator)

better than 50%. The beam area was 5 x 5 mm^2. For $V_{\pi/2}$ charging the pulse lengths were estimated to be (figure 55(a)) $\lesssim$ 400 ps, the duration of the optical shutter in this configuration. A streak camera was available for a short time to measure these pulses, but without success. The failure was due to the short duration and low light level of the train, and the unreliability of the excimer laser which was operating near to threshold. An accurate measurement was not important, however, since the shutter speed was known, and the pulse train was too short to yield any substantial shortening. The 400 ps estimate was greater than that of the modulator external to the cavity (figure 49(b)). This was because any light which was within the crystal, travelling in either direction, as the voltage modulation occurred, would suffer some change of phase retardation and partial coupling back into the gain region, i.e. the pulse of light coupled back began with that light which was re-emerging from the crystal on its second pass as the voltage modulation was applied, and ended with that entering the crystal $\simeq$300 ps later as the modulation stopped. For the single pass modulator only light within the crystal on the single pass or which entered during the period of the modulation suffered a change in phase retardation.

At the higher charging voltage, $V_{3\pi/2}$, the structure observed occurred as the light was retarded more than required for the most efficient switching, equivalent to the voltage falling to two thirds of its bias value for two passes of the crystal. A further increase in the efficiency of turning off the crystal bias voltage then resulted in a less efficient optical modulator. A reduction in the light intensity striking the GaAs switch reduced the structure and visibly shortened the pulses, but was difficult to reproducibly control. Pulse

Table 6

Mode-locking element	Pulse duration	Peak power (approx)	Modulation depth	Period of laser action
Pockels cell	1ns	2kW	>95%	100ns
Redesigned modulator, $V_{\pi/2}$	400ps (estimated)	1kW	90%	60ns
$V_{3\pi/2}$	1ns	4kW	75%	120ns

Summary of active mode-locking results

lengths of $\lesssim$ 1 ns were measured from oscilloscope traces.

Table 6 summarises the results obtained with the various methods of active mode-locking. A less than 100% modulation depth was obtained with the faster modulator because of the non-uniformities within the crystal.

6.2.4 Discussion

The double pass transit time of the crystal to the silvered mirror is 200 ps and is of the same order as the measured optical modulation period of 300 ps. A further reduction in the switching time of the modulator would reduce its efficiency and lead to less efficient laser operation (section 5.2). This particular system is therefore reaching its limits of useful operation with respect to active mode-locking.

As table 6 shows, the losses introduced by the elements of the modulators restrict the period of laser operation, but this is not as important as the fact that very little pulse shortening is observed over the number of roundtrips available with the laser. This rate of shortening is slower than the theoretical limit[111] and implies that pulse lengths very much shorter than the shutter speed will, in general, require laser action for times not so far available with excimer lasers.

At higher power densities, gain saturation may affect the pulse length (saturation intensity $\simeq$ 0.1 MW cm^{-2} for XeCl, with $\sigma\tau$ = 50 Å^2 ns[113]). In theory, when saturation occurs, the leading edge of a pulse sees a very high gain, while the trailing edge experiences reduced gain due to depletion of the population inversion. A change in pulse shape and a shift in the centre of the pulse is therefore expected. The effect on the pulse duration depends on the shape of the leading edge of the pulse, and this effect alone may produce only pulse distortion

as in the case of the amplification of ps dye laser pulses[114]. However, combined with the effect of the active mode-locking element, which will tend to cut off the leading edge of a pulse as it is pulled forward by gain saturation, the net result may be to shorten the duration of a pulse (assuming the modulator is driven at the round-trip frequency of the cavity). The extent of the pulse shortening will depend on the gain recovery time of the laser and upon the mismatch between the modulator and cavity roundtrip frequencies. This mechanism may be responsible for the production of 310 ps pulses from a mode-locked discharge XeCl laser, with the > 1 ns period modulator described in Chapter 4[78], after only 3 roundtrips.

In summary, a long pulse XeCl laser has been actively mode-locked to give pulses of $\simeq$ 400 ps duration with powers in the kW range. Although the technique is reaching the limit of its usefulness, a number of options are available to increase output powers and decrease further the pulse lengths generated. First, the problem of the restricted electrooptic crystal aperture can be solved by telescoping the 2.5 cm XeCl beam down to the required size. This has successfully produced an order of magnitude increase in total output power, but at the expense of an increased cavity length and a higher threshold for laser operation. Second, the speed of the modulator could be increased with the travelling wave technique (Chapter 5) which, although complicated, might produce pulses with a reasonable efficiency with widths approaching the duration of the pulse from a GaAs switch (as short as $\simeq$ 30 ps[88] operating at low voltage snd switching inefficiently). To achieve any substantial pulse shortening over the pulse train, with the gain duration of XeCl lasers at present available, would require a high enough gain for saturation to become important. Even then,

the mechanism for pulse shortening and the pulse durations which might be obtained are unclear, although it is unlikely that durations approaching the bandwidth limit could feasibly be obtained without much longer periods of laser operation.

6.3 Passive mode-locking

6.3.1 Introduction

Technically, when passive mode-locking is possible for a particular laser it is very much simpler than the active alternative, involving only the insertion of a cell containing an absorbing dye with a fast relaxation time within the laser cavity. This section will describe qualitatively the consequent build up of short pulses[115].

At its simplest, the absorbing dye can be thought of as a two level energy system. A pulse of incident laser light is strongly absorbed unless its intensity is such that the absorber ground state is substantially depleted, correspondingly increasing the transmission. Following the passage of the pulse, the absorber relaxes back into its ground state.

At the threshold of laser action, the radiation inside a cavity consists of random intensity fluctuations in time, due to the randomness of the cavity modes, with spikes of several times the average energy and durations typically of the order of the inverse laser bandwidth. In the linear development period which follows the radiation power moves from this spontaneous noise level to the point where non-linear absorption becomes important and, due to the selection of modes in the amplification process, the spectral distribution narrows with a corresponding increase in the duration of fluctuations. At the end of this phase, the most intense pulse is preferentially passed by the absorber and is further amplified in the active

medium, becoming dominant relative to the background noise. If the absorber relaxation time is long compared to the duration of the fluctuations, then several pulses may pass before this occurs and the evolution of a single pulse is prevented. Conversely, for a relaxation time much shorter then the fluctuation duration pulse shortening occurs with a corresponding increase in spectral width.

Picosecond pulses have been reliably generated by this technique in giant pulse lasers, such as Nd :glass or ruby, and continuous or quasi-continuous systems such as dye lasers. Mode-locking of dye lasers[116] has been seen to produce pulses with durations much shorter than the absorber recovery time. To explain this pulse compression it is necessary to consider the effects of both saturable absorption and saturable amplification on the shape of a pulse[117][118]. The saturable absorber can cause a steepening of the leading edge of a pulse because of the discriminating nature of the dye on low level intensity components. Saturable amplification arises from the non-linearity of the gain in the active medium (section 6.2.4). When the radiation is sufficiently intense it can sweep out a high proportion of the population inversion so that the radiation following experiences a reduced gain. Hence, amplification of the leading edge and reduced amplification of the trailing edge gives rise to an effective decrease in pulse width. Substantial pulse shortening has been observed by this process over periods of 20-30 roundtrips[119].

6.3.2 Passive mode-locking of excimer lasers

Pulse generation from excimer lasers which was, in theory, due to mode-locking, has been reported for both XeF (351 nm)[75] and KrF (248 nm)[120] lasers. In both cases, short pulse dis-

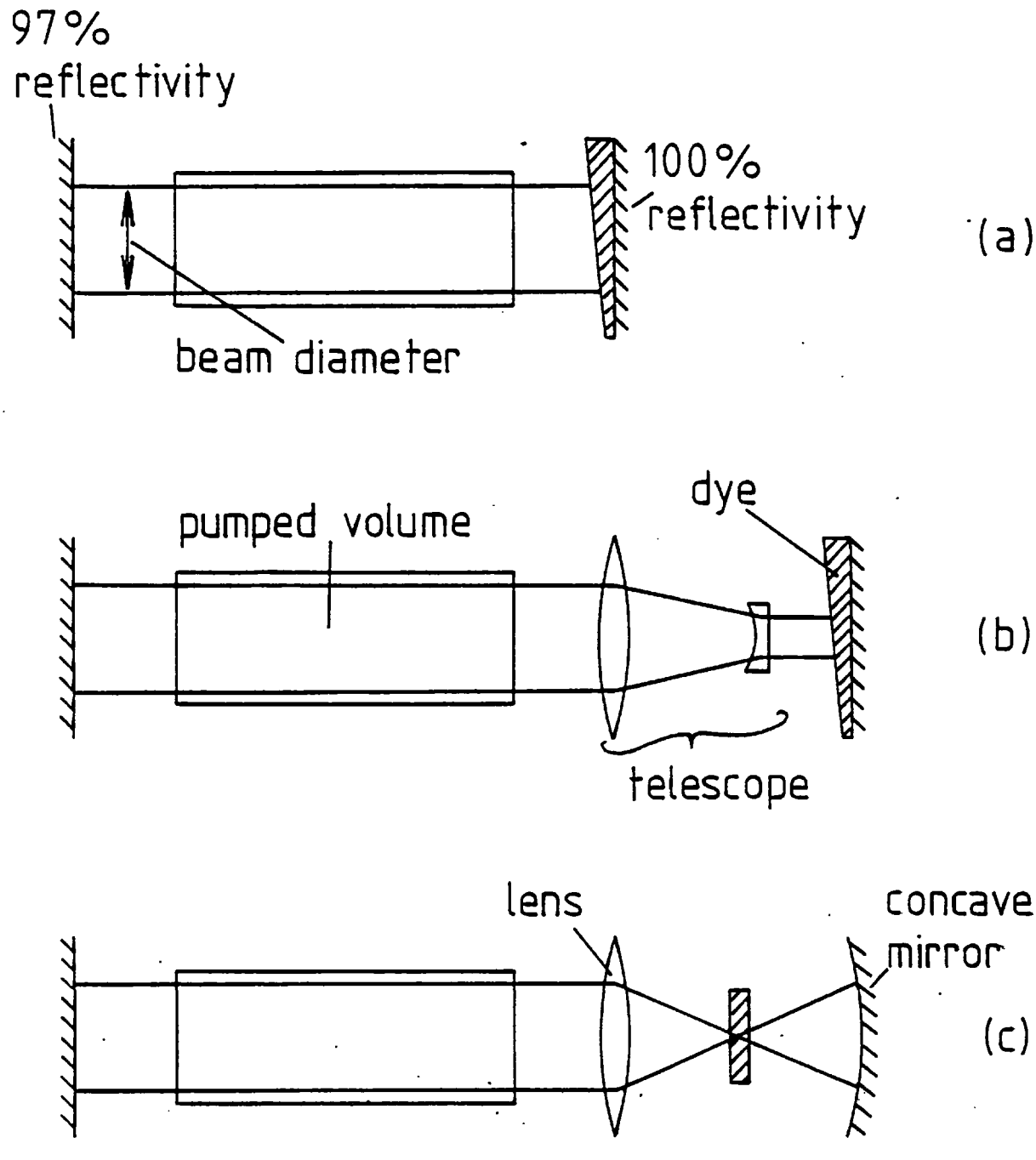
charge excited lasers were used. For XeF the best results were found with auramine hydrochloride, a dye with an excited state lifetime of the order of ps, as the saturable absorber. Three long pulses were produced with a modulation depth of 50%. In the KrF experiment, pulses of $\lesssim$ 2 ns duration and $\simeq$ 1 MW peak power were obtained with a 85% modulation depth. The best results were obtained for the dyes p-terphenyl (relaxation time τ = 1.5 ns) and auramino-O ($\tau \simeq$ ps). These results prompted an investigation of passive mode-locking with the long pulse XeCl laser. It was hoped that the gain duration of the laser would allow enough roundtrips for pulses to form and shorten.

Many common dyes were available and known to strongly absorb light at UV laser wavelengths, pumped, for example, by KrF[121] or XeCl[122] lasers. Their suitability for mode-locking was dependent on their absorption cross section, quantum efficiency and excited state lifetime. However, the complexity of those molecules and the uncertainties about their behaviour when exposed to intense UV radiation, especially as to whether they could be considered as simple, saturable two level systems, meant that particular dyes could not be confidently chosen. A number of available dyes were therefore experimented upon.

The experimental arrangements of figure 56 were used. 56(a) was the simplest and allowed the shortest cavity length. However, it was clear that the power densities generated by the laser, even with two high reflectivity mirrors, would be insufficient to saturate the dyes of lower cross sections.

Figures 56(b) and (c) both solved this problem at the expense of increased cavity length. In the first, an intercavity telescope allowed the projection of a parallel beam onto an adjustable dye cell (cell width $\lesssim$ 2 mm) contacted to

Figure 56



Passive mode-locking schemes

a silvered mirror. The telescope consisted of a converging bi- or plano-convex Spectrosil B lens of 50 mm aperture, and a plano-concave lens of 10 mm aperture. All lenses were anti-reflection coated at 308 nm to minimise losses, and different combinations of focal lengths allowed the 2.5 cm diameter beam emerging from the discharge cavity to be reduced to between 1% and 74% of its original area at the dye cell. The lenses were set up with the HeNe alignment laser and slightly adjusted to account for the calculated differences in their focal lengths in the UV. Light intensities at the dye cell could then be accurately controlled. However, it was found that, especially for the higher magnification telescopes, the damage threshold for the silvered 100% reflectivity mirror (coated with SiO_2) was being exceeded for dye concentrations which allowed a substantial fraction of the incident light through the cell.

Figure 56(c) finally solved this, but meant that a contracted dye cell could no longer be used. While this is not optimum for short pulse generation[118], it would not affect the possibility of observing modulation. In this case, the light was focussed down by the 10 cm focal length lens into a 1 mm wide quartz dye cell. A 10 cm radius of curvature mirror with a 100% (silvered) reflectivity completed the laser cavity. Hence, high power densities could be generated in the dye without the danger of damaging mirror coatings.

For all configurations, the dye cell windows were misaligned to prevent laser action occurring from them. Concentrated dye was introduced into the cell and gradually diluted until the threshold for XeCl laser action was reached. Further dilution was then carried out until either mirror damage occurred or the cell effectively contained only solvent.

Table 7 summarises the known characteristics of the dyes

Table 7

dye	solvent	fluorescence lifetime	extinction coefficient ϵ l/mole cm	
p-terphenyl	ethanol	940ps [123]	5000 [124]	laser dyes
p-quaterphenyl	toluene	700ps [123]	31000 [124]	
BBD	toluene	920ps [124]	48000 [124]	
coumarin (1)	ethanol	5ns [123]	3000 [129]	
α NPO	toluene	2ns [124]	16000 [124]	
bis-MSB	toluene	1.3ns [124]	30000 [124]	
tinopal CBS=X	ethanol	0.5ns [130]	-	fluorescent brightener
uvitex OB	ethanol	0.5ns [130]	-	

Saturable absorbers for passive mode-locking

used. The convenient molar extinction coefficient, ϵ is defined by the relationship

$$I = I_0 10^{-\epsilon c d} \qquad (6.7)$$

where I_o is an incident light intensity and I the remaining intensity after traversing d cm of dye of concentration c moles l^{-1}. ϵ (l/mole cm) is simply related to the absorption cross section σ (cm^2) by $\sigma = 3.8 \times 10^{-21} \epsilon$. Most of the available dyes had similar fluorescence lifetimes. Where possible, those with higher cross sections were chosen to minimise the light intensity needed to produce saturation ($\propto 1/\sigma\tau$). It was also preferable that they had been successfully used in excimer-pumped dye lasers, since this meant that they were stable under intense UV illumination. In addition to dyes, both thin glass slides and UV filters were considered as alternative saturable absorbers.

In none of these experiments, under any conditions, was modulation of the laser output observed.

6.3.3 Discussion

The saturable absorbers of table 7 all have reasonable cross sections and fast relaxation times. They have, in many cases, been used as laser dyes and are therefore stable under intense UV illumination. Hence, the reason for this failure to passively mode-lock the XeCl laser must be sought elsewhere.

First, the supposedly successul passive mode-locking of XeF[75] and KrF[120] must be considered further. There is some evidence that mode-locking may not have been observed at all. It has been shown in experiments on a discharge excited KrF laser[125] that under certain conditions the optical loss originating from an inter-cavity dye solution may lead to relaxation oscillations.

The size and, more crucially, the period of these oscillations was found to depend on the cavity lifetime and pump rate. Passive mode-locking, using the dyes for which successful results had been claimed, was not observed.

A number of conditions must be met before pulse compression can occur in a dye laser[118]. One of these is that the gain recovery time must be of the same order as the cavity round trip time ($t_R/\tau_A \simeq 1$), otherwise full recovery of the population inversion during a roundtrip gives rise to amplification of the leading edge of the pulse. In the case of excimer lasers, vibrational relaxation repopulates the upper laser level. For KrF the gain recovery time has been shown to be approximately equal to the fluorescence decay time of the upper laser level[125] which is itself typically in the range 0.6 - 2.5 ns, depending on the total gas pressure. The first figure corresponds more closely to a realistic laser pressure. In a discharge pumped XeCl system the gain has been found to recover in two stages, with a substantial recovery on a sub-ns timescale[69]. Hence, in both lasers the relationship $t_R/\tau_A \simeq 1$ does not hold (in this case $\tau_A < 1$ ns, $t_R \simeq 8$ ns). Although this relationship has not been derived for the case of excimer lasers, it may indicate the reason why passive mode-locking has not been successful. Not only will pulse compression not occur, but also the chance of a single noise spike being selected by the absorber and becoming dominant with respect to a low level background is much less. A spike may be selected by the absorber, but before it can build up to the point where it becomes dominant, many others will also be generated. As is, in fact, observed, the dye inside the cavity would appear to "open" but then remains open.

In order to make this explanation rigorous, the rate equations for the amplifying and absorbing media in question

would need to be solved. Practically, it may be possible to substantially reduce t_R, but it is difficult to foresee how this could be made $\simeq 1$ ns using available pumping methods.

6.4 Conclusions

An alternative technique to those described so far, which has allowed short pulse generation in the UV, is injection locking[127]. In this experiment, a mode-locked Rh 6G dye laser was frequency tuned with two Fabry-Perot etalons, such that, on doubling the output in an ADP crystal, the wavelength of the output overlapped that of the stronger XeCl laser transition. On injection into a discharge pumped XeCl laser, which would have commenced laser action without the presence of the injected pulses, self-oscillation of the amplifier was prevented, and a train of 5-7 intense ps pulses at 308 nm were obtained ($\simeq 2$ mJ in 7 ps) with no observable background.

Injection mode-locking or pulse amplification is the method by which the most powerful ultrashort pulses can at present be generated in the UV. The method is complicated, however, and depends on matching the excimer wavelength to that of a frequency doubled dye laser. It is only recently that tunable flashlamp pumped dye lasers operating in the blue/green have been passively mode-locked[128], and the injection locking technique may now be extended to shorter excimer wavelengths. Active mode-locking by the method described can be applied to most wavelengths (depending on polarizer and Pockels cell losses) without changing the dye laser. It also has the decided advantage that the combination of an untuned, mode-locked Rh6G dye laser and an excimer laser is very reliable.

CHAPTER 7

CONCLUSIONS

7.1 Introduction

Following a brief review of the important results so far reported, this chapter will go on to consider the ways in which the laser system might be improved and the further experiments which could be carried out with it.

7.2 Review

7.2.1 The laser system

An electron beam sustained discharge excimer laser was developed and characterised in detail. The electron beam generator comprised a 200 kV pulse transformer driven power supply and an electrostatically focussed electron beam diode. When a discharge circuit was incorporated, and the whole system used to pump an XeCl excimer laser, average output power densities of 0.63 MW cm^{-2} in a 250 ns (FWHM) pulse were obtained at 308 nm. The enhancement ratio for this system, of the power deposited in the gas from the discharge to that from the electron beam, was 4.8. This high value reflects the care taken in the design and optimisation of the pulsed power supply and electron beam diode. Consequently, relatively high laser output power densities were achieved using a modest electron beam generator which was compact and extremely reliable. The reliability of the system meant that a number of experiments could be successfully carried out with the laser, some of which had a reasonable degree of technical complexity (7.2.2). An extraction efficiency of 1.5% was found for the XeCl laser, and gain and beam quality measurements were made. KrF operation of the system was considered, and the discharge was found to be

unstable for all available combinations of electron beam current density, discharge voltage and capacitance, and gas mixture.

7.2.2 Pulse generation

Most of the work carried out with the XeCl laser concerned the repetitive generation of short duration UV laser pulses.

The illumination of a semi-insulating GaAs switch with pulses of visible light from a passively mode-locked dye laser can lead to the generation of very short high voltage pulses. The use of these pulses to drive optical modulators was considered. A study of a commercial Pockels cell was made which led to the development of a simple electrooptic modulator. When incorporated into an optical shutter, pulses of 300 ps duration were switched out at a repetition rate of > 0.1 GHz. Active mode-locking experiments were carried out with both the commercial Pockels cell and redesigned modulator, and pulses with durations of the order of the shutter period were produced. Unsuccessful passive mode-locking experiments were finally performed and tentative reasons for their failure given.

7.3 Further work

7.3.1 The laser system

A number of improvements could be made to the XeCl laser in order to increase its output energy without the need to modify the electron beam generator. It was seen in Chapter 3 that the extraction volume for the system was only $\simeq$50% of the total pumped volume. Hence, a redesigned discharge cavity with larger aperture optics should lead to a doubling of the total output energy. A disadvantage of this would be a beam emerging from the laser with an approximately trapezoidal, rather than circular, cross-section.

As a second step, the pumped volume could also be increased by a more efficient use of the electron beam. At the prefoil, the optimum beam height was 4 cm, or twice the window aperture. Therefore a new 4 cm wide window would double the volume pumped by the electron beam, although the strength of the Hibachi support structure might have to be increased to support the extra strain on the foil. The energy storage in the discharge would similarly need to be enlarged; the simplest way, which would avoid the breakdown problems of higher discharge voltages, being to approximately double the capacitance. A further increase in the size of the optics would now be required, but up to a fourfold increase in the laser output energy compared to the original system would be expected. The final level of the output would depend on how efficiently the discharge energy could be coupled into the lower impedance discharge. This would depend on how low the inductance of the discharge circuit could be made and might require that the energy be delivered from some form of low inductance line rather than a simple capacitor bank.

In order to further improve the system, either to give higher output power densities for XeCl or to allow sustained discharge operation of a KrF laser, it would be necessary to make the electron beam current density reaching the discharge cavity larger. Replacing the prefoil by a crowbar would give a small improvement, but the main foil would then be unprotected from diode arcs. Also, a further study of the electron beam focussing structure, perhaps involving a consideration of other cathode materials, might prove useful. However, effectively a new pulsed power supply would be required to allow a substantial change to be made to the current density.

7.3.2 Mode-locking

Proposals to improve the efficiency and speed of the optical shutter have been made (Chapter 5). It was pointed out that, in order to further investigate the possibilities of pulse shortening in an actively mode-locked laser, a higher gain, long pulse system would have to be developed.

7.3.3 Other experiments

Although the active mode-locking of this particular laser cannot usefully be pursued much further, the synchronised dye laser/excimer laser combination could be used in a number of other experiments.

Tuning the mode-locked dye laser and frequency doubling the output would permit a study of injection-locking and a further investigation of the behaviour of the laser gain. In the first case, the experiments on discharge pumped systems[127] could be repeated (section 6.4). Since the cavity would not contain any lossy internal elements, and since injected pulses might encourage the earlier build-up of laser action[131], the effect of saturable gain could be observed with the laser run at full pump-power. However, at the peak of the pumping curve, due to the fast recovery of the laser gain, self-oscillation of the laser cavity might begin in the period between the injected pulses. It might therefore be necessary to reduce the pump power to the level where the injected pulses see a net gain which is above the threshold level, while the gain is depleted enough to be below threshold in the period between pulses. The gain must be recovering to a value above threshold as the pulse re-enters the gain region.

The evolution of the injected pulse could be monitored, in the first place, to observe the effect of saturable gain over

many roundtrips. A dye cell could then be introduced and the effect of the saturable absorber considered. If the pulse shortening requirements for dye lasers outlined in Chapter 6 are applicable to excimer lasers, then the relationship between gain recovery and cavity roundtrip time will mean that rapid pulse shortening will not occur.

Injecting pulses from the dye laser whose cavity length slightly exceeded that of the excimer would allow the gain recovery of the laser to be studied. As the first pulse completed a trip around the cavity, a second would be injected, delayed with respect to the first. A train of pulses would build up in this way. In the linear gain period, the pulses would be equally amplified, but as the first pulse began to saturate the gain the rate of its recovery would be directly observable in the level of gain experienced by the following pulses.

The temporal and spectral behaviour of the gain could also be investigated by considering the small signal gain seen by the tuned dye laser pulses, with the discharge cavity as an amplifier. Under conditions of laser action it would also be interesting to observe the two components of the XeCl laser output (Chapter 1) as a function of time, and the extent to which, in the long pulse system, one became dominant due to the homogeneous nature of the transition.

A new generation of flashlamp-pumped dye lasers[128] will allow the extension of these techniques to other excimer wavelengths. With relevance to Chapter 3 would be an accurate measurement of the variation of the gain of the KrF laser with time, which should confirm the presence of a discharge instability and collapse of the laser gain. Other excimers, such as XeF, should also be studied in the long pulse system in order to

obtain a better understanding of the practical effect of the halogen donor on the stability of the discharge.

Finally, a number of tuning experiments could be carried out with this system. The long gain duration should allow a spectrally narrow output to be generated. To simultaneously obtain both good spectral and spatial beam quality it would probably be necessary to injection lock the long pulse system, itself in an unstable cavity configuration, with the narrow band output of a master oscillator, perhaps in the form of an etalon[132] or grating[133][134] tuned short pulse, discharge pumped laser.

In conclusion, while X-ray preionized systems (Chapter 1) will allow larger volume operation at high repetition rates, this system will continue to have many uses in experiments where a reliable, high output power density laser is required.

REFERENCES

(1) A.E. Siegman, An Introduction to Lasers and Masers, (McGraw-Hill), 395 (1971)

(2) P.J. Hay, T.H. Dunning, Jr., J. Chem. Phys. 66, 1306 (1977)

(3) P.J. Hay, T.H. Dunning, Jr., J. Chem. Phys. 69, 2209 (1978)

(4) J.J. Ewing, C.A. Brau, Phys. Rev. A12, 129 (1975)

(5) P.C. Tellinghuisen, J. Tellinghuisen, J.A. Coxon, J.E. Velazes, D.W. Setser, J. Chem. Phys. 68, 5187 (1978)

(6) J. Tellinghuisen, J.M. Hoffman, G.C. Tisone, A.K. Hays, J. Chem. Phys. 64, 2484, (1976)

(7) L.A. Gundel, D.W. Setser, M.A.A. Clynne, J.A. Coxon, W. Nip, J. Chem. Phys. 64, 4390 (1976)

(8) C.A. Brau, J.J. Ewing, J. Chem. Phys. 63, 4640 (1975)

(9) D.C. Lorents, D.L. Huestis, M.V. McCusker, H.H. Nakano, R.M. Hill, J. Chem. Phys. 68, 4657 (1978)

(10) R.M. Hill, P.L. Trevor, D.L. Huestis, D.C. Lorents, Appl. Phys. Lett. 34, 137 (1979)

(11) M.H.R. Hutchinson, Appl. Phys. 21, 95 (1980)

(12) M.J. Shaw, Prog. Quant. Elect. 6, 3 (1979)

(13) M. Rokni, J.A. Mangano, J.H. Jacob, J.C. Hsia, IEEE J. Quant. Electron. QE-14, 464 (1978)

(14) C.A. Brau, in Excimer Lasers, ed. C.K. Rhodes (Springer-Verlag), 87 (1979)

(15) L.A. Levin, S.E. Moody, E.L. Klosterman, R.E. Center, J.J. Ewing, IEEE J. Quant. Electron. QE-17, 2282 (1981)

(16) N.T. Olson, Optical Spectra 10, 42 (December 1976)

(17) S. Humphries, Jr., C. Eichenberger, E. Maeke, H. Sanderson, A. Wright, Cornell University Report, LPS 220 (March 1977)

(18) T.H. Storr, A.W.R.E. Report, SSWA/TS/7310/557

(19) R.A. Fitch, IEEE Trans. Nucl. Sci., 18, 190 (1971)

(20) J.C. Martin, A.W.R.E. Report, SSWA/JCM/704/49

(21) J.C. Martin, I.D. Smith, U.K. Patents Nos. 1, 114, 713 (1968) and 3, 456, 221 (1969)

(22) C. Edwards, M.D. Hutchinson, J.C. Martin, T.H. Storr, A.W.R.E. Report, SSWA/JCM/755/99

(23) A.D. Blumlein, U.S. Patent No. 589127 (1974)

(24) S.P. Bugaev, G.A. Mesyats, D.I. Proskurovski, Sov. Phys. -Dokl. 14, 605 (1969)

(25) C.D. Child, Phys. Rev. 32, 492 (1911)

(26) M.L. Bhaumik, R.S. Bradford, Jr., E.R. Ault, Appl. Phys. Lett.28, 23 (1976)

(27) J.D. Daugherty, J.A. Mangano, J.H. Jacob, Appl. Phys. Lett. 28, 581 (1976)

(28) E.A. Stappaerts, H. Kominie, S.J. Brosnan, W.H. Long, Jr., Conference on Lasers and Electro-Optics, Phoenix, Arizona (1982)

(29) A.J. Andrews, A.J. Kearsley, C.E. Webb, Opt. Commun. 20, 265 (1977)

(30) R. Burnham, N.W. Harris, N. Djeu, Appl. Phys. Lett. 28, 86 (1976)

(31) T.J. McKee, J. Banic, A. Jares, B.P. Stoicheff, IEEE J. Quant. Electron. QE-15, 332 (1979)

(32) R. Burnham, N. Djeu, Appl. Phys. Lett. 29, 707 (1976)

(33) D.E. Rothe, R.A. Gibson, Opt. Commun. 22, 265 (1977)

(34) K.L. Kohla, Laser Focus 18, 67 (June 1982)

(35) Lambda Physik, Model No. EMG 201 E (1982)

(36) S. Sumida, M. Obara, T. Fujioka, Appl. Phys. Lett. 33, 913 (1978)

(37) S. Lin, J.I. Levatter, Appl. Phys. Lett. 34, 505 (1979)

(38) S. Lin, Bao Zhi-xiang, Gong Guang-yuan, Huo Yun-sheng, Shu Ju-ping, Tang Shi-qing, Wei Yun-rong, Zheng Cheng-en, Appl. Phys. Lett. 38, 328 (1981)

(39) J.I. Levatter, K.L. Robertson, S. Lin, Appl. Phys. Lett. 39, 297 (1981)

(40) J.I. Levatter, Z. Li, Rev. Sci. Instrum. 52, 1651 (1981)

(41) A.J. Mendelsohn, R. Normandin, S.E. Harris, J.F. Young, Appl. Phys. Lett. 38, 603 (1981)

(42) J.F. Young, S.E. Harris, P.J.K. Wisoff, A.J. Mendelsohn, Laser Focus 18, 63 (April 1982)

(43) J.J. Ewing, C.A. Brau, Appl. Phys. Lett. 27, 350 (1975)

(44) L.F. Champagne, Appl. Phys. Lett. 33, 523 (1978)

(45) V.F. Losev, V.F. Tarasenko, Y.I. Bychkov, Sov. J. Quantum Electron. 9, 918 (1979)

(46) J.I. Levatter, J.H. Morris, S. Lin, Appl Phys. Lett. 32, 630 (1978)

(47) D.E. Rothe, J.B. West, M.L. Bhaumik, IEEE J. Quant. Electron. QE-15, 314 (1979)

(48) G.L. Oomen, W.J. Witteman, Appl. Phys. Lett. 33, 878 (1978)

(49) M.H.R. Hutchinson, P.W. Smith, Proceedings of the Electro-Optical/Laser International Conference '80, Brighton, (1980)

(50) J.C. Martin, P.D. Champney, D.A. Hammer, Cornell University Report (1967)

(51) Maxwell Laboratories Inc., Engineering Bulletin No. 1007 (1978)

(52) J.C. Martin, A.W.R.E., private communication

(53) I.E. Smith, Proceedings of the 1st Int. Symp. Insulation of High Voltages in Vacuum, Prague (1964)

(54) R.K. Parker, R.E. Anderson, C.V. Duncan, J. Appl. Phys. 45, 2463 (1974)

(55) I. Langmuir, K.T. Compton, Rev. Mod. Phys. 3, 191 (1931)

(56) D.W. Forster, A.W.R.E. Report, SSWA/DWF/733/398 (1973)

(57) J.C. Martin, A.W.R.E. Report, SSWA/JCM/759/193 (1975)

(58) G. Herbert, A.W.R.E., private communication

(59) E.J. Henley, Nucleonics 12, 62 (1954)

(60) J.G. Eden, D. Epp, Rev. Sci. Instrum. 51, 781 (1980)

(61) G.K. Loda, D.A. Meskan, Proc. Int. Top. Conf. on Electron Beam Res. and Tech., Albuquerque, New Mexico (1975)

(62) W.H. Long, R.S. Bradford, IEEE J. Quant. Electron. QE-15, 327 (1979)

(63) J.J. Ramirez, K.R. Prestwich, The REBLE Report, Sandia Laboratories, Albuquerque, New Mexico

(64) M.J. Berger, S.M. Seltzer, N.A.S.A. Report NASA-SP-3012 (1964)

(65) L.V. Spencer, N.B.S. Monograph No. 1 (1959)

(66) M.R.O. Jones, Ph.D. Thesis, University of London (1981)

(67) E. Armandillo, A.J. Kearsley, C.E. Webb, J. Phys. E : Sci. Instrum. 15, 177 (1982)

(68) N.E. Ernst, F.K. Tittel, IEEE J. Quant. Electron. QE-16, 945 (1980)

(69) P.B. Corkum, R.S. Taylor, XII International Quantum Electronics Conference, Munich (1982)

(70) A.E. Siegman, Proc. IEEE 53, 277 (1965)

(71) M.C. Gower, Opt. Commun. 36, 43 (1981)

(72) D. James, T.J. McKee, W. Skrlac, IEEE J. Quant. Electron. QE-15, 335 (1979)

(73) W.H. Long, J. Appl. Phys. 50, 168 (1979)

(74) P.W. Smith, Proc. IEEE 58, 1342 (1970)

(75) C.P. Christensen, L.W. Braverman, W.H. Steier, C. Wittig, Appl. Phys. Lett. 29, 424 (1976)

(76) J. Agostinelli, G. Mourou, C.W. Gabel, Appl. Phys. Lett. 35, 731 (1979)

(77) W. Margulis, W. Sibbett, J.R. Taylor, Opt. Commun. 35, 153 (1980)

(78) G. Reksten, T. Varghese, W. Margulis, Appl. Phys. Lett. 39, 129 (1981)

(79) A. Yariv, Quantum Electronics, 2nd Edition (John Wiley and Sons), 340 (1975)

(80) J.C. Scott, A.W. Palmer, J. Phys. E : Sci. Instrum. 11, 901 (1978)

(81) W. Zapka, R-K. Wu, J. Phys. E : Sci. Instrum. 15, 298 (1982)

(82) J.F. McCann, J. Pczy, P. Wilson, J. Phys. E : Sci. Instrum. 15, 322 (1982)

(83) D.H. Auston, Appl. Phys. Lett. 26, 101 (1975)

(84) P. LeFur, D.H. Auston, Appl. Phys. Lett. 28, 21 (1976)

(85) C.H. Lee, Appl. Phys. Lett. 30, 84 (1977)

(86) A.M. Johnson, D.H. Auston, IEEE J. Quant. Electron. QE-11, 283 (1975)

(87) W. Margulis, S. Laval, Appl. Phys. Lett. 40, 829 (1982)

(88) J.A. Valdmanis, G. Mourou, C.W. Gabel, Appl. Phys. Lett. 41, 211 (1982)

(89) E.G. Arthurs, D.J. Bradley, A.G. Roddie, Appl. Phys. Lett. 20, 125 (1972)

(90) M.C.P. Electronics Ltd.; Wembley, Middlesex. Data Manual (1974)

(91) V.K. Mathur, C.S. Chang, C.H. Lee, Rev. Sci. Instrum. 52, 616 (1981)

(92) D.S. Evans, G.R. Jessop. V.H.F.-U.H.F. Manual (RSGB Publications), 11.2 (1981)

(93) A. Yariv, Quantum Electronics, 2nd Edition (John Wiley and Sons), 349 (1975)

(94) Lasermetrics Inc., New Jersey, Model 111

(95) I.P. Kaminow, E. Turner, in the Handbook of Lasers (Chemical Rubber Company), 451 (1971)

(96) D.S. Evans, G.R. Jessop, V.H.F.-U.H.F. Manual (RSGB Publications), 3.5 (1981)

(97) K.J.R. Wilkinson, J. Inst. Elect. Engs. Pt. IIIA 93, 1090 (1946)

(98) O.L. Ratsey, J. Inst. Elect. Engs. Pt. IIIA 93, 245 (1946)

(99) Du Pont de Nemours International S.A., Technical Bulletin M-1E

(100) G. Mourou, W. Knox, Appl. Phys. Lett. 35, 492 (1979)

(101) L.L. Steinmetz, T.W. Pouliot, B.C. Johnson, Appl. Optics 12, 1468 (1973)

(102) J.C. Scott, A.W. Palmer, J. Phys. E : Sci. Instrum. 11, 901 (1978)

(103) M.G. Vitkov, Opt. and Spectrosc. 27, 185 (1969)

(104) W. Sibbett, D.J. Bradley, S.F. Bryant, Conference Digest, IX International Conference on Quantum Electronics (1976)

(105) D.J. Bradley, W. Sibbett, Appl. Phys. Lett. 27, 382 (1975)

(106) I.P. Kaminow, J. Liu, Proc. IEEE 51, 132 (1963)

(107) W.W. Rigrod, I.P. Kaminow, Proc. IEEE 51, 137 (1963)

(108) R.M. White, C.E. Enderby, Proc. IEEE 51, 214 (1963)

(109) J.J. Ewing, C.A. Brau, Appl. Phys. Lett. 27, 351 (1975)

(110) A. Yariv, Quantum Electronics, 2nd Edition (John Wiley and Sons) 266 (1975)

(111) A.E. Siegman, D.J. Kuizenga, Opto-electronics 6, 43 (1974)

(112) D.J. Kuizenga, D.W. Phillion, T. Lund, A.E. Siegman, Opt. Commun. 9, 221 (1973)

(113) C.A. Brau, J.J. Ewing, J. Chem. Phys. 63, 4640 (1975)

(114) A. Mingus, J.L. Martin, R. Astier, A. Orszag, in Picosecond Phenomena II, editors R.M. Hochstrasser, W. Kaiser, C.V. Shank (Springer-Verlag), 59 (1980)

(115) J.R. Taylor, Ph.D. Thesis,Queen's University of Belfast,1974

(116) D.J. Bradley, in Ultrashort Light Pulses, ed. S.L. Shapiro (Springer-Verlag), 18 (1977)

(117) G.H.C. New, Opt. Commun. 6, 188 (1972)

(118) G.H.C. New, IEEE J. Quant. Electron. QE-10, 115 (1974)

(119) E.G. Arthurs, D.J. Bradley, A.G. Roddie, Appl. Phys. Lett. 23, 88 (1973)

(120) T. Efthimiopoulos, J. Banic, B.P. Stoicheff, Can. J. Phys. 57, 1437 (1979)

(121) V.I. Tomin, A.J. Alcock, W.J. Sargeant, K.E. Leopold, Opt. Commun. 26, 396 (1978)

(122) O. Uchino, T. Mizunami, M. Maeda, Y. Miyazoe, Appl. Phys. 19, 35 (1979)

(123) J.R. Taylor, Imperial College, private communication

(124) I.B. Berlman, Handbook of Fluorescence Spectra of Aromatic Molecules, 2nd Edition (Academic Press, 1971)

(125) M.C. Gower, Rutherford and Appleton Laboratories Annual Report to the Laser Facility Committee, 2.22 (1981)

(126) K.T.V. Grattan, M.H.R. Hutchinson, K.J. Thomas, Opt. Commun. 39, 303 (1981)

(127) G. Reksten, T. Varghese, D.J. Bradley, Appl. Phys. Lett. 38, 513 (1981)

(128) W. Sibbett, J.R. Taylor, Opt. Commun. 43, 50 (1982)

(129) K. Drexhage, in Dye Lasers, ed. F.P. Schäfer (Springer-Verlag), 163 (1975)

(130) P.G. May, Imperial College, private communication

(131) C.B. Edwards, F. O'Neill, M.J. Shaw, Appl. Phys. Lett. 36, 617 (1980)

(132) J. Goldhar, W.R. Rapoport, J.R. Murray, IEEE J. Quant. Electron. QE-16, 235 (1980)

(133) R.G. Caro, M.C. Gower, C.E. Webb, J. Phys. D : Appl. Phys. 15, 767 (1982)

(134) J. Reintjes, Opt. Lett. 5, 342 (1980).

APPENDIX : PUBLICATIONS

(1) A Versatile Electron Beam Pumped Excimer Laser System, M. Casey, P.W. Smith and M.H.R. Hutchinson. Digest of Technical Papers, 3rd IEEE Pulsed Power Conference, Albuquerque, New Mexico, June 1981

(2) A High Power-Density Electron-Beam Sustained Laser, M. Casey, P.W. Smith and M.H.R. Hutchinson. Submitted to the Review of Scientific Instruments, September 1982.

A VERSATILE ELECTRON BEAM PUMPED EXCIMER LASER SYSTEM

M. Casey, P.W. Smith and M.H.R. Hutchinson

Optics Section, The Blackett Laboratory,
Imperial College, London SW7 2AZ, U.K.

Summary

A compact electron beam pumped excimer laser system has been developed capable of providing high power tunable VUV (10 MW) and UV (~30 MW) laser radiation in short pulses (~11 ns). With simple modifications longer UV laser pulse operation can be achieved (3 MW over 280 ns).

An unusually small high voltage pulsed power supply, the novel features of which are described, supplies one of three easily interchangeable laser heads. Two of the laser heads use coaxial electron beam diodes to pump the rare gas and rare gas halide excimers respectively. The third head relies on the electron beam sustained discharge technique for long pulse pumping of the rare gas halide excimers.

Introduction

The size and complexity of the majority of commercial electron beam pumped laser systems often means that they are not suitable for use in small laboratories. A system has therefore been designed which is not only small but can also pump a wide range of excimer lasers in both long and short pulse modes. The small size of the system, as shown in figure 1, is largely due to the use of a highly compact pulsed power supply. This power supply drives one of three laser heads, which bolt on to the front of the power supply. The short pulse rare gas halide laser head can be seen in position on the system in figure 1.

Pulsed Power Supply

The pulsed power supply can be operated in either a short or long pulse mode. Simple modifications are required to change from one mode of operation to the other. The power supply in both forms uses a pulse transformer to charge either a coaxial Blumlein P.F.L. for operation in the short pulse mode or a high voltage capacitive storage network to provide a longer, lower voltage pulse.

Short Pulse Operation

Figure 2 is a circuit diagram of the pulsed power supply in its short pulse form. The power supply is housed in an oil filled tank (0.66 x 1.22 x 0.48m^3). The compact size is due to the use of a pulse transformer for high voltage generation and a coaxial Blumlein P.F.L. which has an intermediate conductor in the form of a tape helix. Although a coaxial pulse forming line system has been demonstrated with a single helical coaxial line[1], it is believed that this is the first time that a Blumlein P.F.L. has been operated with a helical conductor. In this mode of operation the power supply can deliver a 20 ns pulse (rise time 3 ns) at up to 600 kV with a nominal output impedance of 40Ω.

C_2, which comprises two 0.3 μF rapid discharge capacitors in parallel, is charged from a 50 kV 200 Js^{-1} charging unit via a D.C. filter circuit which consists of L_1, L_2 and C_1. As the pulse transformer is an autotransformer with a two turn primary in the centre of the windings, the potential of the primary rises to half the output voltage of the transformer after C_2 has been discharged into the primary. Thus the D.C. filter network prevents energy returning to the charging unit from the transformer as the potential of the primary rises. C_2 is discharged into the primary windings of the transformer via a low inductance rail gap pressurised with dry air. The gap can be allowed to self-break or can be triggered, by applying a trigger pulse to a third blade electrode. The trigger unit must be isolated from the power supply because of the rise in potential of the primary transformer after triggering.

The transformer is of the Martin and Smith type[2] and has a turns ratio of 22:1. The observed and calculated

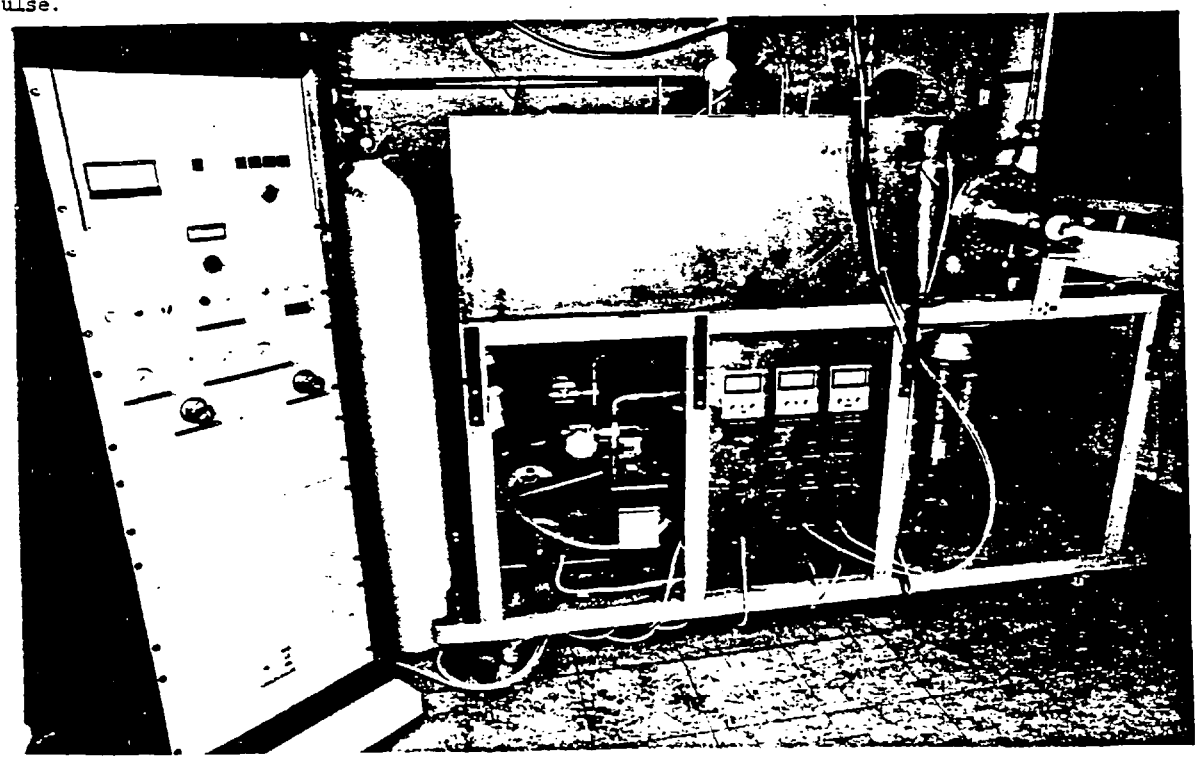
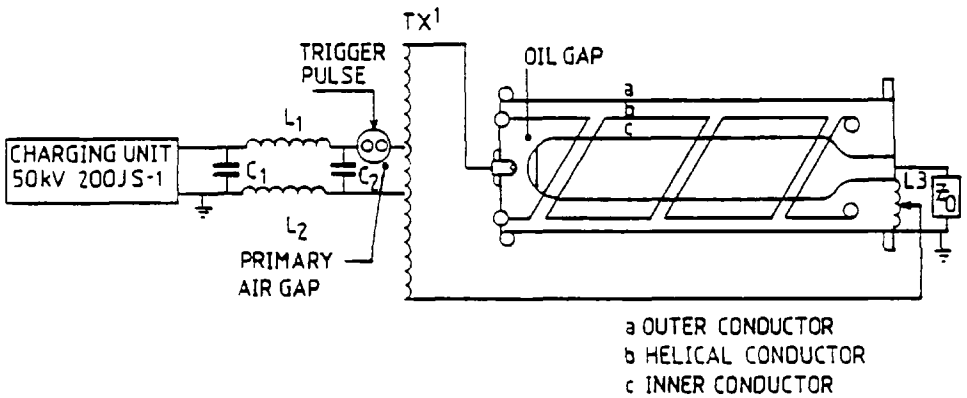


Figure 1: The complete system

C_1 0·01μF 50kV FILTER CAPACITOR
C_2 2 X 0·3 μF 75 kV RAPID DISCHARGE CAPACITORS
L_1 L_2 1·4mH
L_3 27μH SPIRAL INDUCTOR
TX 1 PULSE TRANSFORMER
2 TURN PRIMARY
TURNS RATIO 22:1
AUTOTRANSFORMER



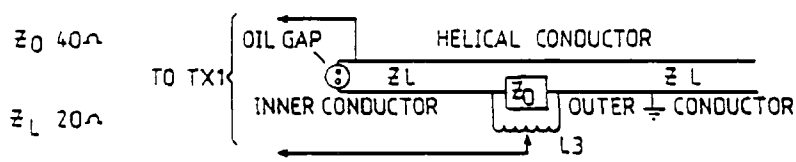


Figure 2: Circuit diagram of the short pulse version of the power supply

gain of the transformer is approximately 16.5. A small computer programme has been developed which accurately predicts the performance of this type of transformer under various load conditions.

The transformer charges a coaxial Blumlein P.F.L., with a helical intermediate conductor, to achieve pulse compression. The nominal output impedance of the Blumlein P.F.L. is 40 Ω. The helical conductor enables a pulse of 20 ns duration to be produced from a device which is only 1 metre long. The tape helix has just over three turns, and is supported within the structure by lucite "elephant's foot" spacers. A coaxial structure was chosen for ease of connection to the three laser heads. An adjustable, self-breaking oil gap is used to switch the Blumlein P.F.L.

Since the unrolled tape helix is a parallelogram, it was originally anticipated that the output pulse from the Blumlein P.F.L. would have a rise time corresponding to the difference in the time of travel of an electric wave along the two diagonals of the parallelogram. This effect is not observed as can be seen by the output pulse profile (figure 3) from the power supply when connected to an electron beam diode of approximately 40 Ω impedance. To explain this and also the two peak structure of the pulse, computer aided modelling of the Blumlein P.F.L. was undertaken using the computer code ECAP[3] in the transient analysis mode.

The two transmission lines of the Blumlein P.F.L. were approximated by two, twelve element lumped LC circuits, which were bridged over every four elements by a series combination of an inductor and capacitor. This inductor and capacitor were used to model the capacitive coupling between adjacent turns of the three turn tape helix. The resulting computation leads to an output pulse (figure 3) which is very similar in shape to that obtained experimentally. This suggests the interesting possibility that shorter multi-turn helical Blumlein P.F.L.'s may be feasible which produce good, fast rising and fast falling pulses, if the turn to turn coupling is optimised by, for example, the use of extra isolated conductors within the Blumlein P.F.L. structure. It is also interesting to note that as the inductance in series with the load is increased, or the capacitance in parallel with the load is increased, the height of the first peak in the pulse is reduced and the pulse develops a slow rising top.

Long Pulse Operation

In the long pulse form of the power supply, (see figure 4) the Blumlein P.F.L. is removed and is replaced by a high voltage capacitive storage element C_3 consisting of six capacitors connected in series, with voltage sharing resistors. The transformer is also changed to an oil impregnated, 8:1 turns ratio, pulse transformer similar in design to the original. A three turn primary is used and the measured and calculated gain of the transformer is 5.5. After C_3 is charged to a maximum value of 275 kV, SG2, which is a pressurized, sulphur hexafluoride filled spark gap, self-breaks to give a 250 kV output pulse of 450 ns (FWHM) duration. The approximate output impedance of the power supply in this form is 60 Ω and the output pulse risetime is 100 ns.

The output of the power supply in either form is connected to an appropriate laser head via a conventional field graded, oil to vacuum, high voltage bushing. The laser heads are then simply bolted on to the vacuum side of the bushing. The uniformity of field grading within the bushing was checked using a field plotting computer programme. The pulsed power supply is mounted on a welded steel table, and the vacuum systems for the laser diodes and laser gas handling systems are mounted beneath the table to facilitate the interchange of the three laser heads.

The Short Pulse Laser Heads

Coaxial electron beam diodes are used to pump gases contained in etched stainless steel anode tubes in both heads. The coaxial geometry was chosen because of the high degree of uniformity and efficiency of electron beam pumping which can be achieved [4,5]. The cathode in both heads consists of a cylinder 20 cm long and 13 cm in diameter in which three 20 cm lengths of razor blade are mounted on pegs, set at 120° with respect to each other. The anode tube lies coaxially within the cathode, the 20 cm long etched portion of the tube being positioned adjacent to the blades. The anode tubes are etched to a thickness of ∿ 50 μm. The current density

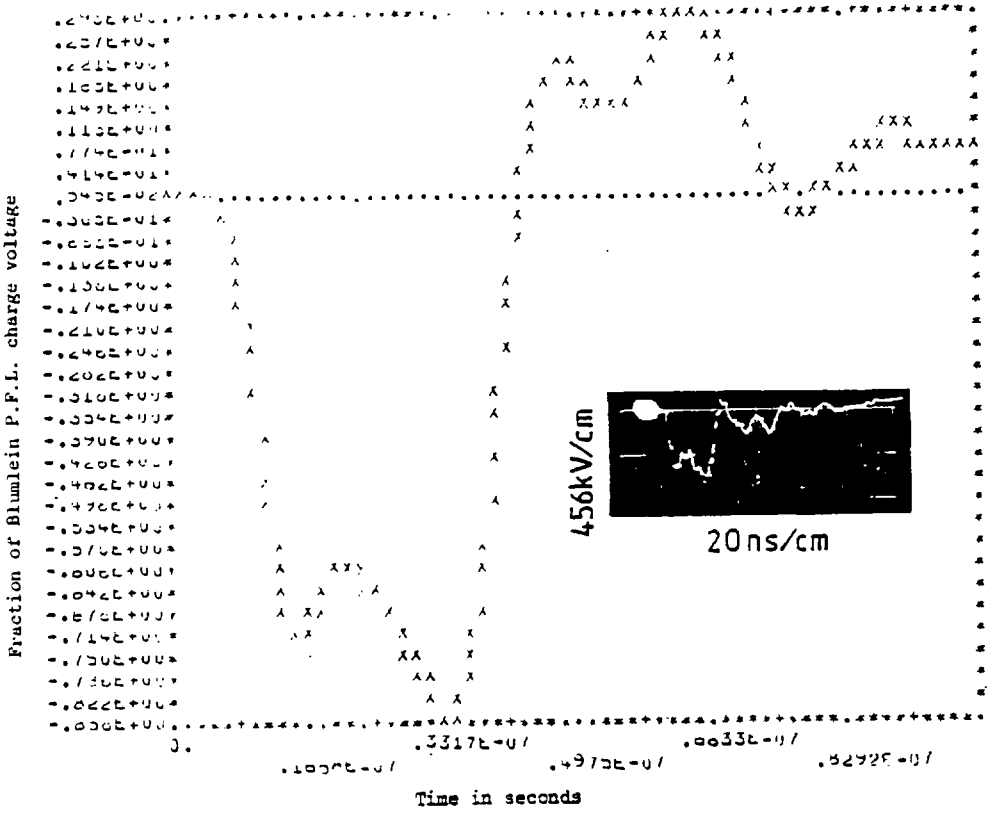


Figure 3: Calculated and observed short pulse voltage profiles from the power supply operating into a 40 Ω e-bear diode

of the electron beam penetrating the walls of the anode tube was found to be uniform to within ±20% over the etched portion of the tube.

The Coaxially Pumped VUV Rare Gas Laser Head

An 8 mm diameter anode tube is used in this head and the blade to anode tube separation was optimised experimentally to a distance of 8 mm. At this separation the maximum diode current was measured to be 12 kA and the total electron beam energy dissipated during the pulse was 110 J.

As the rare gas VUV excimer lasers are very sensitive to impurities, the laser cavity and gas handling components are made of stainless steel, and provision for gas distillation is necessary in the associated gas handling system. The laser reflectors are mounted within two end cavities and consist of a plane >97% reflectivity multilayer dielectric mirror and a barium fluoride etalon. The reflectors are mounted on kinematic mounts adjustable from outside the cavities.

The head has been used to pump the Xenon (Xe_2^*) laser (λ = 172 nm untuned). Maximum laser output is obtained at a Xenon pressure of 11 Bar and laser pulse energies in excess of 30 mJ have been measured in pulses of 10 ns duration (FWHM), with a spectral width of 2.5 nm. The beam divergence is 10 mrad (full angle) at half maximum intensity. Tuning of the xenon laser (over the range 171 - 175 nm) can be achieved by introducing a rotatable quartz prism into the laser cavity. It is anticipated that similar output characteristics should be obtained for a Kr_2^* laser (λ = 146 nm) operated in the head, and the system should also be capable of pumping the Ar_2^* laser (λ = 126 nm).

The Coaxially Pumped Rare Gas Laser Head

The anode tube diameter in this head is 25 mm and optimum performance was achieved with a cathode to anode tube separation of 18 mm. This corresponds to a measured diode impedance of 30 Ω and an estimated 134 J of electron beam energy is dissipated at the anode. The pumped volume is 100 cm^3.

All metal components of the laser cavity and gas handling system are made of stainless steel for ease of passivation and resistance to corrosion. An externally mounted, plane, multilayer dielectric mirror (reflectivity >97%) acts as the back reflector and one of the quartz windows sealing the cavity serves as output coupler.

The excimer lasers XeCl* (λ = 308 nm) and KrF* (λ = 249 nm) have been operated in this head. Laser pulses of ~ 400 mJ energy with 12 ns (FWHM) duration were measured for the KrF* laser (peak power = 33 MW) using a gas mixture of neon, argon, krypton and fluorine (1000: 150:30:1) at a total pressure of 8 Bar. For the XeCl* laser, 300 mJ laser pulses were measured with a duration of 11 ns (FWHM), (peak power = 27 MW) using a gas mix of neon, argon, xenon, and hydrogen chloride (780:190: 26:1) at a total pressure of 7.5 Bar.

The Electron Beam Sustained Discharge Head

In order to achieve long laser pulse operation from the rare-gas halide lasers, an electron beam sustained discharge head has been developed for use with the pulsed power supply operating in the long pulse mode. A 36 cm long transverse edge/plane electron beam diode (~60 Ω impedance) produces a 36x2cm^2 cross-section electron beam. The electron beam is capacitively focussed[6] by means of two electrostatic focussing electrodes which are mounted on to the cathode using glass rod insulators. Although the beam can be tightly focussed to the exact width of the window in the anode plate, in practice the diode, after only a few shots, becomes unstable and vacuum breakdown occurs between the focussing electrodes and the anode. For this reason the beam is focussed to a width of 4 cms at the anode and >24Acm^{-2} of electron beam current density is reliably transmitted into the laser medium through a 75 μm thick P.T.F.E. coated Kapton main foil supported on a "Hibachi" grill structure. A thin (12.5 μm) aluminium foil is used as a prefoil to stop the low energy electrons produced by the tail of the voltage pulse from the power supply.

The electrons pass into the laser cavity through a stainless steel mesh which acts as cathode in the discharge circuit. The discharge in the gas runs between the mesh and a flat anode which lies 3 cm away from the mesh.

The laser/discharge cavity is constructed of P.T.F.E. and stainless steel with 25 mm diameter quartz windows mounted at either end. The optical extraction volume is 127 cm^3 and the pumped volume is 209 cm^3.

Energy for the discharge is supplied by C_4 (see figure 4) which is either a single capacitor or two

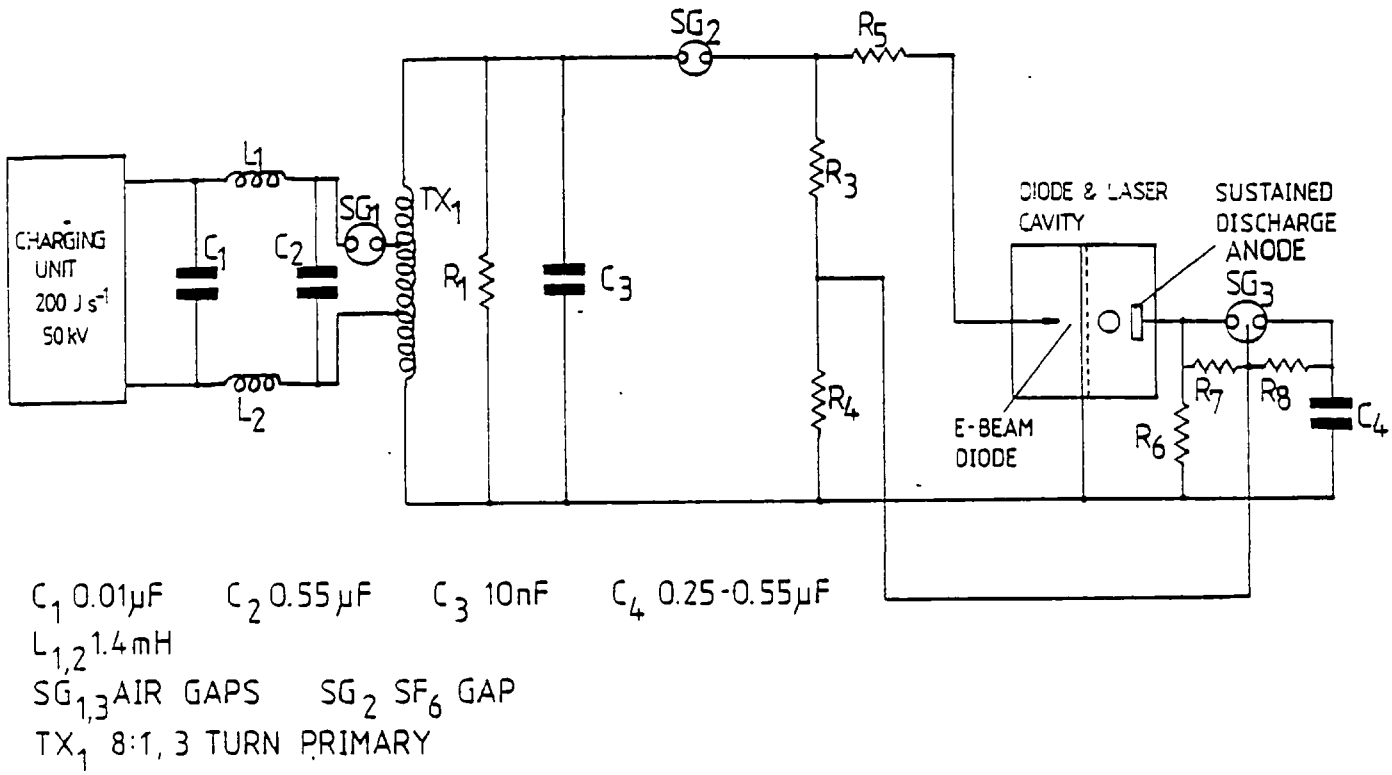


Figure 4: Circuit diagram of the system operating in the long pulse mode

capacitors arranged in the form of a simple Chebyshev type filter [7], used to minimise the inductance of the discharge storage element. The inductance of the discharge circuit must be kept as low as possible so that the amount of energy which can be dissipated in the low impedance (~0.2Ω) ionised laser medium is maximised. A dry air pressurised rail gap is used to switch the energy from C_4 into the gas on receipt of a trigger pulse derived directly from the power supply. This ensures synchronism between the start of the electron beam and the start of the electrical discharge. Three feeds are used to connect the rail gap to the discharge anode to minimise circuit inductance.

The head has been successfully used to pump the XeCl* excimer laser. Laser pulses of up to 800 mJ energy have been produced with a duration of 280 ns (FWHM), using a gas mixture of neon, xenon, and hydrogen chloride (750:25:1) at a total pressure of 5 Bar. The beam diameter is 25 mm.

Acknowledgements

The authors would like to thank H.G. Herbert and J.C. Martin of the Pulsed Power Group at A.W.R.E., Aldermaston for their help in the early stages of the design of the short pulse version of the pulsed power supply. Financial support from the National Research and Development Corporation, the Science Research Council, and Hartley Measurement Limited is also gratefully acknowledged.

References

1. Rohwein G.J. and Buttram M.T., "Preliminary Design of a 100 Hz, 350 kV Short Pulse Generator", Sandia Laboratories, Albuquerque, 1976.

2. Martin J.C. and Smith I.D. "Improvements in or relating to high voltage pulse generating transformers", Pat. No. 1,114,713, May 1968.

3. ECAP is described in the IBM manual "1620 Electronic Circuit Analysis Program (ECAP) Program No. 1620-EE-02X; Manual No. GH20-0170-2".

4. Oomen G.L. and Witteman W.J., "A coaxial e-beam excitation system for high power excimer lasers", Opt. Commun., Vol. 32, (1980), p. 461.

5. Bradley D.J., Hull D.R., Hutchinson M.H.R., and McGeoch M.W., "Megawatt VUV xenon laser employing coaxial electron-beam excitation", Opt. Commun., Vol. 11, (1974), p. 335.

6. Loda G.K. and Meskan D.A. "Repetitively pulsed electron beam generator", Proc. Intern. Top. Con. Electron Beam Res. & Tech., Albuquerque, Vol. II, (1975), p. 252.

7. Cohn D.B. and Lacina W.B. "High power short wavelength laser development", Northrop Corp. Tech. Rep. No. NRTC-77-43R, (1977), p. 40.

"A HIGH POWER-DENSITY ELECTRON-BEAM SUSTAINED LASER"

M. Casey, P.W. Smith and M.H.R. Hutchinson

Optics Section, The Blackett Laboratory,
Imperial College, London SW7 2BZ

Abstract

A high optical power-density excimer laser pumped by an electron-beam sustained discharge has been developed. The electron-beam generator comprised a 200 kV pulse transformer-driven power supply and an electrostatically focussed electron-beam diode. The careful design and optimisation of this generator has allowed very reliable, reproducible operation of the complete laser system with a high enhancement ratio of 4.8. An average output power-density of 0.63 MW cm^{-2} in a 250 ns (FWHM) pulse has been obtained from an e-beam sustained discharge XeCl* laser with an extraction efficiency of 1.5%.

1. Introduction

Electron-beam sustained discharge pumping provides a method for the generation of UV laser pulses of a high intensity and a relatively long duration. Since such pulses are desirable for many applications, a rare gas halide laser system relying on this method of pumping has been developed. It is compact and reliable.

The electron-beam generator comprises a 200 kV pulse transformer-driven power supply and an electrostatically focussed electron-beam diode. Optimisation of the overall system, when used to pump the XeCl* excimer laser, has resulted in an output power density comparable to the highest so far observed from an electron-beam sustained discharge system [1]. The laser output pulse has a reproducibility of better than 5% and the periodic servicing requirements of the system are minimal.

2. The Pulsed Power Supply

An electrical circuit diagram of the complete system is shown in figure 1. Pulsed high voltage generation was achieved by the use of a pulse transformer TX_1. The pulse transformer was a copper foil wound auto- transformer, insulated with polyester film (0.25 mm thick), and vacuum impregnated with transformer oil. The copper foil windings were tapered to grade the electrical field within the transformer, and the three primary turns were situated in the centre of the windings. The transformer had a turns ratio of 8:1 and was energised by discharging C_2 (0.55 μF) into the primary windings via a spark gap SG_1, pressurised with dry air. The gap was a low

inductance rail gap which could be triggered by the application of a high voltage pulse to a third blade electrode situated between the two rail electrodes. The trigger blade was placed two-thirds of the way between the two rail electrodes being closer to the transformer (output) side. A resistive divider across the gap ensured that under pre-fire conditions the trigger electrode was held at a potential which maintained the uniform field conditions within the gap. A negative fast-rising pulse of up to 100 kV amplitude was used to trigger the gap. Since the primary turns of the transformer were located in the centre of the windings, the potential of the primary rose to approximately one half of the output voltage of the transformer. For this reason, C_2 was charged via a D.C. filter network L_1, L_2, C_1, which allowed the primary turns to float when the spark gap SG_1 was fired. It was charged from a 200 Js^{-1} unit to up to 50 kV.

The transformer and associated components can be represented by the equivalent circuit shown in figure 2 and its performance can be calculated using the relationship:

$$\frac{v(t)}{V_{C_2(0)}} = \frac{1}{L_s C_s} \cdot \frac{1}{(\omega_1^2 - \omega_2^2)} \left[\cos(\omega_1 t)\exp(-\alpha t) - \cos(\omega_2 t)\exp(-\beta t)\right] \qquad (1)$$

where v(t) is the voltage on C_3 as a function of time, $V_{C_2(0)}$ is the initial voltage on C_2,

$$\omega_1 = \sqrt{\frac{C_2 + C_s}{L_p C_2 C_s} - \alpha^2} \quad , \quad \omega_2 = \sqrt{\frac{1}{L_p (C_2 + C_s)} - \beta^2}$$

$$\alpha = \frac{R_s}{2 L_s} \quad , \quad \beta = \frac{1}{2 R_L C_s}$$

C_2 is the primary capacitance, L_s is the total series inductance, R_s is the series resistance and L_p is the primary inductance. C_s is the total reflected secondary capacitance and R_L the reflected load resistance. n is the transformer turns ratio.

SG_2, which was a simple two electrode self-breaking spark gap pressurized with SF_6, was set to break down at the first peak of the output of the transformer. This peak was reached in a time t_r which is given approximately by

$$t_r = \pi \sqrt{\frac{L_s C_2 C_s}{C_2 + C_s}} \qquad (2)$$

neglecting damping, and the peak voltage reached V_p is given by[2]

$$G = \frac{V_p}{V_{C_2(0)}} = n\left[\frac{\exp(-\alpha t) + \exp(-\beta t)}{R_C + R_L + 1}\right] \qquad (3)$$

where $R_C = \frac{C_s}{C_2}$, and $R_L = \frac{L_s}{L_p}$.

The gain of the transformer under load was checked by observing and calculating the output voltage of the transformer when the power supply was loaded with a 60 Ω copper sulphate resistor. When C_2 was charged to 46 kV, V_p was measured to be 223 kV, i.e. the observed gain was 4.84. The calculated gain was 4.7, and the time to the first peak was measured and calculated to be 570 ns. The output waveform which was observed when the transformer was allowed to ring into the unswitched capacitor C_3 is shown in figure 3 together with the waveform which was calculated using equation (1).

Under normal operation, the output of the transformer was

switched, via SG_2 and a 2Ω copper sulphate resistor, on to the cathode of a transverse electron-beam diode. The copper sulphate resistor prevented excessive current being drawn from C_3 in the event of an electrical breakdown within the diode chamber. The resulting pulse applied to the diode rose in 100 ns and was 450 ns (F.W.H.M.) long, for a 40Ω diode impedance.

An oil filled tank (0.66 x 1.22 x 1.48 m^3) housed the complete power supply and a conventional field graded, oil to vacuum, high voltage bushing coupled the output from the power supply to the diode chamber and laser cavity. A field plotting computer programme was used to aid the design of the bushing and, in particular, to ensure that the electric field across the bushing was uniformly graded.

3. The Electron-Beam Diode

The final design of the e-beam diode assembly was chosen after extensive experimentation with a variety of electron-beam cold cathode emitters and focussing techniques. For good beam uniformity and low divergence, it is important in the operation of an e-beam sustained laser, that the e-beam transmitted into the laser gas mix should be as uniform as possible. It was also observed that the output energy of the laser increased monotonically as the electron-beam current transmitted through the narrow (2 x 40 cm^2) e-beam window was increased; for this reason, the e-beam current density was maximised.

The performances of the diode assemblies were measured by

collecting the current received by the e-beam diode anode plate and the current transmitted into the evacuated laser cavity and returning the respective e-beam currents to earth through two low value non-inductive resistors constructed from large numbers of carbon composition resistors. The time varying impedance of the diode was then calculated by dividing the observed voltage profile applied to the cathode by the total collected current profile. Although it is possible to calculate the impedance of an un-shielded space-charge limited transverse e-beam diode, it is extremely difficult to allow for the effects of shielding of the emitting surface by the focussing electrodes in such a calculation. Thus, the diode assembly design was optimised empirically, by varying such parameters as the projection of the blade from the blade holder, the anode to cathode separation, the focussing electrode separation, and the blade recess behind the focussing electrodes.

The most convenient and reliable cathode emitter was found to be a single uncoated stainless steel razor blade. Other emitters which were tested included titanium and tantalum foils, graphite felt and multiple blade arrangements. Focussing was at first attempted using a "race track" type structure which surrounded and was electrically connected to the cathode. However, it was found that the beam could not be focussed tightly enough to achieve good transmission through the e-beam window without vacuum breakdown occuring between the "race track" and the anode plate, despite careful polishing and oiling.

As an alternative, capacitive electrostatic focussing [3]

was used. Two focussing electrodes were mounted above and below (see figure 4) the cathode blade holder on glass rod insulators. When the negative voltage is first applied to this type of diode assembly, the cold cathode emitter behaves as if it is unfocussed and the normal blade emission process is not inhibited due to field reduction by the focussing electrodes. Once the blade has started to emit electrons, the focussing electrodes charge up to the cathode potential. The resultant electrostatic field then inhibits the divergence of the e-beam as it travels towards the anode.

By this means, it was possible to constrict the beam height at the anode to match the height of the window into the laser cavity. However, it was found in practice that unless the diode assembly was very accurately and uniformly spaced from the anode plate, and the electrodes regularly oiled, there was still a tendency for vacuum breakdown. To prevent this problem, the tightness of the focussing of the e-beam was slightly reduced by decreasing the depth of recess of the blade behind the focussing electrodes. The resulting e-beam was measured to be 4 cm wide at the anode, which should be compared to a width of 7 cm for an unfocussed beam. It was also found that the spacing accuracy between the anode and cathode was less critical and at a blade to anode sparation of 3.8 cm, a tolerance of ±0.5 mm was sufficient to ensure good blade and foil lifetimes.

All measurements of beam size and uniformity were made using the cellophane-dye dosimetry technique [4]. To prevent saturation of the dye, strips of aluminium foil were used to reduce the e-beam dose

received by the cellophane to an acceptable level.

The electron-beam passed into the laser cavity through two foils and a wire mesh. A thin aluminium prefoil was mounted on to the anode plate to stop low energy electrons produced by the tail of the voltage pulse from the power supply. It was found that if a prefoil was not used, the energy due to these low energy electrons was deposited in the main pressure bearing foil leading to its premature failure. The use of a prefoil also meant that the anode plate presented a uniformly flat surface to the cathode, thereby ensuring a more uniform field in the diode by covering the window recess in the anode plate.

The pressure bearing main foil, supported on a conventional "Hibachi" grill structure, consisted of either 75 μm PTFE coated "Kapton" or 30 μm titanium foil. The titanium foil was found to have a higher tensile strength than Kapton, although when it failed the foil collapsed totally and often caused damage to the e-beam diode assembly. Kapton was found to fail gradually by developing small pin holes and also had the advantage that it had a slightly higher e-beam transmission than the titanium foil. Finally, the e-beam passed through a stainless steel mesh of 80% transmission which acted as a cathode for the discharge in the laser cavity.

Under the normal operational conditions, the peak voltage which was applied to the cathode was 189 kV and the peak total e-beam current measured by the earth return resistors was 4.1 kA. Thus, at the peak of the power deposition in the e-beam diode, the diode

impedance was 47 ± 5Ω. As a further check on this system, a computer code[5] ECAP (IBM 1965) was used to calculate the performance of the power supply into a fixed load equal to the average diode impedance and good agreement was found between the observed and calculated e-beam cathode current and voltage profiles. Typical profiles are shown in figure 5, together with the synchronised voltage and current profiles associated with the discharge circuit. Diode closure can clearly be seen on the e-beam current profile as a sharp rise in current at the end of the pulse.

The mean current density at the prefoil was calculated to be 26 A cm^{-2} and cellophane-dye dosimetry indicated that at the central portion of the foil the current was approximately 30 A cm^{-2}. The e-beam current density reaching the discharge region was attenuated by the foils and mesh. It was measured using a Faraday cup and found to be 13 A cm^{-2}.

4. The Discharge Circuit

Energy for the electrical discharge was stored in C_4 (0.55 μF) which was charged to a maximum value of 30 kV. A spark gap, SG_3, switched the energy from C_4 into the laser discharge cavity. This spark gap was a low inductance rail gap, pressurized with dry air, which was triggered automatically from a potential divider R_2, R_3 mounted in the pulsed power suply. D.C. biasing of the trigger electrode was set using the resistor network R_5, R_6, and R_7.

The amount of energy discharged into the cavity is strongly dependent on the overall inductance of the discharge circuit. We have observed, and it has been reported [6], that the discharge impedance in an e-beam sustained excimer laser system falls rapidly to a low but fairly constant value, which is mainly dependant on such factors as the concentration of halogen bearing molecules, gas pressure, e-beam density and discharge dimensions. If the time varying discharge impedance is denoted by $Z_d(t)$, transient circuit analysis of the discharge circuit as shown in figure 1 leads to an expression for the voltage across the discharge as a function of time shown below. (A typical value for Z_d after the initial impedance drop in our system when pumping the excimer XeCl* was 0.3Ω).

$$v_d(t) = V_{C_4(0)} \frac{Z_d(t)}{\omega L} \exp(-\alpha' t)\sin(\omega t) \qquad (4)$$

where $V_{C_4(0)}$ is the initial voltage on C_4,

$$\omega = \sqrt{\frac{1}{LC_4} - \alpha'^2} \quad , \quad \alpha' = \frac{Z_d(t)}{2L}$$

The inductance of the discharge circuit was kept as low as possible to maximise the total discharge energy deposited in the gas and minimise the discharge voltage risetime. Low inductance parallel plate feeds connected C_4 to SG_3 and three feeds were used to connect SG_3 to the cathode in the discharge cavity. The discharge current was monitored by a Nichrome foil resistor which was placed in series with the earth return conductor of the discharge circuit. Typical waveforms for the discharge circuit are shown in figure 5.

5. Laser Operation and Performance

All metallic components of the laser cavity were stainless steel. The discharge anode was mounted via three spacers on to a thick sheet of PTFE backed by perspex (figure 4). The interelectrode spacing could be varied by adjusting the thickness of the spacers and the highest laser output energies were obtained at a spacing of 3 cm. Spectrosil 'A' quartz windows of 2.5 cm diameter were mounted at either end of the discharge cavity and the laser resonator was formed by mounting multilayer dielectric mirrors of 97% and 60-70% reflectivities outside the cavity.

With e-beam pumping alone, a maximum output of 70 mJ in a 140 ns (FWHM) pulse was measured using argon as the major diluent. The gas mix was HCl: Xe: Ar in the ratio 1:15:1140 at a total pressure of 3 Bar. In the sustained mode, the highest laser output energies were obtained with Neon as buffer gas. With C_4 charged to an optimum value of 24 kV, an output energy of 800 mJ was measured in a pulse of 250 ns (FWHM) duration, corresponding to a specific energy of 4 J/l and an average power of 3.2 MW. The optimised gas mix was HCl:Xe:Ne in the ratio 1:17:1260 at a total pressure of 5 Bar. A 5% cm^{-1} laser gain was derived from measurements of operation under these conditions.

In order to measure accurately the volume of the gas which was pumped by the e-beam and discharge, thin strips of blue cellophane were placed within the discharge cavity at the cathode mesh, the anode

and at a position mid-way between the two electrodes. By firing the system with the cellophane in position, the width of the pumped volume could be measured as the distance from the mesh was increased. As expected, the width increased with distance from the mesh and the pumped volume was calculated to be 430 cm^3. The optical extraction volume as defined by the two windows was 196 cm^3.

Since the energy with which the electrons entered the gas after transmission through the foils and mesh could not be calculated accurately, blue cellophane dosimetry was used to estimate the e-beam energy deposited in the gas. It was found to be 20 J. The time varying voltage and current traces of the discharge gave a value for the discharge energy deposited of 96 J.

From these measurements the extraction efficiency was calculated to be 1.5%, while the mean power efficiency once laser action had begun was 3.2%.

6. Conclusions

The enhancement ratio for this system, of the power deposited in the gas from the discharge to that for the electron beam, was 4.8. This is a high value compared to other e-beam sustained $XeCl^*$ lasers[1,7] and reflects the care taken in the design and optimisation of the pulsed power supply and electron-beam diode. Consequently, relatively high laser output power densities were achieved using a modest electron-beam generator which was compact and extremely reliable.

The authors would like to acknowledge financial support from the National Research and Development Corporation and the Science and Engineering Research Council.

7. References

1. D.E. Rothe, J.B. West, M.L. Bhaumik, IEEE J. Quant. Electron., QE-15, 314 (1979).

2. J.C. Martin, private communication.

3. G.K. Loda, D.A. Meskan, Proc. Int. Top. Conf. on Electron Beam Res. and Tech. (Albuquerque,), 252 (1975).

4. E.J. Henley, Nucleonics, 12, 62 (1954).

5. I.B.M., 1620 Electronic Circuit Analysis Program (ECAP), Manual No. H20-0170-0 (1965).

6. W.H. Long, R.S. Braford, IEEE J. Quant. Electron., QE-15, 327 (1979).

7. J.I. Levatter, J.H. Morris, S. Lin, Appl. Phys. Lett., 32, 630, (1978).

8. Figure Captions

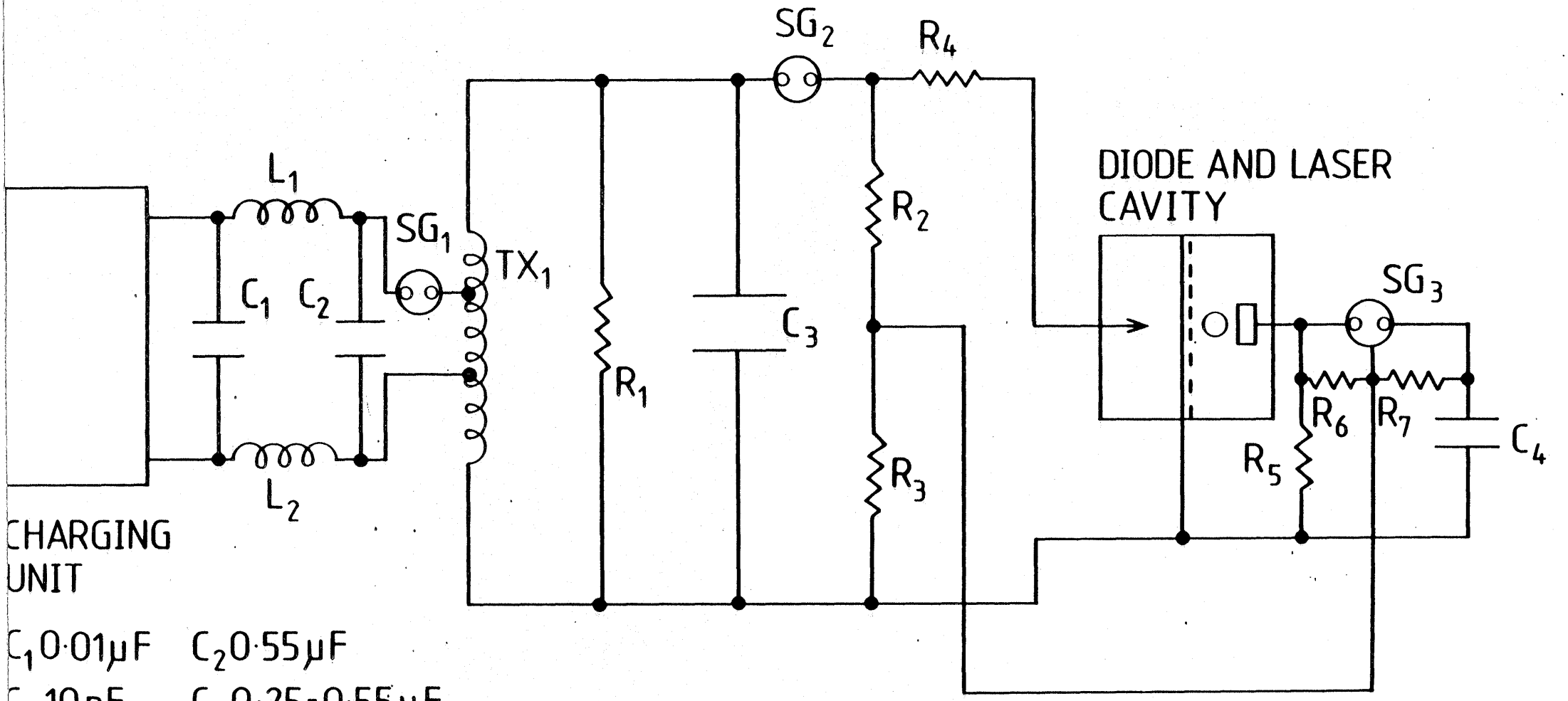
Figure 1: Circuit diagram of the complete system.

Figure 2: Equivalent circuit of the pulsed power supply.

Figure 3: Calculated and observed transformer performance.

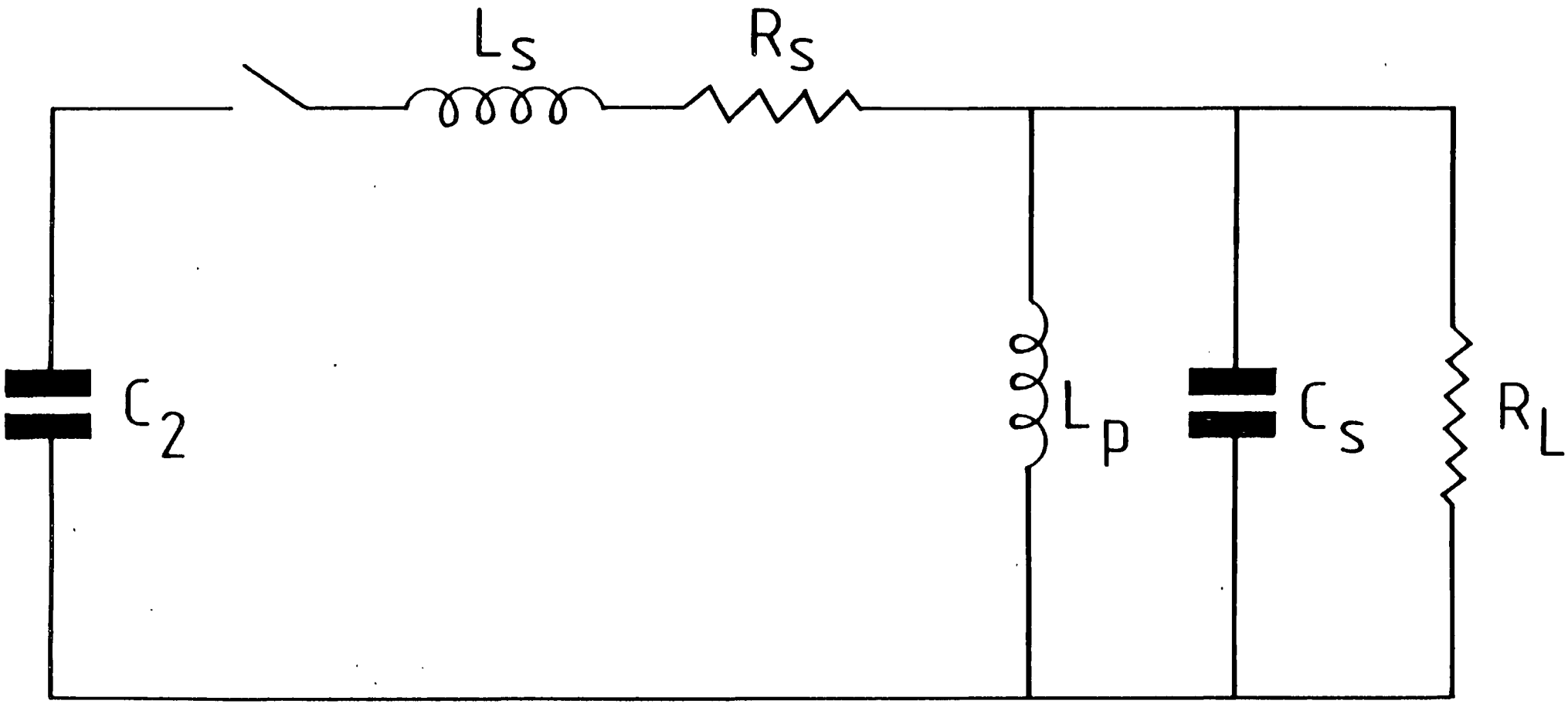
Figure 4: E-beam sustained discharge head.

Figure 5: Synchronised electrical characteristics of the electron-beam and the discharge.



C_1 0·01μF C_2 0·55μF
C_3 10nF C_4 0·25-0·55μF
$L_{1,2}$ 1·4mH

CIRCUIT DIAGRAM OF THE COMPLETE SYSTEM FIG 1



EQUIVALENT CIRCUIT OF THE PULSED POWER SUPPLY

FIG 2

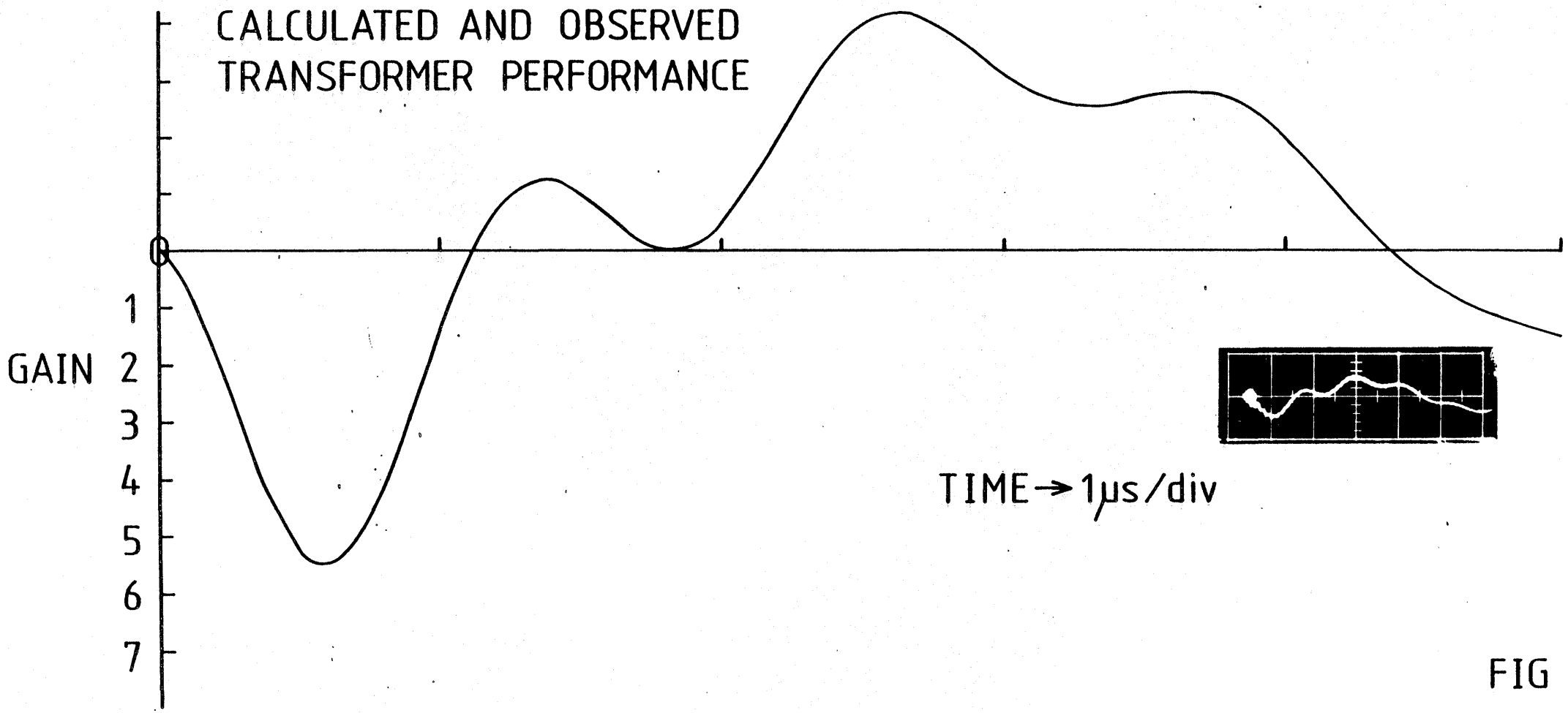
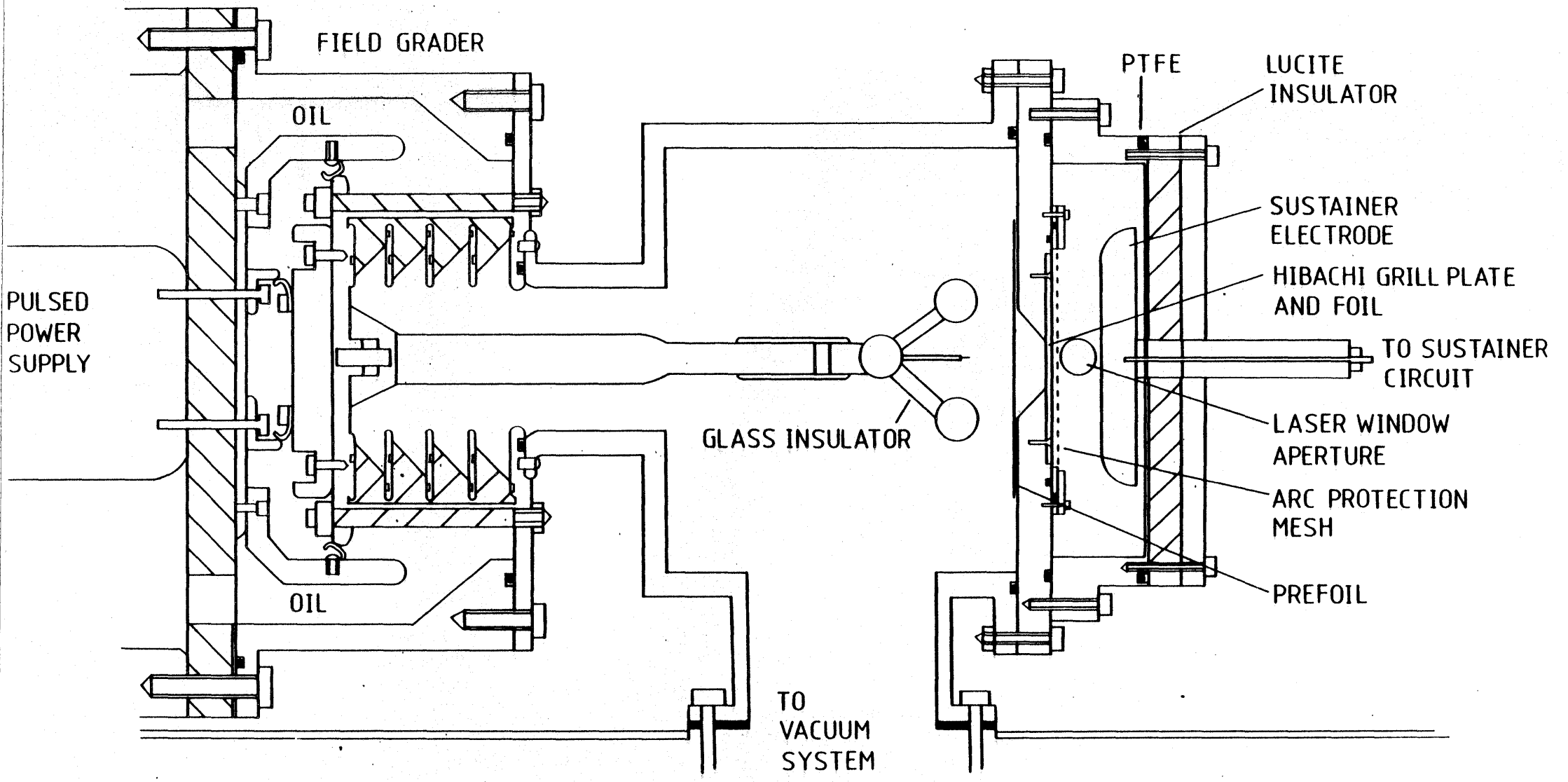

CALCULATED AND OBSERVED
TRANSFORMER PERFORMANCE
0
1
2
3
4
5
6
7
GAIN
TIME→1μs/div

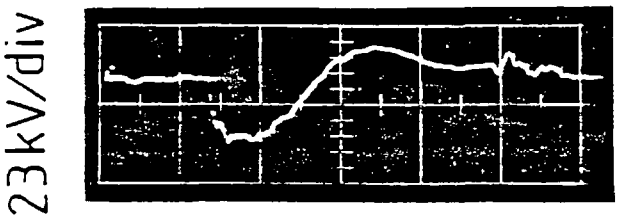
FIG 3



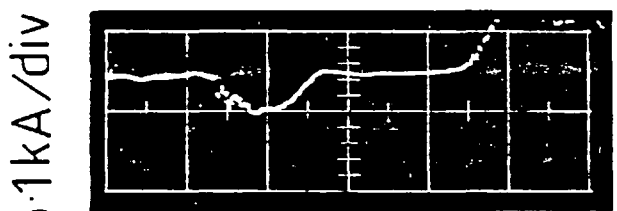
E-BEAM SUSTAINED DISCHARGE HEAD

FIG 4

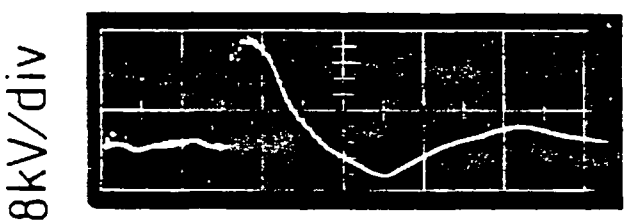
E-BEAM VOLTAGE



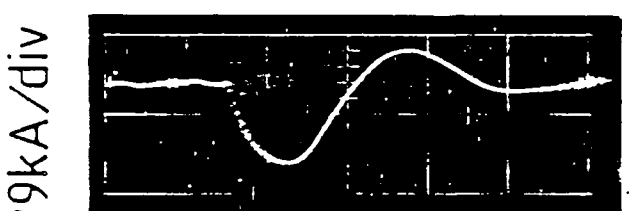
E-BEAM CURRENT



DISCHARGE VOLTAGE



DISCHARGE CURRENT



SYNCHRONISED ELECTRICAL CHARACTERISTICS OF THE ELECTRON BEAM AND THE DISCHARGE

FIG 5